

Triggering Mechanisms and Rainfall Thresholds
of Shallow Landslides on Soil-mantled Hillslopes
with Permeable and Impermeable Bedrocks

January 2006

Yuki MATSUSHI

Triggering Mechanisms and Rainfall Thresholds of Shallow Landslides on
Soil-mantled Hillslopes with Permeable and Impermeable Bedrocks

A Dissertation Submitted to
the Graduate School of Life and Environmental Sciences,
the University of Tsukuba
in Partial Fulfillment of the Requirements
for the Degree of Doctor of Philosophy in Science
(Doctoral Program in Geoenvironmental Sciences)

Yuki MATSUSHI

Abstract

Rainfall-induced shallow landslides occur in most soil-mantled steep hillslopes as a dominant denudation process in humid temperate regions. This study revealed the hydrological-triggering mechanisms and rainfall thresholds of landslides in adjoining hills with permeable sandstone and impermeable mudstone bedrocks in the Boso Peninsula, Japan. Detailed field and laboratory investigations were conducted to inspect the subsurface structures and to obtain geotechnical properties of slope materials. The characteristics of slope hydrology were inferred from pressure-head monitoring and rainfall–runoff observations. An analysis of slope stability identified critical conditions for the several past landslides.

Hydrological triggering of landslides differs with hillslope lithology. Rainwater percolates through the permeable sandstone slope as an unsaturated gravitational flow. The wetting front migration results in a decrease in soil cohesion and causes landsliding at the steep lower part of the hillslopes. In the hillslope with the impermeable mudstone, the hydraulic discontinuity beneath a thin soil layer causes a transient positive pressure head that generates a saturated subsurface storm flow. The reduction in effective normal stress triggers a shallow soil slip at the uppermost part of hollows.

An analysis of the relationship between the magnitude of rainfall and hillslope instability provides a rainfall threshold for landsliding. The rainfall threshold can be expressed by a power-law function that combines rainfall intensity and duration. The site-specific combination of rainfall intensity and duration incorporates geotechnical properties of hillslope materials and slope hydrological processes. The hillslope with

permeable sandstone has greater critical rainfall and hence a longer recurrence interval than the impermeable mudstone hillslope. This implies the lower potential for landsliding in the sandstone hillslopes, corresponding to the lower landslide activity.

Keywords: shallow landslides, hillslope hydrology, slope stability, critical rainfall, permeability, pressure head, soil-water characteristic curve, shear strength

Contents

	Page
Abstract	i
Contents	iii
List of Tables	vi
List of Figures	vii
Chapter I Introduction	1
I-1 Importance of rainfall-induced shallow landslides	1
I-2 Previous studies and their problems	3
I-3 Purpose and approach of this study	6
Chapter II Study area	8
II-1 General settings	8
II-2 Topography of the hills	9
II-3 Spatial and temporal distribution of shallow landslides	10
Chapter III Slope morphology and subsurface structure	13
III-1 Slopes	13
III-2 Soil sounding and geophysical surveys	13
III-3 Soil thickness	15
III-4 Geophysical structures	15
III-5 Sallow soil profiles	16
Chapter IV Geotechnical soil properties	18
IV-1 Soil sampling and geotechnical tests	18
IV-2 Basal soil properties	19

IV-3	Permeability	19
IV-4	Soil-water retention characteristic	20
IV-5	Shear strength	22
Chapter V	Slope hydrology	26
V-1	Methods of hydrological observations	26
V-2	Long-term fluctuations of pressure head and rainfall–runoff characteristics	28
V-3	Short-term response of pressure head to rain infiltration and subsurface water behavior	29
V-4	In situ soil-water retention characteristics	30
Chapter VI	Discussion	32
VI-1	Landslide mechanisms	32
VI-1-1	Slope stability analysis	32
VI-1-2	Critical conditions for landsliding	34
VI-1-3	Hydrological triggering of the landslides	35
VI-1-4	Implication of the landslide-triggering mechanisms to landslide locations and hill morphologies	39
VI-2	Rainfall thresholds for landsliding	40
VI-2-1	Changes in factor of safety during rain storms	40
VI-2-2	Analysis of the relationship between the magnitudes of rainfall and slope instability	42
VI-2-3	Critical combinations of rainfall intensity and duration	45
VI-2-4	Recurrence intervals of the critical rainfall	47
VI-3	Summary of discussion, advantages and future prospects	48

Chapter VII	Conclusions	50
	Acknowledgements	52
	References	53
	Tables	64
	Figures	73

List of Tables

	Page
Table 1 Sequence of landslide occurrence from aerial photographs	64
Table 2 Dimensions of the landslides	65
Table 3 Physical properties of the soils	66
Table 4 Optimum parameter values for the model fitted to soil-water retention characteristics	67
Table 5 Moisture contents and shear test results for each specimen group	68
Table 6 Shear strength parameters obtained by a simple linear-regression for the dataset of each specimen group	70
Table 7 Optimum parameter values for the regressions for reduction in soil shear strength	71
Table 8 Parameter values for envelopes of in situ the soil-water retention plots	72

List of Figures

		Page
Figure 1	Location and shaded relief map of the study area	73
Figure 2	Climatic conditions of the study area	74
Figure 3	Geologic map and topographic cross-sections of the study area	75
Figure 4	Records of annual maximum daily rainfall in the study area	76
Figure 5	Rainfall records of the 1989 storm	77
Figure 6	Aerial photographs taken in 1990	78
Figure 7	Landslide densities for the past two decades	79
Figure 8	Locations of the selected slopes and topographic maps of the observed watersheds	80
Figure 9	Profiles of the selected slopes, and plan views and cross sections of slip scars	81
Figure 10	Subsurface structures of the hillslopes inferred from soil soundings and geophysical surveys	82
Figure 11	Shallow soil profiles at the soil pits with depth variations of the cone penetration resistance	84
Figure 12	Grain-size distributions of the soils	85
Figure 13	Vertical profiles of hydraulic conductivity	86
Figure 14	Soil-water characteristic curves of the soils	87
Figure 15	Results of shear tests for the soil specimens with varied moisture contents	88

Figure 16	Relations between the volumetric water content and shear strength parameters	89
Figure 17	Results of multiple linear-regression analyses for the formulation of shear strength reduction	90
Figure 18	Reduction in shear strength with respect to increasing soil volumetric water content	91
Figure 19	Comparison of measured and calculated shear strength	92
Figure 20	Pressure head fluctuations in slopes and hydrographs in watersheds for the entire observation period	93
Figure 21	Short-term pressure head responses and equipotential lines of hydraulic head during May 19 to 21, 2004	97
Figure 22	Changes in volumetric water content in slopes with fluctuations of pressure head at corresponding depths	98
Figure 23	Soil-water retention plots from in situ monitoring	99
Figure 24	Schematic illustration of the infinite-slope model for the limit equilibrium stability analysis	100
Figure 25	Simulation of the reduction in factor of safety with increasing pressure head	101
Figure 26	Schematic illustrations showing hydrological landslide-triggering mechanisms	102
Figure 27	Slope stability fluctuations calculated from observed pressure heads	103
Figure 28	Analytical procedures for determining critical rainfall	105

Figure 29	Inverse correlations between the minimum factors of safety and mean rainfall intensities at the most effective rainfall duration	106
Figure 30	Rainfall thresholds for landsliding and temporal changes in mean rainfall intensity of the torrential rainfall on August 1, 1989	107
Figure 31	Recurrence intervals of the critical rainfall	108
Figure 32	Hydrological landslide-triggering cycles in hillslopes with permeable and impermeable bedrocks	109

Chapter I Introduction

I-1 Importance of rainfall-induced shallow landslides

Shallow landslides in response to heavy rainstorms occur in soil-mantled steep hillslopes as a dominant erosional process in humid temperate regions. Landslides remove materials from hillslopes and scour low-order channels, supplying a large quantity of sediment to high-order fluvial systems (Dietrich and Dunne, 1978). Denudation by landsliding occupies the majority of total sediment yield from drainage basins (Aniya, 1985).

Most shallow landslides are located on unchanneled hollows as evidence of ongoing upslope development of valley heads (Tsukamoto, 1973; Tsukamoto et al., 1982; Reneau and Dietrich, 1987). Repetition of landslides promotes sustaining growth of hillslope depression, determining persistent spacing of hollows and noses in drainage basins (Iida and Okunishi, 1979, 1983). Therefore, location of landslides controls expansion of channel networks (Montgomery and Dietrich, 1988, 1992). Frequent landsliding enhances highly bifurcating drainage structure, by increasing density of shallow drainage depressions in upper hillslopes (Inoue and Oguchi, 1995).

Drainage density correlates negatively with relative relief of basins or slopes in a steep terrain subject to frequent landsliding (Oguchi, 1997; Tucker and Bras, 1998; Talling and Sowter, 1999). This indicates that landslides play a vital role in forming *low-relief and finely-dissected landscapes* (Mino, 1942, pp. 362–370; Yatsu, 1950), since they actively reduce ridges and develop small headwaters. Consequently, spatial and temporal distributions of shallow landslides are important controls on long-term change of the hilly landscapes.

Hill morphology depends clearly on geology, reflecting the long-term results of cumulative denudation of hillslopes. Suzuki et al. (1985) pointed out that permeability and strength of bedrocks behave as crucial agents for landscape change, controlling the basin relief and drainage density. Precipitation extremes are responsible for a catastrophic denudational event that deforms the basins. However, actual hydro-geomorphological processes in hillslopes during intense rainstorms remain controversial.

Subsurface water behavior in hillslopes as well as the critical condition leading to landslides thus has to be studied in detail in relation to physical and mechanical properties of hillslope materials. Linkage between slope hydrology and slope instability provides a clue to addressing the actuality of landscape change. Studies on contemporary denudation by shallow landslides will exert a persuasion on explaining evolution of the different hilly landscapes.

Rainfall-induced shallow landslides pose a grave threat to lives and property in another standpoint, since they occur suddenly and often travel a long distance as a high-speed debris flow. A shallow landslide and subsequent debris flow cause thousands of deaths and serious economic damage worldwide, especially in mountainous regions subjected to heavy rainfall. Although human activities such as deforestation of hillslopes or cutting of the slope toe for construction purposes conduce to landsliding, the majority of landslides occur simply as a result of intensive rainwater infiltration to an otherwise stable natural hillslope. Prediction of landsliding of a natural hillslope thus meets a societal demand on the hazard assessments.

Identifying a rainfall threshold for landslide initiation becomes a fundamental task to predict and prevent the hazards. The rainfall threshold provides requisite information

to make a decision on issuing landslide warnings for a resident evacuation or road closures. The threshold for landslide initiation is unlikely to be uniform in a regional scale, but changes with geological settings. Hence, a quantitative evaluation of the relativity of the site-specific thresholds to the nature of hillslope materials arises as an important issue in the disaster mitigation practice.

I-2 Previous studies and their problems

Stability of natural slopes was analyzed as a one of longstanding geotechnical problems (e.g. Skempton and Delory, 1957; Terzaghi, 1962). Carson and Petley (1970) brought the geotechnical strategies into geomorphology for discussing denudation processes operating on hillslopes. After the pioneering studies, geomorphologists began to employ the mechanical slope stability analysis to evaluate denudation and development of hillslopes (Carson, 1971; Prior and Graham, 1974; Rogers and Selby, 1980; Matsukura and Tanaka, 1983; Matsukura, 1984). Since shallow landslides in humid tropical environments result mostly from heavy rains, identification of rainfall threshold for landslide initiation becomes a coincident issue in this discipline.

A primitive concept of a landslide-triggering threshold of rainfall was developed through separating the rainfall events that triggered landslides from non landslide-triggering storms. Several researchers concentrated their efforts on establishing this empirical threshold by identifying critical combinations of rainfall intensity and duration (Caine, 1980; Cannon and Ellen, 1985; Wieczorek, 1987; Terlien, 1998; Jakob and Weatherly, 2003). The empirical threshold can be applied for issuing landslide warnings in combination with real-time monitoring of a network of telemetering rain gauges and regional precipitation forecasts. Implementation of this

warning system achieved an apparent success to predict landslide occurrence at a storm in 1986 in California (Keefe et al., 1987).

A weak point of the empirical approach is to treat the physical processes in hillslopes as a *black box*. The critical relationship between rainfall intensity and duration must be strongly influenced by site-specific conditions, especially in physical and mechanical properties of hillslope materials. The surface material on hillslopes originates basically from decomposition of bedrock. Geological variation in the bedrocks produces the varying physical and mechanical properties of soils. Thus the rainfall threshold depends on geology of the hills. This becomes most obvious at disparity in temporal and spatial landslide frequencies among natural drainage basins with varying geological settings.

Several studies explained the effect of basin geology on landslide activity by whether hillslopes tend to easily or hardly be saturated (Onda, 1992, 1994; Onda et al., 2004). The landslide activity was interpreted by susceptibility of hillslopes to generation of positive pressure heads under a saturated regime, in association with water storage capacity of regolith zone and/or subsurface water flow paths. However, this explanation is insufficient regarding the mechanism and threshold of landslide initiation. Some landslides most probably occur under an unsaturated regime, resulting only from a decrease in cohesive shear strength of the soil (Krahn et al., 1989; Rahardjo et al., 1995; Terlien, 1997). Van Asch et al. (1999) emphasized the importance of a comprehensive understanding of how the hydrological processes affect the destabilization of hillslopes.

The theoretical relation between slope hydrology and landslide initiation was analyzed using physically motivated models in late 1980s and 1990s. The models

developed in coupling a concept of steady-state saturated throughflow above an impermeable bed with an infinite-slope stability analysis (Okimura and Ichikawa, 1985; Montgomery and Dietrich, 1989, 1994; Wu and Sidle, 1995). This *steady-state* type model achieved success in explaining landslide distribution in mountain drainage basins and assessing topographic control on landslide susceptibility of hillslopes (Iida, 1999; Borga et al., 2002). However, several issues remain unsolved in the *steady-state* models regarding the supposed hydrological concept.

Results of hydrological observation in a natural hillslope contradicted the steady-state slope hydrology (Yasuhara, 1984; Musiaka et al., 1988; Johnson and Sitar, 1990; Fannin and Jaakkola, 1999; Fannin et al., 2000; Simoni et al., 2004). Direct measurement of subsurface hydrological response during rainstorms revealed that the soils on hillslopes respond quickly and transiently to rainfall, and non-steady moisture redistribution follows the intense rainwater infiltration. Iverson (2000) pointed out the timescale discrepancy between the conceptual and real slope hydrology in a landslide source area. The concept of steady-state groundwater flow can predict only the long-term distribution of pressure head, which should be identified as a predisposition to landsliding.

The aforementioned shortcomings prevent the *steady-state* models from providing a rationale for simultaneous landslide occurrence at a rainfall peak associated with intense rainwater infiltration (Iverson, 2000; D'Odorico et al., 2005). In addition, the concept of steady-state subsurface flow parallel to the slope cannot apply to hillslopes underlain by highly permeable bedrocks. Lack of hydraulic discontinuity at the bottom of a soil column allows vertical percolation of rainwater, and hence the near-surface lateral water movement becomes an unfeasible proposition.

Recently, numerical simulations of rainwater infiltration greatly improved our understanding of hydrological conditions for landslide initiation. A one- or two-dimensional finite element method was typically used in combination with a slope stability analysis. The finite element analysis proved that the vertical rainwater infiltration and subsequent non-steady redistribution of pressure head are sufficiently competent to trigger landslides (Gasmo et al., 2000; Cho and Lee, 2001; Collins and Znidarcic, 2004; Kim et al., 2004).

However, there are still few quantitative studies of hillslope hydrological processes connecting to landslide mechanisms based on field observations. We cannot expect more pertinent discussion about the geologically controlled landslide mechanisms or rainfall thresholds unless the actual slope hydrology is linked with the critical condition for landsliding. Certain field evidence is needed to understand how subsurface-water dynamics influence landslide initiation, denudation of hillslopes, and landscape evolution.

I-3 Purpose and approach of this study

The present study aims to reveal slope hydrological processes and landslide-triggering mechanisms in two hilly locations with contrasting morphology and bedrock. Discussion in this study focuses on clearing the *black box*, by making a quantitative association between stability limit of hillslopes, subsurface water behavior, and critical rainfall for landsliding. The connection of properties of slope materials, slope hydrology, and rainfall thresholds is an unprecedented attempt in the previous studies, so that assures the novelty of this work.

Detailed field and laboratory investigations were conducted to accomplish the

objective. Geophysical inspections revealed the subsurface slope structures. Geotechnical testing provided properties of slope materials relevant to slope stability analysis. Hydro-climatic observations elucidated pressure head responses in hillslopes to rainfall as well as rainfall–runoff characteristics in small watersheds.

Chapter II Study area

II-1 General settings

The study area is located in the south-west Boso Peninsula, central Japan (Fig. 1). The peninsula lies on the southernmost margin of the North American plate, bordered on the south by the Philippine Sea plate. Westward subduction of the Pacific plate characterizes the geotectonic segments of this region as a non-volcanic outer arc above the subduction boundary. This geotectonic environment activates the coseismic crustal movement of this area, resulting in rapid uplifting at a rate of > 1 m/kyr throughout the Quaternary (Kaizuka et al., 2000, p. 151).

Bedrock in this area belongs to the middle Pleistocene forearc basin fill, referred to as the Kazusa Group (Ito, 1995, 1998). Submarine fan successions generated by glacioeustasy cycles under the influence of paleo-ocean currents produced repeated sandy and muddy depositional sequences (Ito, 1998; Ito and Horikawa, 2000). The emergence of these submarine deposits in the last 500 ka has led to the development of small hills ranging in elevation of 100–300 m.

The region has a humid temperate climate with average daily temperatures between 5°C and 30°C, and with mean annual rainfall of 1500–2000 mm (Fig. 2). The orographic effect enhances the rainfall at the southern part of the peninsula. Seasonal fronts in early summer and fall as well as occasional typhoons contribute to 40–50% of the total rainfall. The area receives very little snowfall, and the snow coverage rarely remains on the ground for extended periods.

Brown forest soil develops on the hillslopes, except for narrow ridges or steep slip scars with bedrock exposures. A planted forest of cypress (*Chamaecyparis obtusa*) and

cedar (*Cryptomeria japonica*) covers the study area. Hardwood and various understory species also coexist within the conifer stands. The forest age varies from several years to several decades. No large-scale timber harvesting has been conducted in the recent decades.

II-2 Topography of the hills

The study site exhibits distinct topographic characteristics that vary from hills in the northwest to hills in the southeast. The dashed lines in Fig. 1 demarcate this boundary between the varying morphometric characteristics. Hill terrains in the northwestern section exhibit relatively high rounded crests (relative relief of 150–200 m) with low drainage density ($5\text{--}8\text{ km}^{-1}$). The southeastern hills display low rugged ridges (relative relief of 50–100 m) with high drainage density ($15\text{--}22\text{ km}^{-1}$).

The topographic difference corresponds to the geology of the area (Fig. 3). Coarse sandstone and conglomerates (the Nagahama and Ichijuku Formations; ca. 600–700 ka) comprise the northwest high terrain, whereas muddy sandstone and sandy mudstone (the Iwasaka and Awakura Formations; ca. 700–800 ka) make up the southeast lower terrain. Hereafter, we call these two areas the sandstone area and the mudstone area (Figs. 1 and 3).

Overall, the landscape with the two areas comprises cuesta-like landforms with back-slopes facing northwest (Fig. 3). The southwest–northeast rows of the cuesta ridges widely develop in the southern Boso Peninsula, which have been recognized as a structural geomorphology reflecting a variety of bedrocks (Nakagawa, 1960; Suzuki, 1985; Kaizuka et al., 2000, pp. 151–152). Several major rivers on the peninsula (such as the Koito River in Figs. 1 and 3) incise the cuesta rows as an antecedent valley prior

to the development of the geologically-controlled hilly landscapes.

II-3 Spatial and temporal distribution of shallow landslides

The study area has experienced episodic denudational events by shallow landsliding. Heavy rainstorms trigger almost all shallow landslides in the study area, although large earthquakes has also occurred periodically around the Boso Peninsula. Figure 4 shows the records of annual maximum 1-day rainfall and the five largest earthquakes in the study area. The earthquake on December 17, 1987 caused more than 380 cliffs or slopes to fail in the northeastern part of the peninsula (Kamai and Noro, 1988). Intense acceleration by the earthquake triggered not only the toppling or fall type of failures but shallow slides of natural hillslopes (Kamai 1989; Waragai et al., 1993). However, these failures took place within an area of 30–60 km northeast from the area of interest. Hence only the rainfall extremes are responsible for shallow landsliding in the study area at least for the recent decades.

Torrential rainfall on July 1, 1970 and August 1, 1989 caused the two largest landslide events in the recent decades (Furuya and Ohkura, 1992; Numamoto et al., 1999). The present study focuses on the latest one, the 1989 storm, of which the detailed records of rainfall and landslides are available. Figure 5 shows the records of the 1989 storm at four meteorological stations within a 30-km radius from the study area. The storm provided the rainfall of 30–70 mm/h in the maximum 1-h intensity. Cumulative rainfall of 250 mm fell at Yokohama in minimum and 450 mm fell at Sakuma in maximum during approximate a day from the onset of the storm body.

The rainstorms produced many slides along the mudstone slopes, but only a few hillslopes failed in the sandstone area (Fig. 6). Landslides occurred only on steep lower

parts of hillslopes adjacent to major valleys in the sandstone area, while the landslides in the mudstone area took place mainly on uppermost hollows near slope crests (Matsushi and Matsukura, 2004). Although area of the individual landslides could not be measured precisely on the aerial photographs, the approximate size of landslide sources in the sandstone area (width 30 m × length 50 m) tends to be larger than that in the mudstone area (20 m × 40 m).

The number of the landslide scars produced over the past two decades was identified using sequential air photographs taken by Geographical Survey Institute in 1981, 1984, 1990, 1995, and 2000 (Table 1). The photo-reading ambits were confined to six basins of 3rd or 4th stream order in each area. The landslide distribution maps from the two consecutive photos were superimposed to delimit landslides which had occurred during the five periods: before 1981, 1981–84, 1984–90, 1990–95, and 1995–2000 (Fig. 4, Table 1).

Figure 7 shows the changes in landslide density (number of slip scars per unit area) in the five periods during the past two decades. The prominent bars on 1984–1990 resulted undoubtedly from the 1989 storm, since no other significant storms were observed during the period (Fig. 4). The density of landslides by the storm in the mudstone area reaches 71.1 km^{-2} , being about 19 times larger than that in the sandstone area (3.8 km^{-2}). In the 20-year total, landslide density in the mudstone area (127.6 km^{-2}) is about 22 times larger than that in the sandstone area (5.7 km^{-2}).

The adjoining hills have no great variation in climatic conditions, vegetation cover, and tectonic settings. Therefore, the variation in the density and locations of the landslides must reflect slope hydrology and mechanical stability limits for landsliding of the hillslopes in each area. This study evaluates the hillslope hydrological processes,

and physical properties of the hillslope materials to explain the different landslide activities.

Chapter III Slope morphology and subsurface structure

III-1 Slopes

Field and laboratory experiments were designed to understand hillslope hydrological processes and obtain parameter values relevant to slope stability analyses. For these purposes, three slipped slopes with a typical size and geometry were selected in each area (Figs. 8A and 8C). Geotechnical properties of hillslope materials are assumed to be spatially homogeneous within the area underlain by the same bedrock.

Figure 9 shows profiles of the six selected slopes, as well as the plan views and cross sections of the slip scars on the slopes. All the scars have a shallow platy form bounded by a small scar step, showing general geometry of a translational landslide (Selby, 1993, pp.260–263). These landslides seem to have resulted from the 1989 storm, since they are first visible on the aerial photograph taken in 1990.

Landslides on the slopes with same bedrocks have similar slope angles and slip depths (Table 2). The slope angles were determined from the longitudinal profiles of the slip scars. The slip depths represent mean values estimated from the vertical cross-sections of the landslides. Volumes were calculated by multiplying the mean slip depth and the sliding area. The landslides on the sandstone slopes (1.4–1.7 m in depth, 37–38° in slope angle, and 3×10^2 – 1×10^3 m³ in volume) are deeper, steeper, and larger than those on the mudstone slopes (0.6–0.7 m, 32–35°, and 4 – 5×10^1 m³).

III-2 Soil sounding and geophysical surveys

Soil soundings were conducted along the scar profiles on the S-1 (sandstone) and M-1 (mudstone) slopes, using a simplified dynamic cone penetrometer (MARUTO

Testing Machine Co., Japan). The penetrometer consists of a penetration rod with a cone tip (25-mm diameter with 60° tip angle), guide rods, and a 5-kg weight. The weight drives the cone into subsoil, falling from a height of 50 cm along the guide rod.

Here the resistance value for the cone penetration N_c is defined as the number of impacts needed for every 10-cm penetration. Using N_c -values, Wakatsuki et al. (2005) distinguished four subsurface layers: $0 \leq N_c < 5$ (upper), $5 \leq N_c < 10$ (middle), $10 \leq N_c < 30$ (lower), and $N_c \geq 30$ (bedrock). Accordingly, the thickness of soil mantle is defined as the depth attained when the N_c reaches 30.

The geophysical prospecting, refraction seismic survey and electrical resistivity investigation, provides deep subsoil information of the S-1 and M-1 slopes. The seismic velocities reflect contrasting mass densities in layered structure, whereas electrical resistivities change depending on groundwater distributions or material densities. The investigations were carried out on May 9, 2005. Total 20 mm rain fell on the slopes during May 6 to 7 prior to the operating day.

A three-channel seismograph McSEIS-3 (OYO Inc., Japan) was used to measure elastic wave velocities of both upper unconsolidated materials and intact bedrock, and to calculate depths of the seismic layer boundaries. A sledge hammer was struck onto an aluminum plate placed on the ground surface to produce a seismic signal. Travel times of the elastic waves were collected with different distances at 2-m intervals; the maximum distance is 50 m on S-1 slope and 25 m on M-1 slope.

A geo-electric apparatus Handy-ARM (OYO Inc., Japan) was used to determine subsurface resistivity distribution. Thirty-two electrodes were set out at 1.5-m or 1-m intervals following the configuration of pole-pole array. Direct current resistivity between each of the electrodes was measured and recorded. The two-dimensional

resistivity tomogram was computed with the software ElecImager/2D-Lite (OYO Inc., Japan).

III-3 Soil thickness

The sandstone slope has thick soil mantles (Fig. 10A). The value of N_c for the sandstone slope increases gradually and reaches 30 at depths of 6–7 m in maximum. The slip plane of the landslide perches on the boundary of the upper ($0 \leq N_c < 5$) and middle ($5 \leq N_c < 10$) layers. Thick soft soils (4–5 m of $N_c < 30$ layers) remain on the bedrock at the scar head of the landslide.

The soil on the mudstone slope forms a thin veneer over the bedrock (Fig. 10B). The soil thickness is up to a meter at the intact part of the slope upward from the scar head. The soft upper soil ($0 \leq N_c < 5$) has a sharp contact with the bedrock ($N_c \geq 30$) at the base of the soil layer. The slip plane of the landslides lies just above this soil–bedrock boundary. Colluvial deposit of 2–3 m thick covers the foot of the slip scar, forming a small debris tongue as a reminder of the past landslide.

III-4 Geophysical structures

The seismic refraction soundings revealed two boundaries in both S-1 and M-1 slopes (Fig. 10). The upper boundary with low elastic-wave velocities (0.8 km/s in S-1 and 0.4 km/s in M-1) indicates a base of soft soil layer or colluvial deposit, which coincides with the lower bound of the layers with small N_c -values. The lower boundary in bedrock (1.6 km/s in S-1 and 1.2 km/s in M-1) suggests a progression of deep weathering which probably causes a decrease in density of the rock masses.

Direct current resistivity tomography in S-1 slope visualizes moisture distribution

and conjectural location of the groundwater table in the bedrock (Fig. 10A). The high resistivity ($> 400 \Omega \text{ m}$) area near the slope surface represents a dry layer, where the soil-water recharged by the prior rainfall had evaporated or drained. The base of this dry layer corresponds roughly to the upper seismic boundary (0.8 km/s), suggesting different water-retention capability between loose upper soils and firm subsoil materials. The low resistivity ($< 200 \Omega \text{ m}$) region exists at the left bottom of the tomogram. Upper face of this region corresponds in level to the channel with persistent stream flow. This implies horizontal spreading of the groundwater table into bedrock.

Subsurface resistivity in M-1 slope tends to be lower than that of S-1 slopes (Fig. 10B). This indicates a relatively wetter condition or more consolidated nature of subsurface materials in the mudstone hillslope. Resistivity islands with relatively high values ($> 150 \Omega \text{ m}$) in the tomogram may reflect massive mudstone cores escaping interstitial water invasion. This resistivity distribution does not allow us to figure out much appropriate interpretations of subsurface structures, but for certain, there are no evident groundwater systems in the mudstone bedrock.

III-5 Sallow soil profiles

Soil pits were dug at three points on the scar profiles in order to inspect shallow subsurface structure (Fig. 9; pits 1 and 2 on the S-1 slope, and pit 3 on the M-1 slope). Subsurface soil profiles were recorded using exposed upslope-face of the pits (Fig. 11). The soil profiles at the scar head include a potential failure plane that corresponds to the depth of an extension of the slip surface (the schematic in the lower right in Fig. 9). In the soil profiles in pit 1 and pit 3 (at the scar heads), the depth of the potential failure planes is 70–80 cm and 50–60 cm, respectively (Figs. 11A and 11C).

The shallow soil profile of the S-1 slope consists of homogeneous sand (Fig. 11A). The N_c value in the pit 1 increases slightly with depth, but no apparent discontinuity is found around the potential failure depth. The sand at the bottom of the pit 2 (lower part of the slope: Fig. 9) holds the original beddings of the stratum (Fig. 11B). This observation indicates that the slope material in this depth originates from in-situ weathering of the sandstone bedrock.

The soil profile on the M-1 slope exhibits sharply demarcated weathering horizons (Fig. 11C). Silty organic aggregates make up a soft loose soil ($N_c < 5$) that includes scattered gravels in the uppermost 0.3 m. From 0.3 to 0.6 m deep, interlocking rock fragments form a dense residual horizon ($5 \leq N_c < 30$). The residual horizon sharply switches into the parent material below 0.6-m depth.

Chapter IV Geotechnical soil properties

IV-1 Soil sampling and geotechnical tests

Undisturbed soil cores 5.0 cm in diameter and 5.1 cm in height (100 cm^3 in volume) were extracted at every 10–15 cm depth intervals from the soil profiles. The samples from the pits 1 and 3 provided values of soil unit weight, porosity and grain-size distribution through the shallow soil layers.

Vertical profiles of the hydraulic conductivity were determined for all pits. Saturated hydraulic conductivity of soil was measured in the laboratory by a constant-head permeability test. In-situ testing of the infiltration capacity was also conducted at the bottom of the mudstone pit because of difficulty in undisturbed sampling.

The soil-water characteristic curve was determined by using the soil cores from the depths of 30 cm and 75 cm in the pit 1, and the depths of 15 cm and 30 cm in the pit 3. The samples were left in a water-poured container at least 48 hours for capillary saturation. Drying soil-water characteristic curve was then measured by a water head method for the range of pressure head from 0 to -0.6 m , and a vacuum method for the range from -0.6 to -3.9 m .

Samples for testing soil shear strength were also obtained from the pits 1 and 3 using a trimming ring of 6.0-cm bore diameter and 2.0-cm height. The dimension of the soil specimens is identical to the direct shear instrument used in this study. Sampling depth is 70–85 cm for the pit 1 (28 cores) and 35–40 cm for the pit 3 (24 cores), which is close to the depth of the potential failure plane. The moisture contents of the specimens were adjusted stepwise from an oven-dried condition to a capillary saturated condition. These specimens were delicately placed into an isometric shear box after sealing them

in a plastic bag for at least a week to allow moisture equilibration.

Direct box shear tests using the undisturbed soil specimens provided the strength parameters of the soils. Single stage shearing at a rate of 1 mm/min was conducted under four different normal stresses (10, 20, 30 and 40 kPa). The volumetric water content of the specimens was calculated from the weight difference between the specimen just after the shear test and that in completely dried condition.

IV-2 Basal soil properties

The soils on the sandstone and mudstone slopes have significant difference in their grain-size distributions (Fig. 12). Soils originating from the sandstone have a large fraction of coarse and fine sands accounting for 80–90% of the total grains, whereas soils originating from the mudstone contain finer materials accounting for 40–70% by silt and clay. The physical properties of the soils reflect this grain-size characteristic (Table 3). The soil on the sandstone slope has a greater average dry unit weight (12.7 kN/m³) and a smaller porosity (0.52) than the soil from the mudstone slope (11.1 kN/m³ and 0.58).

IV-3 Permeability

The vertical variation of the permeability depends strongly on geology. Figure 13 shows vertical profiles of the hydraulic conductivity, as well as the intensity of annual maximum 1-h rainfall in the study area. The maximum intensities of 1-h rainfall range from 5×10^{-6} to 2×10^{-5} m/s.

The permeability of the sandstone-soil shows a nearly straight vertical profile with values around 10^{-4} m/s. No discontinuity of permeability was found across the

potential failure plane, and also at transition from the shallow soil layer (pit 1) down to the bedrock (pit 2). The permeability exceeds the magnitude of annual maximum rainfall intensities, so that the rainwater will be able to percolate into deep portion of the hillslope.

The permeability of the mudstone-soil decreases significantly with depth. The value on the order of 10^{-5} m/s near the surface falls abruptly to 8×10^{-7} m/s at 0.7-m depth. Field measurement of the infiltration capacity (black squares in Fig. 13) gave the minimum permeability of 5×10^{-8} m/s at the depth of 0.9 m. The permeability below the depth of ~ 0.6 m is much lower than the maximum intensities of 1-h rainfall, suggesting that infiltrated rainwater will accumulate upon the impervious bedrock.

IV-4 Soil-water retention characteristic

The soils originating from the two parent materials have different soil-water retention characteristics (Fig. 14). The volumetric water content of the sandstone-soil falls smoothly from 0.47 to $0.2 \text{ m}^3/\text{m}^3$ as the pressure head decreases from 0 to -1 m, and then settles in a residual state as the soil contains only suspended water. The soil on the mudstone slope rapidly drains water before the pressure head decreases to -0.5 m. However, the soil maintains relatively high volumetric water content around $0.35 \text{ m}^3/\text{m}^3$ even when the pressure head becomes -4 m.

The broken and solid lines in Fig. 14 show the best-fit model curves. An equation of van Genuchten's (1980) model modified by Kosugi (1994) was adopted:

$$\theta = \theta_r + (\theta_s - \theta_r) \left[1 + m \left(\frac{\psi}{\psi_0} \right)^{\frac{1}{1-m}} \right]^{-m} \quad (1)$$

where θ is the volumetric water content, θ_s is the saturated volumetric water content, θ_r is the residual volumetric water content, ψ is the pressure head, ψ_0 is the pressure head at the inflection point of the model curve, and m is a fitting parameter ($0 < m < 1$). In this case, the air-entry value of the soil is assumed to be zero, because the specimens drain gravitational water promptly after the onset of negative pressure heads (Fig. 14).

Equation (1) was fitted to the data by non-linear least squares optimization based on Marquardt (1963). A software program for the non-linear regression conducted the fitting by an iterative computation for minimizing the residual sum of squares of the model curves versus observed datasets. The value of θ_s was fixed on the volumetric water content at the zero-pressure head, and the other parameters, i.e., θ_r , ψ_0 and m , were estimated by the regression.

The fitting analysis provided the optimum parameter values in Table 4. The model curves using these values accurately represent the soil-water retention characteristics of each soil: $r^2 = 0.98$ and 0.95 for sandstone, 0.95 and 0.99 for mudstone (see also Fig. 14). The values of θ_s and θ_r are similar to those in a previously published catalog for silt loams: $\theta_s = 0.44$ – 0.55 and $\theta_r = 0.01$ – 0.28 (Mualem, 1976). The magnitudes of ψ_0 for the sandstone-soils are also similar to those in Kosugi (1994): $-9 \times 10^{-1} \text{ m} \leq \psi_0 \leq -2 \times 10^{-1} \text{ m}$. However, ψ_0 for the mudstone-soil is significantly closer to 0 m than the previously reported values, as a result of the rapid water drainage in a

near-zero negative pressure head.

IV-5 Shear strength

The shear tests revealed the characteristics of decline in soil shear strength with increasing moisture content. Table 5 and Fig. 15 show the test results for the specimens with varied moisture conditions. The specimens were categorized into the six moisture levels from oven-dried to capillary saturated conditions: groups A to F in the sandstone-soil, and groups G to L in the mudstone-soil (Table 5). Solid lines in Fig. 15 indicate the results of a linear-regression for each specimen group. Inclination and y-intercept of the lines correspond respectively to the angle of shearing resistance and the cohesive strength for each moisture group.

The angles of shearing resistance for both soils decreased drastically from the largest value in the driest condition to nearly a constant value at wetter conditions (Table 6, Fig. 15). Figure 16A shows the relationships between the average volumetric water content in each group and the angle of shearing resistance. The groups A and G, the driest condition, show a significantly large angle of shearing resistance of 48.4° and 53.3° , respectively. The group H in the mudstone-soil also represents a large value of 47.7° , but this inclination seems to be affected by the result for normal stress of 40 kPa (Fig. 15, Table 5). The other moisture conditions, the groups B to F and the groups I to L, show the angles of shearing resistance within a narrow range in 25° – 33° for the sandstone-soil and 27° – 31° for the mudstone-soil (Table 6).

The cohesive strength decreased with increasing moisture content and approached a minimum value at saturated condition (Table 6). Figure 16B shows the relationships between the average volumetric water content and the soil cohesion in each group. The

cohesive strength of the soils decreases exponentially with increasing volumetric water content.

The reduction characteristics of the soil shear strength (Fig. 16) suggest the following presumptions: (1) the angle of shearing resistance takes a constant value independent of volumetric water content of the soil, (2) the soil cohesion is an exponential function of volumetric water content. These presumptions lead to a formulation of the decrease in soil shear strength:

$$\tau = Ce^{-\mu\theta} + \sigma \tan \phi \quad (2)$$

where τ is the shear strength, C is the apparent soil cohesion at dry condition, μ is the reduction coefficient, σ is the applied normal stress, and ϕ is the apparent angle of shearing resistance. Note that C is a hypothetical ultimate value when $\theta = 0$; an increase in μ causes a significant reduction of cohesive strength.

Equation (2) is consistent with the existing discovery that only the cohesive component decreases with increasing soil moisture (Fredlund et al., 1978; Escario and Sáez, 1986; Gan et al., 1988; Vanapalli et al., 1996; Miao et al., 2002; Lee et al., 2003). The previous studies employed a function of matric suction as a parameter of soil moisture conditions. The matric suction in a soil is defined as pore-air pressure minus pore-water pressure, which cannot be determined accurately in our shear tests. Therefore, Eq. (2) is used as an approximate formula for evaluating the reduction in shear strength of an unsaturated soil.

In the analyses, the test results of the driest conditions were excluded (groups A and G, Table 5). This is because the angle of shearing resistance in these conditions was

significantly larger than that of the wetter conditions (Fig. 16A, Table 6). The reason for this phenomenon is so far unclear, but cementation of fine materials and/or shrinkage of the soil mass might contribute to enlarge frictional resistance of the soils in an excessively dried condition. The present study targets only soils under moist conditions of which the value of ϕ can be assumed to be constant.

To determine the values of unknowns (i.e., ϕ , C and μ), Eq. (2) should be linearized as follows:

$$\ln[\tau - \sigma \tan \phi] = -\mu\theta + \ln C. \quad (3)$$

The left side of the equation represents logarithm of the cohesive component of the shear strength. This equation allows us to execute a multiple linear-regression analysis following the procedure described below:

1. Assign an arbitrary value to ϕ ,
2. Compute the term $\ln[\tau - \sigma \tan \phi]$ for every dataset of τ and σ ,
3. Conduct a simple linear-regression for the datasets of $\ln[\tau - \sigma \tan \phi]$ and θ ,
4. Repeat 1 to 3 to seek the most suitable value of ϕ , which yields the highest correlation coefficient,
5. Compute the value of C and μ from the y-intercept ($\ln C$) and inclination ($-\mu$) of the regression line with the best-fit ϕ .

Results of the regression analyses are described in two stages as Fig. 17. Figure 17A shows the changes in square of correlation coefficient of Eq. (3) with respect to varying ϕ . The correlation reaches a peak at $\phi = 28.3^\circ$ for the sandstone-soil, and at

27.7° for the mudstone-soil. Substituting the most suitable values of ϕ , the relationships between $\ln[\tau - \sigma \tan \phi]$ and θ were obtained as shown in Fig. 17B.

The parameters obtained by the regression are listed in Table 7. The variables in the equations reflect liquefaction characteristics of the soils and susceptibility to changes in pore-water pressure during shear deformation. Therefore, one must regard these values as purely empirical rather than physically significant. Nonetheless, the equations using these soil-specific parameters accurately represent the observed strength reduction characteristics of each soil (Fig. 18).

Figure 19 compares the measured and calculated shear strength. In the diagram, values of SE (standard error of estimate) are defined as a standard deviation of the predictive residuals. The smaller value of SE indicates the more accurate prediction. The values of SE were 2.67 kPa for the sandstone-soil, 4.25 kPa for the mudstone-soil. Of note is that the SE in the mudstone-soil was significantly affected with the anomalous shear strength value (an arrowed plot in Fig. 19). This plot is the test result with normal stress of 40 kPa in the group H (Table 5, Fig. 15). Discounting the outlier, the SE for the mudstone-soil comes down to 1.29 kPa.

Chapter V Slope hydrology

V-1 Methods of hydrological observations

Tensiometers with pressure transducers (RSUxx, IRROMETER Co. Inc., USA) were set-up within 10 meters upslope from the scar head on S-1 and M-1 slopes to monitor responses of pressure head in hillslopes to rainfall (Fig. 9). All tensiometers were calibrated at laboratory before the installations within ± 0.01 m precision of pressure head. Two nests of tensiometers were established on the S-1 slope (ST1 and ST 2, with ceramic cups at depths of 30, 75, and 120 cm). Three nests were set-up on the M-1 slope (MT1, MT 2 and MT 3; depths of ceramic cups were 30 cm for MT1, 23 cm and 46 cm for MT2, and 30 cm, 60 cm, and 90 cm for MT3). A data logger connected to the pressure transducers recorded the subsurface pressure head at every 10 minutes.

A soil moisture sensor (ThetaProbe TYPE ML2x, Delta-T Devices Ltd., UK) was installed to monitor subsurface volumetric water content at 75 cm depth at ST 2 and at 60 cm depth at MT 3. The output from the sensor, dielectric constant of soil, was collected with a data logger in 10-minute intervals. The recorded dielectric constants were converted to volumetric water content with ± 0.02 m³/m³ precision by a laboratory calibration using the native material from the monitoring depths.

The simultaneous monitoring of pressure head and volumetric water content at a corresponding depth permits to draw an 'in situ' soil-water characteristic curve including hysteresis between drying and wetting processes of the soils. Therefore, the 'in situ' curve makes it possible to estimate the ranges of alteration in the 'laboratory' parameters for soil-water retention characteristics (Table 4).

A small watershed was selected in each area to monitor rainfall–runoff responses (Figs. 8B and 8D). The sandstone watershed (hereinafter called S-watershed) maintains a stable base flow of 0.2–0.3 L/s welling from a spring at 5 m upstream from the catchment outlet (Fig. 8B). The downstream channel floor is inundated with saturated sediment resulting from the groundwater seepage. Behind the spring, soil-mantled slopes with no slip scars form an unchanneled dry hollow. In the mudstone watershed (M-watershed), a channel with well-defined banks incises the bottom of the watershed (Fig. 8D). The channel lacks a stream flow except for a short period during rainfall events. The upstream end of the ephemeral channel branches into tributaries and extends to the convergent hollows. Several hillslopes near the deep channel underwent slipping, exposing the mudstone bedrock. Most slopes in the watershed have much thinner soil cover, and some have only organic deposits on the bedrock.

Runoff was measured at the watershed outlet by means of a weir and a capacitive water-level probe (UIZ–CA050, UIZIN Co., Japan). The flow depths in the weir were recorded with a data logger at 10-minute intervals. The observed water level was converted into a discharge using an in-situ calibration curve.

Rainfall at 10-minute intervals was also observed at the points denoted with stars in Figs. 8A and 8C. A tipping-bucket rain gauge with a data logger was placed at open site of tree crowns on the forested slopes. The gauge has an orifice diameter of 20 cm and stood approximately 60 cm above the forest floor. Recorded bulk rainfall includes no effect of interception by surrounding understory vegetation, but may have little influence of a projection by tree canopies.

The pressure head, runoff and rainfall were observed from May 2004 to July 2005. The data of volumetric water content of soil are available from February to August

2005. All of the observations included temporal respites during extremely dry periods or downtimes when loggers are filled up with data.

V-2 Long-term fluctuations of pressure head and rainfall–runoff characteristics

The pressure heads in the sandstone slope show a small range of fluctuations (a band of ± 0.5 m below zero-pressure head) throughout the observation period (Fig. 20A). The pressure head at the deepest points (depth 120 cm) maintained negative values up to -0.2 m even during intensive rainfall events. Pressure head at the shallowest monitoring depth (30 cm) momentarily exceeded 0 m only at rainfall peaks.

Runoff from the S-watershed did not respond to individual storms. The watershed maintained a stable discharge less than 0.5 L/s, with slight fluctuations on a rather long timescale. The low discharge was verified by field observations during a rainfall event.

The pressure head on the mudstone slope varied over a wide range during the observation period from negative values of -2 m to positive values up to 0.5 m (Fig. 20B). The pressure head reached positive values in response to almost all rainfall events at every depth. A marked decrease in the pressure heads followed until the next rainfall, especially during dry summer months. The pressure heads between the events oscillate diurnally because of the evapotranspiration cycles.

Runoff from the M-watersheds responded sharply to rainfall events. The accurate magnitudes of several peak flows could not be measured because of overflows. Following these extremes, the discharge fell rapidly as rain stopped and declined to zero after a few days when the pressure head in the slope decreased to a negative value.

V-3 Short-term response of pressure head to rain infiltration and subsurface water behavior

The pressure-head fluctuation from May 19 to 21, 2004 is a typical response to a rainfall event. Pressure heads observed during the other rainfall events show similar changes to those in this period. Thus the data during the three days are presented as a representative of short-term hydrological responses of the slopes (Figs. 21A and 21C). Figures 21B and 21D illustrate the distributions of the hydraulic head and the saturated zone at the timings of four arrows in Figs. 21A and 21C.

The pressure heads in the sandstone slope responded to rainfall sequentially from shallow (30 cm) to deep monitoring depths (120 cm) (Fig. 21A). The time lags in the rising edges of the pressure head between 30 cm and 75 cm depth, and between 75 cm and 120 cm depth were about six hours for the first event on May 19. The time lags became shorter (~1–4 hour) for the subsequent rainfall on May 21. In addition, the pressure heads rose abruptly at shallower depths but more gradually at deeper points.

The equipotential lines of hydraulic heads in the sandstone slope tended to be horizontal in absence of significant saturated zones (Fig. 21B). Accordingly, unsaturated gravitational water flow dominates the subsurface water transportation. This vertical rainwater percolation should recharge the deep groundwater body in the permeable bedrock (Fig. 10A). Indeed, no perceptible responses in runoff were observed (Fig. 20A). Infiltrated rainwater discharges to the stream through the deep aquifer on a long-term basis, giving the observed constant base flow.

The pressure heads in the mudstone slope rose nearly concurrently with rainfall and reach positive values at all monitoring depths (Fig. 21C). The sharp increases in the

pressure heads began from the deepest point and rapidly moved to shallower depths, indicating a rise in the saturated zone from the bottom to top. The positive pressures persisted for several hours at 30-cm depth, but several days at 90-cm depth.

The resultant hydraulic head lines under the saturated regime tended to be perpendicular to the slope, indicating downslope water movement upon the impermeable bedrock (Fig. 21D). This subsurface lateral flow drained rainwater through the soil layer out to channel systems, giving acute runoff peaks in response to every rainfall event (Fig. 20B). In fact, discharge from the watershed continued while the pressure head in the slope maintains a positive value, and declines as the pressure head reverts to a negative value.

V-4 In situ soil-water retention characteristics

Figure 22 shows the responses of soil moisture and pressure head to rainfall at the corresponding monitoring depth. Volumetric water content θ in the sandstone slope responded widely to rainfall ranging from 0.2 to 0.35 m³/m³, although the pressure head ψ fluctuated within a relatively narrow range from -0.8 m up to -0.2 m (Fig. 22A). The soil on the mudstone slope maintained a moist state ($\theta > 0.46$ m³/m³) over the winter and spring months (Fig. 22B). In summer, the volumetric water content decreased below 0.28 m³/m³ in minimum after several dry days. Acute rises of volumetric water content up to 0.53 m³/m³ were observed when the slope became saturated ($\psi > 0$).

The observed volumetric water content plotted against the simultaneous pressure head indicates the 'in situ' soil-water retention characteristics (Fig. 23). The best-fit model lines for the drying curve from the laboratory data (Fig. 14, Table 4) were also

presented in the diagrams (solid and broken thin lines).

The in situ data from the sandstone slope sit on the immediate lower-right of the drying soil-water characteristic curves (Fig. 23A). The upper edge of the in situ plots corresponds to the drying curves, so that the observed data indicate the range of hysteresis between drying and wetting processes of the soil. The values of θ observed in situ were approximately $0.1 \text{ m}^3/\text{m}^3$ lower than the drying curve in maximum. The gray bold lines on an opposite side across the plots represent the envelopes covering the gap between the laboratory curves and in situ-observed data. The envelope for the plots covers the divergence originating from the drying–wetting hysteresis. Parameter values for these envelopes are listed in Table 8.

The in situ soil-water retention characteristic at the mudstone slope differs markedly from the laboratory curves (Fig. 23B). Although the laboratory curves and the in situ data exhibit similar values and changing trends at near-zero pressure head, the in situ data track a more water-retentive path to drying. This may result from disparity in soil texture through the soil profile (Fig. 11C), between shallower sampling points for laboratory tests (the depths of 15 cm and 30 cm) and the deeper zone for the in situ observation (60 cm depth). The upper envelope of the plots covers such a spatial variance in the soil-water retention characteristic.

Chapter VI Discussion

VI-1 Landslide mechanisms

VI-1-1 Slope stability analysis

The landslides on the observed slopes have a shallow slip plane oriented parallel to the original slope surface (Fig. 9). The slip scars have the geometry of an ellipsoidal plate of which the depth is much smaller than width or length. Hence, an infinite-slope stability model was employed to analyze the critical conditions for landsliding (Fig. 24). The analysis neglects all forces not resolvable on a potential failure plane that parallels the ground surface. Reinforcement by piling and lateral tree roots was also not taken into account, because the potential failure plane in the actual soil profiles lies well below the major root zone (Figs. 11A and 11C).

In a limit equilibrium concept, materials on an elongated slope are subject to two opposing forces: a downslope component of soil weight as a driving force, and shear strength of the soil providing a resisting force (Fig. 24). The dimensionless factor of safety FS balances them as:

$$FS = \frac{\text{Resisting force}}{\text{Driving force}} = \frac{\text{Shear strength of soil}}{\text{Downslope component of soil weight}}. \quad (4)$$

If FS reduces below unity, the slope fails along the potential failure plane.

Three instability factors were taken into account: (1) reduction of soil cohesion in response to soil wetting, (2) weight increase of soil resulting from water absorption, and (3) decrease in effective stress derived from pore-water pressures. The first two

were considered only in an unsaturated state, because the values of soil cohesion and soil unit weight are fixed at a saturated condition. The third factor works only when the pressure head in the soil reaches a positive value.

Assuming an equable wetting of homogeneous soil, i.e., uniform soil water content and pressure heads from the land surface to the slip plane, FS is expressed as:

$$FS = \frac{Ce^{-\mu\theta} + \{(\gamma_d + \theta\gamma_w)Z \cos^2 \beta - \text{Max}(\psi, 0)\gamma_w\} \tan \phi}{(\gamma_d + \theta\gamma_w)Z \sin \beta \cos \beta} \quad (5)$$

where Z is vertical soil depth, β is slope angle, γ_d is the dry unit weight of soil, and γ_w is the unit weight of water (9.8 kN/m³). Equation (5) can be algebraically split into three components as:

$$FS = \frac{\tan \phi}{\tan \beta} + \frac{Ce^{-\mu\theta}}{(\gamma_d + \theta\gamma_w)Z \sin \beta \cos \beta} - \frac{\text{Max}(\psi, 0)\gamma_w \tan \phi}{(\gamma_d + \theta\gamma_w)Z \sin \beta \cos \beta}. \quad (6)$$

The first term on the right side of Eq. (6) represents the frictional component of slope stability. The second term expresses the changes in cohesive resistance in an unsaturated state (on the basis of Eq. (2)). The third term refers to slope instabilization by the positive pressure head in a saturated state ($\psi > 0$ m). Substitution of Eq. (1) into Eq. (6) generates the factor of safety mediated by the pressure head, and allows a simulation of slope instabilization for both unsaturated and saturated conditions.

The moisture condition of soil between the land surface and the slip plane is not actually uniform. Soil moisture in an unsaturated slope during an intensive storm

decreases with increasing depth because of rainwater infiltration from the land surface. Thus Eq. (6) may underestimate slightly the weight of soil mass in an unsaturated condition. However, this underestimation has much smaller influence on *FS*-values than the other parameters in the stability equation (Borga et al., 2002; Dykes, 2002). Hence, the following analysis ignores the subtle effect of the weight heterogeneity in the soil column.

VI-1-2 Critical conditions for landsliding

The slope stability analysis was applied to specify the critical conditions of the past landslides whose scars are described in Fig. 9. Slip depths and slope angles of the landslides, and the other input-variables for the analysis were already identified (Tables 2 to 4, 7 and 8). Hence, the factor of safety in those slipped slopes can be simulated as a function of the pressure head at the slip plane. Parameters for soil-water characteristic curves (Eq. (1)) were assigned in three ways for each soil: two laboratory curves from different sampling depths (Table 4), and the parameter set for in situ envelopes (Table 8).

Figure 25 juxtaposes curves showing the results of the stability simulation. Factor of safety reduce with an increase in pressure heads. The *FS*-values for each of the three slopes with the same bedrocks decrease with a similar pattern from an unsaturated to a saturated condition. The similar *FS*-values result from the similarity of the slip depths and slope angles in each of the sandstone and mudstone landslides (Table 2).

The variation of the soil-water characteristic curves transmutes delicately the shape of *FS*-tracks in unsaturated states. However, the parameters for soil-water retention do not affect the *FS*-values in saturated conditions. This is because the volumetric water

content of soil takes a constant value under saturated regimes.

Factors of safety for the sandstone slopes show relatively low values, for example, around 2.0 at -0.9 m pressure head. The low FS -values result from a relatively deeper (~ 1.7 m) and steeper ($\sim 38^\circ$) geometry of the landslides. Factors of safety for the sandstone slopes fall below unity just before the saturation with $-0.14 \text{ m} \leq \psi \leq -0.01$ m (Fig. 25A). This result implies that the sandstone slopes failed under an unsaturated condition without positive pressure heads.

The mudstone slopes maintain a highly stable state, for example, around $FS = 4.0$ at -0.9 m pressure head. The relatively shallower slip depth (~ 0.7 m), gentler slope angle ($\sim 35^\circ$), and also cohesive characteristic of the soils (Fig. 17B, Table 7) are responsible for the stable condition of the unsaturated mudstone slopes. Factors of safety become 1.7–1.8 even at the saturation point ($\psi = 0$ m), and sink below unity when the pressure head reaches 0.7–0.8 m (Fig. 25B). This indicates the completely saturated landsliding of the mudstone slopes.

VI-1-3 Hydrological triggering of the landslides

In the sandstone slope, infiltrated rainwater can seep down vertically through the soil layers into bedrock, because there is no discontinuity of permeability in the subsurface profile (Fig. 13). The thick soil layer on the permeable bedrock cannot reach a saturated state (Fig. 20A). In this case, a wetting front migrates from land surface into subsoil without a positive pressure head (Figs. 21A and 21B).

The unsaturated redistribution of rainwater causes reduction in cohesive strength of the slope materials (Fig. 18). The critical pressure heads for the sandstone slopes were calculated to be negative values (Fig. 25A). The stability simulation proves that the

sandstone slopes do not require positive pressure heads for landsliding. These facts indicate that the wetting front migration by intense rainwater infiltration causes an unsaturated landslide associated only with the reduction in soil cohesion.

Forefront of the down-seeping wetting band locates the slip plane of this type of landslide. The same concept of landslide initiation is supported by a numerical simulation of subsurface rainwater diffusion (Collins and Znidarcic, 2004). The landsliding on the sandstone slope is controlled by whether or not the wetting front reaches deep enough to form a failure plane.

The impermeable bedrock beneath a rather permeable soil layer prevents the percolation of rainwater in the mudstone slopes (Fig. 13). The thin overburden becomes a saturated state with a relatively small amount of rainfall (Fig. 20B). This results in a generation of positive pressure heads, building up a shallow transient groundwater table (Fig. 21D).

The pressure head in the mudstone slope responds promptly to rainfall, reaching a positive state in a short period (Fig. 21C). This hydrological response lends support to the concept of efficiency of pore-pressure transmission associated with slope-normal rainwater infiltration (Iverson, 2000). It also implies that the concept of the steady-state groundwater flow is not appropriate to assess the direct triggering of landslides, even where the hillslopes are underlain by impermeable bedrock. In fact, landslides in the mudstone area took place on uppermost hollows (Matsushi and Matsukura, 2004) without large contributing areas assumed in the steady-state model.

The mudstone slopes become a critical condition when the pressure head reaches a positive value of 0.7–0.8 m (Fig. 25B). The critical pressure head in the mudstone slopes slightly exceeds the thickness of the landslides (Table 2). This indicates that the

slopes failed under a condition of high pore-pressures in excess of hydrostatic maximum level generated by total saturation of the soil matrix. Such a localized increase in pore pressures may be produced by preferential water flows in the soil layer as demonstrated by Pierson (1983).

Water flows through macro pores in a soil layer affect hillslope stability. Rapid discharge through a preferential conduit contributes to stabilizing a slope by increasing the rate of soil drainage. On the contrary, when the passageway is blocked by sediment and/or fills with water, generation of pore-water pressures in surrounding matrix induces slope instability (Uchida et al., 2001). However, the field inspections as well as the results of hydrological observations in the present study did not clarify that a particular passageway of infiltrated rainwater contributes to destabilizing the hillslopes.

Whatever the case, the positive pressure heads corresponding roughly to the soil depth instigates a decrease in effective stress at the slip plane. The reduction of effective stress in a maximum possible level in addition to the loss of soil cohesion triggers a soil slip upon the impervious bedrock. This indicates that the maximum possible pressure head causes a landslide with the minimum thickness, provided that adequate depth of soil has developed on the bedrock.

Figure 26 illustrates the time-domain alterations in subsurface moisture and stress states above permeable and impermeable bedrocks. The failure mechanisms were illustrated schematically on the basis of the subsurface water behavior (Figs. 21B and 21D) and the critical conditions for landslide initiation (Fig. 25). In the sandstone slope, the thick soil layer on the permeable bedrock cannot reach a saturated state (Fig. 26A). In this case, wetting front migration causes reduction of cohesive strength, and the

slope material fails when the shearing resistance drops below the shear stress without positive pressure head. In the slope with impermeable mudstone, the thin overburden becomes saturated with a relatively small amount of rainfall, forming a transient groundwater table (Fig. 26B). As a result, in addition to the reduction in soil cohesion, a decrease in effective stress caused by positive pressure head triggers a soil slip upon the bedrock.

These mechanisms of landslide initiation are verifiable through the rainfall amount of the landslide-triggering storm on August 1, 1989. Total rainfall of 250 mm, 300 mm, 450 mm, and 350 mm fell respectively at Yokohama, Kisarazu, Sakuma, and Sakahata from the beginning of rainfall on July 31 (Fig. 5). Rainfall provided to the studied hills during the storm course can be estimated as ~ 340 mm from the average of these records.

The pre-storm moisture conditions can be estimated from the pressure head observation during irrigation intervals as ~ -0.5 m for the sandstone slope, and < -1 m for the mudstone slope (Fig. 20). These pressure heads correspond to volumetric water contents of $0.20 \text{ m}^3/\text{m}^3$ and $0.35 \text{ m}^3/\text{m}^3$, respectively (Fig. 23). Considering the saturated volumetric water contents of $0.47 \text{ m}^3/\text{m}^3$ for the sandstone-soil and $0.53 \text{ m}^3/\text{m}^3$ for the mudstone-soil (Table 4), total saturation of the soils requires water inputs of $0.27 \text{ m}^3/\text{m}^3$ and $0.18 \text{ m}^3/\text{m}^3$, respectively.

Depths of the landslides are 1.4–1.7 m for the sandstone slopes, and 0.6–0.7 m for the mudstone slopes (Table 2). The saturation of the soil column needs a rainfall amount of 380–460 mm for the sandstone slopes and 110–130 mm for the mudstone slopes. The total rainfall provided by the storm (~ 340 mm) did not match up the requirement of the saturation of the sandstone-soil, but sufficed for the complete

saturation of the mudstone-soil. These estimates support the concepts of the landslide mechanism in each hillslope (Fig. 26).

VI-1-4 Implication of the landslide-triggering mechanisms to landslide locations and hill morphologies

The landsliding with negative pressure heads usually occurs on hillslopes where the slope angles are steeper than the angle of shearing resistance of the slope material (Rao, 1996). This is because the frictional component in resisting force bears the stability of slopes, even if the cohesive strength completely vanishes away. Slopes gentler than the angle of shearing resistance can slip only when the ascending force acts on the potential failure material (Iverson and Major, 1986). However, such a buoyancy effect is not expected for the sandstone slopes, because of the absence of the positive pressure heads (Figs. 20A and 21A).

The angle of shearing resistance is 28.3° for the soil on the sandstone slope (Table 7). Indeed, landslide locations in the sandstone area are confined to the steep ($> 30^\circ$) lower parts of the hillslopes (Matsushi and Matsukura, 2004). Thus, landslides do not erode the gentle (typically $< 20^\circ$) upper slopes, even where the thick soil mantles has developed on the bedrock. This confinement of landslide locations may result in the preservation of relatively high rounded hillcrests in the sandstone area (Fig. 3).

Generation of positive pressure head can triggers landslides even on relatively gentle parts of the hillslopes, provided that adequately thick soil has developed on the bedrock. Consequently, the soil thickness controls the landslide occurrence, rather than slope angles in the mudstone hillslopes. The similar slope condition was reported in a tropical rainforest in Brunei, where intensive rainstorms often hit the hillslopes (Dykes,

2002); only a thin soil layer covers the steep hillslopes of the rainforest, because of the continuous soil removal by shallow landsliding. In a similar way, the mudstone area has been eroded at a rate equivalent to the rate of bedrock weathering, maintaining only thin overburden on the hillslopes.

Convergent hollows become the most feasible locations for the shallow landslides in the mudstone hill, since they accumulate sediment from surrounding ridges or side slopes in addition to the in-situ soil production from the bedrock (Reneau and Dietrich, 1987; Reneau et al., 1989, 1990; Yamada, 1999; Sasaki et al. 2000). Landslides on the uppermost hollows probably spread their effect toward the hillcrest. The mudstone hillcrests show a narrow bedrock-dominant edge, which is likely to be affected by headward erosion of valley slopes. Dissection of the ridge crests by the frequent landsliding of the hillslopes located on either side of the ridge line may be responsible for evolving the rugged hilly landscapes (Figs. 1 and 3).

VI-2 Rainfall thresholds for landsliding

VI-2-1 Changes in factor of safety during rain storms

The slope stability analysis using Eqs. (6) and (1) allows us to pursuit stability fluctuations of the studied slopes (Fig. 27). The factors of safety were calculated from the observed pressure head at each monitoring depth with local slope angles (38.8° for ST2, 35.7° for MT3). The two sets of parameters for soil-water characteristic curves were used in the calculation: the set for deeper samples in each soil as a representative of the laboratory curves (at 75-cm depth for the sandstone, 30-cm depth for the mudstone, Table 4), and the set for in situ envelopes (Table 8). Other parameters in the equations were assumed to be constant over the depth, being fixed on the values in

Tables 3 and 7.

The factor of safety in the sandstone slope shows a similar temporal variation in the cases using the laboratory and in situ parameters for the assumed soil-water characteristic curve (Figs. 27A and 27C). *FS*-values at 30-cm depth in the sandstone slope sharply falls from 4.0–6.0 to nearly 2.0 during every rainfall events, whereas those at depths of 75 cm and 120 cm respond more slowly with a narrow range of fluctuations around $FS = 1.0$ –3.0. The sensitive responses at the shallow zone are induced by soil wetting from land surface. The subsequent rainwater redistribution causes the instability in the deeper zones. The deepest point (120 cm) consistently exhibits the low *FS*-values below 2.0, indicating the unstable predisposition of the sandstone slope.

The changing patterns of *FS* in the mudstone slope differ with the setting parameters for the soil-water characteristic curve. *FS*-values fluctuate within a relatively wide range at the all monitoring depths, in the case using the laboratory parameters (Fig. 27B). Even at deeper points (60 cm or 90 cm), *FS* maintains relatively large values around 3.0–4.0 during intervals of rainfall events. *FS*-values in the case using the in situ parameters exhibit a relatively narrow range of fluctuations, especially in winter to spring months below 2.0, at depths of 60 cm and 90 cm (Fig. 27D).

The difference in *FS*-values with the in-situ and laboratory soil-water retention characteristics results from the water-retentive tendency of the in situ curve (Fig. 23B). However, in both cases, positive pressure heads under a completely saturated condition causes the eventual destabilization of the mudstone slope, reducing the factors of safety to nearly the stability limit of $FS = 1$. Hence the difference between the laboratory and in situ parameters does not affect the *FS*-values for the near-critical

state in the mudstone slope.

VI-2-2 Analysis of the relationship between the magnitudes of rainfall and slope instability

The factor of safety decreases transiently, forming a temporal depression in response to an individual rainfall (Fig. 28A). Relation between the magnitude of rainfall events and the minimum *FS*-values was analyzed at the deepest monitoring depths which are located roughly on an extension of the slip surface (ST2: 120 cm; MT3: 90 cm). The analysis for the sandstone slope was performed for the two origins of *FS*-values, from the laboratory and in situ soil-water retention curves, for evaluating the hysteresis effect in soil wetting. This dual analysis makes no sense in the case of the mudstone slope, because the minimum *FS*-values appear under completely saturated conditions.

The dimple of the *FS*-value develops with a delay from the rainfall peak. Rainfall over a specified time period prior to the dimple appearance affects the minimum *FS*-values. Hence the mean rainfall intensities during the preceding x hours were calculated (Fig. 28A), where x is a series of 28 time frames of rainfall: 0.5, 1, 2, 3, 4, 5, 6, 8, 10, 12, 14, 16, 18, 20, 24, 30, 36, 48, 60, 72, 84, 96, 108, 120, 132, 144, 156, and 168 h. The datasets of the minimum *FS*-value and the 28 types of mean rainfall intensity can be obtained from every rainfall event which renders transiently the slope unstable.

The minimum factor of safety becomes smaller with increasing magnitude of rainfall. Hence the minimum *FS*-value correlates inversely with the mean intensity of the preceding rainfall (Fig. 28B). The relationships were examined sequentially through the 28 rainfall durations with varying time periods. The correlation becomes

strongest at rainfall duration of x_i h, indicating the x_i -h rainfall reduces the factor of safety most effectively.

Changes in the correlation coefficients make a mound with a peak at x_i -h rainfall duration (Fig. 28C). The rainfall duration at the correlation peak tends to be shorter where fast subsurface water movement occurs in the slope, whereas it becomes longer where slow rainwater percolation or antecedent moisture condition controls the stability of the slopes. Therefore the effective rainfall duration for slope instability should change with hydrological processes in the hillslope.

A certain significant level (S.L.) classifies statistically the effective and ineffective rainfall durations (Fig. 28C). In a linear-regression analysis, coincidence of a regression function for a certain dataset can be tested by the magnitude of correlation coefficient $|r|$. A probability P gives the quantitative likelihood of the regression function, which is defined as the probability that the correlation coefficient for a set of independent variables exceeds the observed $|r|$ statistic (Taylor, 1997, pp. 224–226). If P exceeds a given $\alpha\%$, the correlation will be rejected at the $\alpha\%$ significant level. In the present study, the effective durations of rainfall were approved by the S.L. at which the P -value falls below 0.001%.

Relations between the minimum FS -value and mean rainfall intensity in the effective durations provide the statistically significant regression functions (Fig. 28D). The critical rainfall for stability limit is defined by an intersection of the linear-regression line and the horizontal line of $FS = 1$. The value of critical rainfall has a range of $\pm 1\sigma$ uncertainty from 68% confidence limits of the linear regression. Landsliding is expected when the mean rainfall intensity for a given rainfall duration reaches the critical level.

Results of the analysis show different effective duration and critical intensity of rainfall between the sandstone and mudstone slopes (Fig. 29). Total 24 events were collected for the regression analysis for the sandstone slope (Fig. 29A). The strongest correlation appeared in the rainfall duration of 72 h in both analyses using the laboratory (open circles) and in-situ parameters (triangles) for the soil-water characteristic curve. The dual analysis provides the two critical rainfall intensities in the 72-h duration, 2.6 mm/h (range of $\pm 1\sigma = 2.1\text{--}3.2$ mm/h) for the laboratory parameters, and 3.4 mm/h (range of $\pm 1\sigma = 2.9\text{--}4.1$ mm/h) for the in situ ones. In the mudstone slope, the analysis for 49 events shows that 5-h rainfall duration is most effective in destabilizing the slope (Fig. 29B). The critical rainfall for the duration of 5 hours has the mean intensity of 14.3 mm/h (range of $\pm 1\sigma = 11.2\text{--}18.8$ mm/h).

The regression coefficients for the sandstone slope show diphasic changes with the varying rainfall durations (the inset of Fig. 29A). First peak of the correlation arises at 14 h, and the slightly higher second one appears at the 72-h rainfall duration. This indicates that the antecedent moisture condition plays a key role in instability of the sandstone slope, associated with rainfall for time periods about 3 days prior to an instability peak. The 14-h rainfall may be relevant to direct triggering of the shallow landslide.

The mound of correlation coefficient for the mudstone slope forms a single-peak pattern (the inset of Fig. 29B). The correlation peak occurs at 5-h rainfall, and durations from 2-h to 16-h gives statistically significant correlations. This suggests that rainfall during a relatively short period from several hours to half a day controls the slope destabilization. However, even in this case, antecedent moisture also contributes to the slope instability. Influence of the antecedent moisture condition may yield the

markedly-scattered plots in the regression for the mudstone slope (Fig. 29B).

VI-2-3 Critical combinations of rainfall intensity and duration

The statistically significant correlations were available for the rainfall durations from 8 h to 84 h in the sandstone slope, and from 2 h to 16 h in the mudstone slope (Fig. 29). The regression analyses for all of these effective durations provide the critical mean intensities as plotted in Fig. 30. For all points, the critical intensities of rainfall decrease with increasing rainfall duration.

The critical rainfall intensities for the sandstone slope (open circles and triangles) are higher than those for the mudstone slope (solid circles) within a same duration of rainfall. For example, critical mean intensity of 10-h rainfall is ~9 mm/h for the mudstone, whereas the sandstone slope requires 15–20 mm/h for the same duration. Accordingly, the landslide on the mudstone slope occurs with the smaller amount of rainfall than that on the sandstone slope.

The two arrays of critical rainfall from the dual analysis for the sandstone slope exhibit a similar magnitude, but show slightly larger intensities in the results from in situ parameters (triangles) than those in laboratory ones (open circles). The in situ envelope of the soil-water retention involves wetting paths starting from a relatively dry condition, whereas the laboratory one represents a drainage process from the saturated condition. Hence, the slight difference in the critical rainfall indicates the larger requirement of rainfall for slope instability from a drier condition.

The critical rainfall intensity I is a power-law function of rainfall duration D :

$$I = 176.7D^{-0.91} \quad (\text{for the sandstone}), \quad (7)$$

$$I = 127.7D^{-0.89} \quad (\text{for the sandstone}), \quad (8)$$

$$I = 44.9D^{-0.70} \quad (\text{for the mudstone}). \quad (9)$$

Equations (7) and (8) correspond to the results from in-situ and laboratory parameters of soil-water characteristic curves, respectively. The form of these equations, the power-law correlation between intensity and duration of rainfall, accords with the previously reported landslide-triggering thresholds (Caine, 1980; Cannon and Ellen, 1985; Wieczorek, 1987; Terlien, 1998; Jakob and Weatherly, 2003).

The rainfall thresholds in this study can be verified from the records of torrential rainfall on August 1, 1989, which caused landslides on the observed slopes. The four bold lines in Fig. 30 represent the records of the 1989 storm. These lines were calculated from the cumulative rainfall divided by hours of elapsed time from the onset of the main storm (Fig. 5). The mean rainfall intensities at the four sites exceed the analytical thresholds (Fig. 30). This coincides with the fact that both of the sandstone and mudstone slopes failed during the 1989 storm, validating the rainfall threshold for landsliding on each slope.

Moreover, the larger critical rainfall in the sandstone slope predicts delayed occurrence of shallow landslides compared to the one on the mudstone slopes (Fig. 30). The intersections of the rainfall thresholds for each hillslope and the temporal progress in mean rainfall intensity disagrees with their timings from the storm onset. The rainfall records of the 1989 storm first reach the mudstone threshold, and then attain the sandstone thresholds with a delay of several to dozens of hours (Fig. 30). Equations (7)–(9) may make it possible to establish a practical criterion for landslide warnings at

different timings in various rainfall situations. Unfortunately, no record of actual landslide timings is available during the 1989 storm. The verification of this prediction is left to future works which prove the time-lags of the landslides within a prolonged storm event.

VI-2-4 Recurrence intervals of the critical rainfall

Rainfall records from 1940 to 2004 at Yokohama meteorological station provide standard intensity–duration–frequency curves of rainfall (solid lines in Fig. 31). These curves were calculated from the probable rainfall-intensity formula by the specific coefficient method for annual maximum records of 1-h and 24-h rainfall (Iwai and Ishiguro, 1970, pp. 162–177). This method is a statistical processing for estimating non-exceedance probability of mean rainfall intensity during an arbitrary time-frame of rainfall. Thus the curves indicate equipotential lines of probabilities (i.e., return periods) for varying combinations of rainfall intensity and duration.

By combining with the return periods of rainfall, one can translate the critical intensity–duration relationship to a recurrence interval of the landslide-triggering rainfall. This refinement derives a minimum recurrence interval of landslide events, based upon an implicit assumption of optimal material conditions for failure at all time. The recurrence interval of the critical rainfall ranges 3–200 years for the sandstone slope (incorporating the error bars), whereas it is 1.1–3 years for the mudstone slope (Fig. 31). The discrete recurrence intervals of the critical rainfall implies that the landslide probability varies from several to dozens of times during a given time period.

Of note is that the sandstone slope requires higher rainfall intensity and greater rainfall duration, and thus longer recurrence intervals than the mudstone slope (Fig. 31).

This implies the lower potential for landsliding in the sandstone slope, corresponding to the lower landslide activity (Fig. 7). Smaller landslide frequency is responsible for the preservation of thick and hardly saturated soil layers on the hillslope as stated by Onda (1992). This negative feedback system between the soil development and the soil removal by landsliding may exist on the sandstone hillslope.

VI-3 Summary of discussion, advantages and future prospects

Figure 32 summarizes the hydrological triggering systems of the shallow landslides in the studied hills. Weathering of bedrock under a certain climate condition provides soils on hillslopes with site-specific physical properties, especially in shear strength and soil-water retention characteristics. They affect mechanical stability limit of the hillslopes. Permeability of the bedrock controls the hydrological processes in the hillslopes and mechanisms of shallow landslide initiation.

Permeable bedrocks produce a deep and stable groundwater system across an entire hillslope. Rainwater supplied to the slope seeps vertically through the near-surface zone. The downward migration of the wetting front reduces soil cohesion, and results in a shallow landslide under an unsaturated regime. Rain in excess of the threshold for this type of landsliding falls over several hours to a few days, with a return period in decadal scale.

Hillslopes with impervious bedrocks produce a shallow transient drainage system in soils upon the bedrock. The relatively permeable soil layer drains incoming rainwater out to slopes under saturated conditions. The shallow groundwater table builds up and dissipates transiently, generating positive pressure head in the soil mass. The resultant decrease in effective stress at the soil bottom triggers a slide of the soil layer. The

instantaneous rainfall with durations from several hours to half a day triggers a landslide, which occurs within a short recurrence interval up to three years.

The rainfall thresholds in the present study incorporate the site-specific factors, such as strength of slope materials or slope hydrological processes. These factors were ignored or poorly taken into account in a traditional approach that differentiated the landslide-triggering storms from non-landslide rainfall events (Cannon and Ellen, 1985; Keefer et al, 1987; Wiczorek, 1987; Jakob and Weatherly, 2003). The analytical procedure for determining the site-specific threshold is applicable to any regions where geotechnical soil properties and a certain amount of hydrological data are available. Residents living in a vicinity of hazardous areas may be able to evacuate following the warnings based on the site-specific critical combination of rainfall intensity and duration.

Although the rainfall in excess of the threshold is a necessary, but it is not a sufficient condition for landslide occurrence. Landslides would not occur under an inadequate soil thickness. Soil depths on hillslopes changes both temporally and spatially as the past scars with different ages recover sequentially with soil accumulation and bedrock weathering (Shimokawa 1984; Trustrum and De Rose, 1988). Thus the spatial and temporal distribution of landslide is influenced strongly by the historical sequence of landsliding (Iida, 2004). Quantitative evaluation of the actual landslide frequencies requires a more integrated approach incorporating a numerical modeling of subsurface water behavior, topographic effect of slope instability, and basin wide distribution of soil thickness and its alteration in a long time-scale.

Chapter VII Conclusions

This study has focused on landslide mechanisms and rainfall threshold on hillslopes underlain by permeable sandstone and impermeable mudstone in the Boso Peninsula, central Japan. Pressure head monitoring revealed contrasting hydrological processes in hillslopes, and a slope stability analysis including strength reduction of the slope material specified the critical pressure heads for landslide initiation. An analysis of relationship between the magnitude of rainfall and hillslope instability provides critical combinations of rainfall intensity and duration. Hillslopes with different geological settings are denudated by dissimilar landslides in their mechanisms and rainfall thresholds.

In hillslopes with permeable sandstone, subsurface pressure head at the deepest monitoring depth did not exceed 0 m in response to rainfall. Infiltrated rainwater percolates through the bedrock as an unsaturated gravitational flow, giving a constant base flow from the watershed. Critical pressure head for landslide initiation were calculated to be $-0.1-0$ m, suggesting that the reduction in soil cohesion by wetting-front migration causes a landslide. This type of landslide occurs entirely on a steep lower part of the hillslopes ($> \sim 30^\circ$) where the slope angles are larger than the angle of shearing resistance of the soil. Rainfall during three days destabilizes the sandstone hillslope most effectively, suggesting the significance of ancient soil moisture for the initiation of the unsaturated landslide.

The pressure heads at a soil–bedrock boundary in hillslope with impermeable mudstone reaches positive values of ~ 0.5 m in response to almost all rainfall. A saturated subsurface storm flow drains the infiltrated rainwater and produces the acute

runoff responses from the watershed. Critical pressure head for landslide initiation were calculated to be 0.7–0.8 m. In addition to a reduction in soil cohesion, a decrease in effective stress causes a landslide under a saturated regime. The relatively shorter rainfall with durations from several hours to half a day is crucial for this type of landslide initiation. This indicates that an intense and instantaneous rainfall contributes to triggering shallow landslides.

Rainfall intensity for landslide initiation is represented as a power-law function of rainfall duration. The critical combination of rainfall intensity and duration for the permeable sandstone slope recurs with a decadal return period (3–200 years), whereas the impermeable mudstone slope has a threshold with a yearly recurrence interval (1.1–3 years). The rainfall thresholds incorporate geotechnical soil properties and slope hydrological processes in each hillslope. The longer return period of the threshold implies the lower potential for landsliding, which corresponds to the lower landslide activity in the hillslopes with permeable bedrocks.

Acknowledgements

I wish to appreciate Professor Dr. Yukinori Matsukura (University of Tsukuba) for his valuable suggestions, guidance, and encouragement. Constructive comments by Professor Dr. Norikazu Matsuoka (University of Tsukuba) benefited logical organization of this study. I thank Professor Dr. Norikazu Matsuoka again for lending the geo-electric apparatus for the subsurface resistivity inspections. The script of this thesis was greatly improved with critical readings by Professor Dr. Norikazu Matsuoka, Professor Dr. Tadashi Tanaka (University of Tsukuba), and Assistant Professor Dr. Tomohiro Sekiguchi (University of Tsukuba). Professor Dr. Tadashi Tanaka lent me generously the weirs and the rain gauge for field observations. Technical supports by Dr. Tsuyoshi Hattanji (University of Tsukuba) permitted performance of the continuous hydrological measurements. I thank also Mr. Tetsuya Kogure for his assists in tensiometer settings and seismic soundings. My colleagues Mr. Tatsuya Watanabe, Ms. Yasuko Fukai, Mr. Shouhei Kizaki, and Ms. Marie Yamamoto supported field work for the electrical resistivity measurements. Discussions in regular seminars with members of the geomorphology research group of the University of Tsukuba helped motivate this work.

References

- Aniya, M., 1985. Contemporary erosion rate by landsliding in Amahata River basin, Japan. *Zeitschrift für Geomorphologie Neue Folge* 39, 301–314.
- Borga, M., Fontana, G.D., Gregoretti, C., Marchi, L., 2002. Assessment of shallow landsliding by using a physically based model of hillslope stability. *Hydrological Processes* 16, 2833–2851.
- Caine, N., 1980. The rainfall intensity–duration control of shallow landslides and debris flows. *Geografiska Annaler* 62A, 23–27.
- Cannon, S.H., Ellen, S., 1985. Rainfall conditions for abundant debris avalanches, San Francisco Bay region, California. *California Geology* 38, 267–272.
- Carson, M.A., 1971. An application of the concept of threshold slopes to the Laramie Mountains, Wyoming. In: Brunsdon, D., (Eds.), *Slopes Form and Process. Institute of British Geographers, Special Publication* 3, 31–48.
- Carson, M.A., Petley, D.J., 1970. The existence of threshold hillslopes in the denudation of landscape. *Institute of British Geographers Transactions* 49, 71–95.
- Cho, S.E., Lee, S.R., 2001. Instability of unsaturated soil slopes due to infiltration. *Computers and Geotechnics* 28, 185–208.
- Collins, B.D., Znidarcic, D., 2004. Stability analyses of rainfall induced landslides. *Journal of Geotechnical and Geoenvironmental Engineering* 130, 362–372.
- Dietrich, W.E., Dunne, T., 1978. Sediment budget for a small catchment in mountainous terrain. *Zeitschrift für Geomorphologie Neue Folge Supplementbände* 29, 191–206.

- D'Odorico, P., Fagherazzi, S., Rigon, R., 2005. Potential for landsliding: Dependence on hyetograph characteristics. *Journal of Geophysical Research* 110, F01007, doi: 10.1029/2004JF000127.
- Dykes, A.P., 2002. Weathering-limited rainfall-triggered shallow mass movements in undisturbed stepland tropical rainforest. *Geomorphology* 46, 73–93.
- Escario, V., Sáez, J., 1986. The shear strength of partly saturated soils. *Géotechnique* 36, 453–456.
- Fannin, R.J., Jaakkola, J., 1999. Hydrological response of hillslope soils above a debris-slide headscarp. *Canadian Geotechnical Journal* 36, 1111–1122.
- Fannin, R.J., Jaakkola, J., Wilkinson, J.M.T., Hetherington, E.D., 2000. Hydrologic response of soils to precipitation at Carnation Creek, British Columbia, Canada. *Water Resources Research* 36, 1481–1494.
- Fredlund, D.G., Morgenstern, N.R., Widger, R.A., 1978. The shear strength of unsaturated soils. *Canadian Geotechnical Journal* 15, 313–321.
- Furuya, T., Ohkura, H., 1992. Some geological and geomorphological characteristics of the slope failures on the Mt. Kano-zan and its environs in the Boso Peninsula, Japan. *Journal of Japan Landslide Society* 28–4, 29–36 (in Japanese, with English abstract).
- Gan, J.K.M., Fredlund, D.G., Rahardjo, H., 1988. Determination of the shear strength parameters of an unsaturated soil using the direct shear test. *Canadian Geotechnical Journal* 25, 500–510.
- Gasmo, J.M., Rahardjo, H., Leong, E.C., 2000. Infiltration effects on stability of a residual soil slope. *Computers and Geotechnics* 26, 145–165.

- Iida, T., 1999. A stochastic hydro-geomorphological model for shallow landsliding due to rainstorm. *Catena* 34, 293–313.
- Iida, T., 2004. Theoretical research on the relationship between return period of rainfall and shallow landslides. *Hydrological Processes* 18, 739–756.
- Iida, T., Okunishi, K., 1979. On the slope development caused by the surface landslides. *Geographical Review of Japan* 52A, 426–438 (in Japanese, with English abstract).
- Iida, T., Okunishi, K., 1983. Development of hillslopes due to landslides. *Zeitschrift für Geomorphologie Neue Folge Supplementbände* 46, 67–77.
- Inoue, K., Oguchi, T., 1995. Effects of hillslope failure on stream bifurcation ratios and stream length ratios for the Matsumoto region, Japan. *Geographical Review of Japan* 68A, 447–464 (in Japanese, with English abstract).
- Ito, M., 1995. Volcanic ash layers facilitate high-resolution sequence stratigraphy at convergent plate margins: an example from the Plio–Pleistocene forearc basin fill in the Boso Peninsula, Japan. *Sedimentary Geology* 95, 187–206.
- Ito, M., 1998. Submarine fan sequences of the lower Kazusa Group, a Plio–Pleistocene forearc basin fill in the Boso Peninsula, Japan. *Sedimentary Geology* 122, 69–93.
- Ito, M., Horikawa, K., 2000. Millennial- to decadal-scale fluctuation in the paleo-Kuroshio Current documented in the Middle Pleistocene shelf succession on the Boso Peninsula, Japan. *Sedimentary Geology* 137, 1–8.
- Iverson, R.M., 2000. Landslide triggering by rain infiltration. *Water Resources Research* 36, 1897–1910.

- Iverson, R.M., Major, J.J., 1986. Groundwater seepage vectors and the potential for hillslope failure and debris flow mobilization. *Water Resources Research* 22, 1543–1548.
- Iwai, S., Ishiguro, M., 1970. *Applied Hydrological Statistics*. Morikita Shuppan, Tokyo, 370 p (in Japanese).
- Jakob, M., Weatherly, H., 2003. A hydroclimatic threshold for landslide initiation on the North Shore Mountains of Vancouver, British Columbia. *Geomorphology* 54, 137–156.
- Johnson, K.A., Sitar, N., 1990. Hydrologic conditions leading to debris-flow initiation. *Canadian Geotechnical Journal* 27, 789–801.
- Kaizuka, S., Koike, K., Endo, K., Yamazaki, H., Suzuki, T., 2000. *Regional Geomorphology of the Japanese Islands Vol. 4: Geomorphology of Kanto and Izu-Ogasawara*. University of Tokyo Press, Tokyo (in Japanese).
- Kamai, T., 1989. Slope failures by the 1987 Chibaken-toho-oki Earthquake in the Kazusa-Hills, Boso Peninsula, Central Japan —Classification of failures and slope stability. *Journal of Japan Landslide Society* 26–1, 16–25 (in Japanese with English abstract).
- Kamai, T., Noro, H., 1988. Slope failures in Kazusa-Hills during the 1987 Chibaken-Touhouoki Earthquake —Distribution and shape of failures. *Journal of the Japan Society of Engineering Geology* 29–4, 1–10 (in Japanese with English abstract).
- Keefer, D.K., Wilson, R.C., Mark, R.K., Brabb, E.E., Brown, W.M., Ellen, S.D., Harp, E.L., Wiczorek, G.F., Alger, C.S., Zatkan, R.S., 1987. Real-time landslide warning during heavy rainfall. *Science* 238, 921–925.

- Kim, J., Jeong, S., Park, S., Sharma, J., 2004. Influence of rainfall-induced wetting on the stability of slopes in weathered soils. *Engineering Geology* 75, 251–262.
- Kosugi, K., 1994. Three-parameter lognormal distribution model for soil water retention. *Water Resources Research* 30, 891–901.
- Krahn, J., Fredlund, D.G., Klassen, M.J., 1989. Effect of soil suction on slope stability at Notch Hill. *Canadian Geotechnical Journal* 26, 269–278.
- Lee, S.J., Lee, S.R., Kim, Y.S., 2003. An approach to estimate unsaturated shear strength using artificial neural network and hyperbolic formulation. *Computers and Geotechnics* 30, 489–503.
- Marquardt, D.W., 1963. An algorithm for least-squares estimation of non-linear parameters. *Journal of the Society for Industrial and Applied Mathematics* 11, 431–441.
- Matsukura, Y., 1984. Soil slips of two grass-slopes in Mino-mikawa Mountains, Central Japan. *Annual Report of the Institute of Geoscience, the University of Tsukuba* 10, 59–62.
- Matsukura, Y., Tanaka, Y., 1983. Stability analysis for soil slips of two grass-slopes in southern Abukuma Mountains, Japan. *Transactions, Japanese Geomorphological Union* 4, 229–139.
- Matsushi, Y., Matsukura, Y., 2004. Mechanism and location of slope failures in hilly terrains with different bedrock permeability. *Transactions, Japanese Geomorphological Union* 25, 139–159 (in Japanese, with English abstract).
- Miao, L., Liu, S., Lai, Y., 2002. Research of soil-water characteristics and shear strength features of Nanyang expansive soil. *Engineering Geology* 65, 261–267.

- Mino, Y., 1942. *Basis Theories of Geomorphology*. Kokon-Shoin, Tokyo, 517 pp (in Japanese).
- Montgomery, D.R., Dietrich, W.E., 1988. Where do channels begin? *Nature* 336, 232–234.
- Montgomery, D.R., Dietrich, W.E., 1989. Source areas, drainage density, and channel initiation. *Water Resources Research* 25, 1907–1918.
- Montgomery, D.R., Dietrich, W.E., 1992. Channel initiation and the problem of landscape scale. *Science* 255, 826–830.
- Montgomery, D.R., Dietrich, W.E., 1994. A physically based model for the topographic control on shallow landsliding. *Water Resources Research* 30, 1153–1171.
- Mualem, Y., 1976. A new model for predicting the hydraulic conductivity of unsaturated porous media. *Water Resources Research* 12, 513–522.
- Musiak, K., Oka, Y., Koike, M., 1988. Unsaturated zone soil moisture behavior under temperate humid climatic conditions —Tensiometric observations and numerical simulations. *Journal of Hydrology* 102, 179–200.
- Nakagawa, H., 1960. On the cuesta topography of the Boso peninsula, Chiba prefecture, Japan. *Science reports of the Tohoku University, Second Series, Geology, Special Volume* 4, 385–391.
- Numamoto, S., 1999. Monitoring of revegetation after slope failure using aerial photography —A 25-year trend in slope failure sites created by the southern Bousou storm in 1970. *Journal of Japan Society of Erosion Control Engineering* 223, 14–20 (in Japanese with English abstract).
- Oguchi, T., 1997. Drainage density and relative relief in humid steep mountains with frequent slope failure. *Earth Surface Processes and Landforms* 22, 107–120.

- Okimura, T., Ichikawa, R., 1985. A prediction method for surface failures by movements of infiltrated water in a surface soil layer. *Natural Disaster Science* 7, 41–51.
- Onda, Y., 1992. Influence of water storage capacity in the regolith zone on hydrological characteristics, slope processes, and slope form. *Zeitschrift für Geomorphologie Neue Folge* 36, 165–178.
- Onda, Y., 1994. Contrasting hydrological characteristics, slope processes and topography underlain by Paleozoic sedimentary rocks and granite. *Transactions, Japanese Geomorphological Union* 15, 49–65.
- Onda, Y., Tsujimura, M., Tabuchi, H., 2004. The role of subsurface water flow paths on hillslope hydrological processes, landslides and landform development in steep mountains of Japan. *Hydrological Processes* 18, 637–650.
- Pierson, T.C., 1983. Soil pipes and slope stability. *Quarterly Journal of Engineering Geology* 16, 1–11.
- Prior, D.B., Graham, J., 1974. Landslides in the Magho district of Fermanagh Northern Ireland. *Engineering Geology* 8, 341–359.
- Rahardjo, H., Lim, T.T., Chang, M.F., Fredlund, D.G., 1995. Shear-strength characteristics of a residual soil. *Canadian Geotechnical Journal* 32, 60–77.
- Rao, S.M., 1996. Role of apparent cohesion in the stability of Dominican allophane soil slopes. *Engineering Geology* 43, 265–279.
- Reneau, S.L., Dietrich, W.E., 1987. The importance of hollows in debris flow studies; examples from Marin County, California. In: Costa, J.E., Wieczorek, G.F. (Eds.), *Debris flows/avalanches: process, recognition, and mitigation*. Geological Society of America, *Reviews in Engineering Geology* VII, 165–180.

- Reneau, S.L., Dietrich, W.E., Donahue, D.J., Jull, A.J.T., Rubin, M., 1990. Late Quaternary history of colluvial deposition and erosion in hollows, central California Coast Ranges. *Geological Society of America Bulletin* 102, 969–982.
- Reneau, S.L., Dietrich, W.E., Rubin, M., Donahue, D.J., Jull, A.J.T., 1989. Analysis of hillslope erosion rates using dated colluvial deposits. *Journal of Geology* 97, 45–63.
- Rogers, N.W., Selby, M.J., 1980. Mechanisms of shallow translational landsliding during summer rainstorms: North Island, New Zealand. *Geografiska Annaler* 62A, 11–21.
- Sasaki, Y., Fujii, A., Asai, K., 2000. Soil creep process and its role in debris slide generation —field measurements on the north side of Tsukuba Mountain in Japan. *Engineering Geology* 56, 163–183.
- Selby, M.J., 1993. *Hillslope Materials and Processes, Second Edition*. Oxford University Press, Oxford.
- Shimokawa, E., 1984. A natural recovery process of vegetation on landslide scars and landslide periodicity in forested drainage basins. *Proceedings of the Symposium on Effects of Forest Land Use on Erosion and Slope Stability, Hawaii*, 99–107.
- Simoni, A., Berti, M., Generali, M., Elmi, C., Ghirotti, M., 2004. Preliminary result from pore pressure monitoring on an unstable clay slope. *Engineering Geology* 73, 117–128.
- Skempton, A.W., DeLory, F.A., 1957. *Proceedings of Fourth International Conference on Soil Mechanics and Foundation Engineering, London 2*, 378–381.

- Suzuki, T., Tokunaga, E., Noda, H., Arakawa, H., 1985. Effects of rock strength and permeability on hill morphology. *Transactions, Japanese Geomorphological Union* 6, 101–130.
- Talling, P.J., Sowter, M.J., 1999. Drainage density on progressively tilted surfaces with different gradients, Wheeler Ridge, California. *Earth Surface Processes and Landforms* 24, 809–824.
- Taylor, J.R., 1997. *An introduction to error analysis: the study of uncertainties in physical measurements, Second edition*. University Science Books, Mill Valley, California, 328 p (translated to Japanese by Hayashi, S., Baba, R.).
- Terlien, M.T.J., 1997. Hydrological landslide triggering in ash-covered slopes of Manizales (Colombia). *Geomorphology* 20, 165–175.
- Terlien, M.T.J., 1998. The determination of statistical and deterministic hydrological landslide-triggering thresholds. *Environmental Geology* 35, 124–130.
- Terzaghi, K., 1962. Stability of steep slopes on hard unweathered rock. *Géotechnique* 12, 251–270.
- Trustrum, N.A., De Rose, R.C., 1988. Soil depth–age relationship of landslides on deforested hillslopes, Taranaki, New Zealand. *Geomorphology* 1, 143–160.
- Tsukamoto, Y., 1973. Study on the growth of stream channel (I) —Relationship between stream channel growth and landslides occurring during heavy storm. *Journal of Japan Society of Erosion Control Engineering* 87, 4–13 (in Japanese).
- Tsukamoto, Y., Ohta, T., Noguchi, H., 1982. Hydrological and geomorphological studies of debris slides on forested hillslopes in Japan. In: Walling, D.E. (Eds.), *Recent Development in the Explanation and Prediction of Erosion and Sediment Yield*. IAHS Publication 137, 89–98.

- Tucker, G.E., Bras, R.L., 1998. Hillslope processes, drainage density, and landscape morphology. *Water Resources Research* 34, 2751–2764.
- Uchida, T., Kosugi, K., Mizuyama, T., 2001. Effects of pipeflow on hydrological process and its relation to landslide: a review of pipeflow studies in forested headwater catchments. *Hydrological Processes* 15, 2151–2174.
- Vanapalli, S.K., Fredlund, D.G., Pufahl, D.E., Clifton, A.W., 1996. Model for the prediction of shear strength with respect to soil suction. *Canadian Geotechnical Journal* 33, 379–392.
- Van Asch, Th.W.J, Buma, J., Van Beek, L.P.H., 1999. A view on some hydrological triggering systems in landslides. *Geomorphology* 30, 25–32.
- Van Genuchten, M.Th., 1980. A closed-form equation for predicting the hydraulic conductivity of unsaturated soils. *Soil Science Society of America Journal* 44, 892–898.
- Wakatsuki, T., Tanaka, Y., Matsukura, Y., 2005. Soil slips on weathering-limited slopes underlain by coarse-grained granite or fine-grained gneiss near Seoul, Republic of Korea. *Catena* 60, 181–203.
- Waragai, T., Hirose, T., Matsukura, Y., 1993. Instability of a slope made of sandy deposits due to earthquake on the northern Kazusa Hills. *The Chiri Shiso, Annals of the Geographical Association of Nihon University* 35–1, 9–14 (in Japanese with English abstract).
- Wieczorek, G.F., 1987. Effect of rainfall intensity and duration on debris flows in central Santa Cruz Mountains, California. In: Costa, J.E., Wieczorek, G.F. (Eds.), *Debris flows/avalanches: process, recognition, and mitigation*. *Geological Society of America, Reviews in Engineering Geology* VII, 93–104.

- Wu, W., Sidle, R.C., 1995. A distributed slope stability model for steep forested basins. *Water Resources Research* 31, 2097–2110.
- Yamada, S., 1999. The role of soil creep and slope failure in the landscape evolution of a head water basin: field measurements in a zero order basin of northern Japan. *Geomorphology* 28, 329–344.
- Yasuhara, M., 1984. Watershed response to a storm rainfall. *Science Report of the Institute of Geoscience, the University of Tsukuba* 5A, 1–27.
- Yatsu, E., 1950. On relief energy of the Chichibu Mountains, Japan. *Transactions Otsuka Geographical Association* 6, 323–330 (in Japanese).

Table 1 Sequence of landslide occurrence from aerial photographs

Photo ID (year)	Scale	Period	Maximum daily rainfall (mm)**	Number of landslides***	
				<i>Sandstone</i>	<i>Mudstone</i>
Photo A (1981)	1:20 000	–1981*		5	81
Photo B (1984)	1:20 000	1981–1984	173 (22 Oct. 1981)	6	42
Photo C (1990)	1:25 000	1984–1990	323 (1 Aug. 1989)	24	209
Photo D (1995)	1:25 000	1990–1995	180 (27 Aug. 1993)	0	32
Photo E (2000)	1:40 000	1995–2000	283 (22 Sep. 1996)	1	11
Total				36	375

*The latest landslide event occurred on 1 Jul. 1970. Rain of 206 mm fell at Yokohama, 390 mm fell at Fudago in Tokyo University Forest 20 km east from the study area (Numamoto et al., 1999).

**Averages of the records at the four meteorological stations: Yokohama, Kisarazu, Sakuma and Sakahata. See Fig. 1 for the locations.

***Number of newly emerged scars in six basins with total area of 6.33 km² for the sandstone and 2.94 km² for the mudstone.

Table 2 Dimensions of the landslides

	Slope angle (degrees)	Slip depth* (m)	Sliding area (m ²)	Volume (m ³)
<i>Sandstone</i>				
S-1	38.4	1.6	620	990
S-2	37.1	1.7	570	980
S-3	38.4	1.4	230	330
<i>Mudstone</i>				
M-1	32.2	0.7	70	50
M-2	35.4	0.6	70	40
M-3	34.7	0.6	100	40

*Measured vertically from the original ground surface to the slip plane.

Table 3 Physical properties of the soils

Depth (cm)	Dry unit wt. (kN/m ³)	Porosity* (m ³ /m ³)	Grain-size distribution (%)		
			Clay	Silt	Sand
<i>Sandstone</i>					
10	9.8	0.63	3.5	14.6	81.9
30	12.1	0.54	6.2	19.5	74.2
45	12.8	0.52	–	–	–
60	13.3	0.50	3.7	8.0	88.3
75	13.7	0.48	–	–	–
90	13.7	0.48	8.4	7.9	83.6
120	12.9	0.51	7.1	6.5	86.4
150	13.3	0.50	4.7	4.3	91.0
<i>Avg.</i>	<i>12.7</i>	<i>0.52</i>	<i>5.6</i>	<i>10.1</i>	<i>84.3</i>
<i>Mudstone</i>					
5	9.4	0.64	–	–	–
10	–	–	17.1	51.2	31.7
15	11.4	0.56	–	–	–
30	10.5	0.60	19.3	46.0	34.6
40	11.7	0.56	–	–	–
60	–	–	6.8	42.6	50.6
70	12.5	0.52	–	–	–
90	–	–	6.3	34.9	58.8
<i>Avg.</i>	<i>11.1</i>	<i>0.58</i>	<i>12.4</i>	<i>43.7</i>	<i>43.9</i>

*Calculated from the specific gravity of the soil particle: 2.693 for the sandstone, and 2.676 for the mudstone.

Table 4 Optimum parameter values for the model fitted to soil-water retention characteristics

	Saturated v.w.c.* θ_s (m ³ /m ³)	Residual v.w.c.* θ_r (m ³ /m ³)	Inflection point ψ_0 (m)	Parameter m (-)	r^2
<i>Sandstone</i>					
Depth 30 cm	0.47	0.17	-18.9×10^{-2}	0.58	0.98
Depth 75 cm	0.47	0.16	-25.2×10^{-2}	0.60	0.95
<i>Mudstone</i>					
Depth 15 cm	0.53	0.35	-5.7×10^{-2}	0.47	0.95
Depth 30 cm	0.53	0.32	-0.1×10^{-2}	0.20	0.99

*v.w.c. = volumetric water content.

Table 5 Moisture contents and shear test results for each specimen group

<i>Sandstone</i>					
Group	Moisture condition	Volumetric water content (m ³ /m ³)	Degree of saturation (%)	Normal stress (kPa)	Shear strength (kPa)
A	Oven-dried (40 °C)	0.03	6.7	10	33.2
		0.03	4.8	20	40.5
		0.03	6.4	30	53.8
		0.07	12.4	40	65.6
B	Air-dried (25 °C)	0.11	19.6	10	32.5
		0.13	24.3	20	36.8
		0.10	20.0	30	40.6
C	Natural water content	0.09	18.8	40	50.5
		0.18	35.7	10	20.4
		0.16	31.6	20	26.2
		0.15	28.8	30	29.9
D	Add 6 ml water	0.14	25.2	40	40.1
		0.24	47.9	10	13.3
		0.25	49.4	20	20.0
		0.24	46.2	30	25.9
E	Add 13 ml water	0.24	45.4	40	32.3
		0.37	73.3	10	12.6
		0.36	69.5	20	15.1
		0.36	67.2	30	22.8
F	Capillary saturated	0.36	70.9	40	25.5
		0.40	79.2	10	11.3
		0.42	85.1	20	16.6
		0.43	85.0	30	21.2
		0.40	77.6	40	26.8
		0.44	83.6	10	8.9
		0.46	89.4	20	15.9
		0.41	80.6	30	20.2
		0.46	94.9	40	27.6

Table 5 Continued

<i>Mudstone</i>					
Group	Moisture condition	Volumetric water content (m ³ /m ³)	Degree of saturation (%)	Normal stress (kPa)	Shear strength (kPa)
G	Oven-dried (40 °C)	0.15	25.0	10	45.1
		0.06	9.9	20	75.0
		0.15	24.9	30	77.0
		0.18	28.3	40	88.3
H	Air-dried (25 °C)	0.28	45.8	10	32.1
		0.29	46.6	20	35.2
		0.29	48.8	30	41.2
I	Natural water content	0.28	46.8	40	66.0
		0.40	68.8	10	15.5
		0.37	66.3	20	22.6
		0.36	64.8	30	29.9
J	Add 5 ml water	0.37	66.3	40	32.5
		0.44	75.1	10	13.7
		0.45	77.4	20	19.3
		0.45	77.6	30	24.6
K	Add 10 ml water	0.43	73.6	40	29.5
		0.47	81.4	10	13.4
		0.48	84.0	20	17.8
		0.49	83.4	30	24.2
L	Capillary saturated	0.47	84.4	40	28.3
		0.53	94.9	10	10.9
		0.52	95.8	20	15.9
		0.53	92.7	30	20.2
		0.49	89.2	40	26.8

Table 6 Shear strength parameters obtained by a simple linear-regression for the dataset of each specimen group

<i>Sandstone</i>						
Group	Dry					Saturated
	A	B	C	D	E	F
Angle of shearing resistance (degrees)	48.4	30.5	32.6	32.7	25.3	29.6
Soil cohesion (kPa)	20.1	25.4	13.2	6.9	7.2	4.4

<i>Mudstone</i>						
Group	Dry					Saturated
	G	H	I	J	K	L
Angle of shearing resistance (degrees)	53.3	47.7	30.7	28.2	27.5	27.9
Soil cohesion (kPa)	37.8	16.2	10.3	8.4	7.9	5.2

Table 7 Optimum parameter values for the regressions for reduction in soil shear strength

	Soil cohesion at dry condition		Reduction coefficient μ (-)	Angle of shearing resistance ϕ (degrees)	r^2
	$\ln C$	C (kPa)*			
<i>Sandstone</i>	3.58	35.8	4.81	28.3	0.88
<i>Mudstone</i>	5.26	192.9	6.94	27.7	0.93

*Converted from the values of $\ln C$.

Table 8 Parameter values for envelopes of in situ soil-water retention plots

	Saturated v.w.c.* θ_s (m ³ /m ³)	Residual v.w.c.* θ_r (m ³ /m ³)	Inflection point ψ_0 (m)	Parameter m (-)
<i>Sandstone</i>	0.47	0.16	-10×10^{-2}	0.56
<i>Mudstone</i>	0.53	0.20	-5×10^{-2}	0.20

*v.w.c. = volumetric water content.

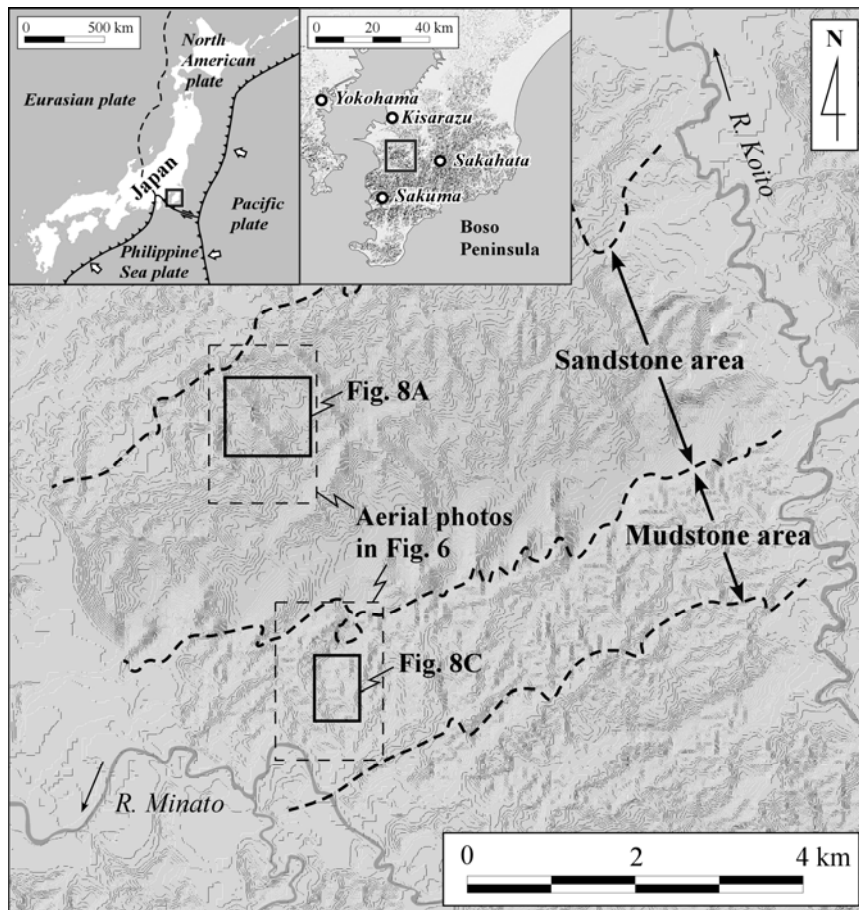


Figure 1 Location and shaded relief map of the study area

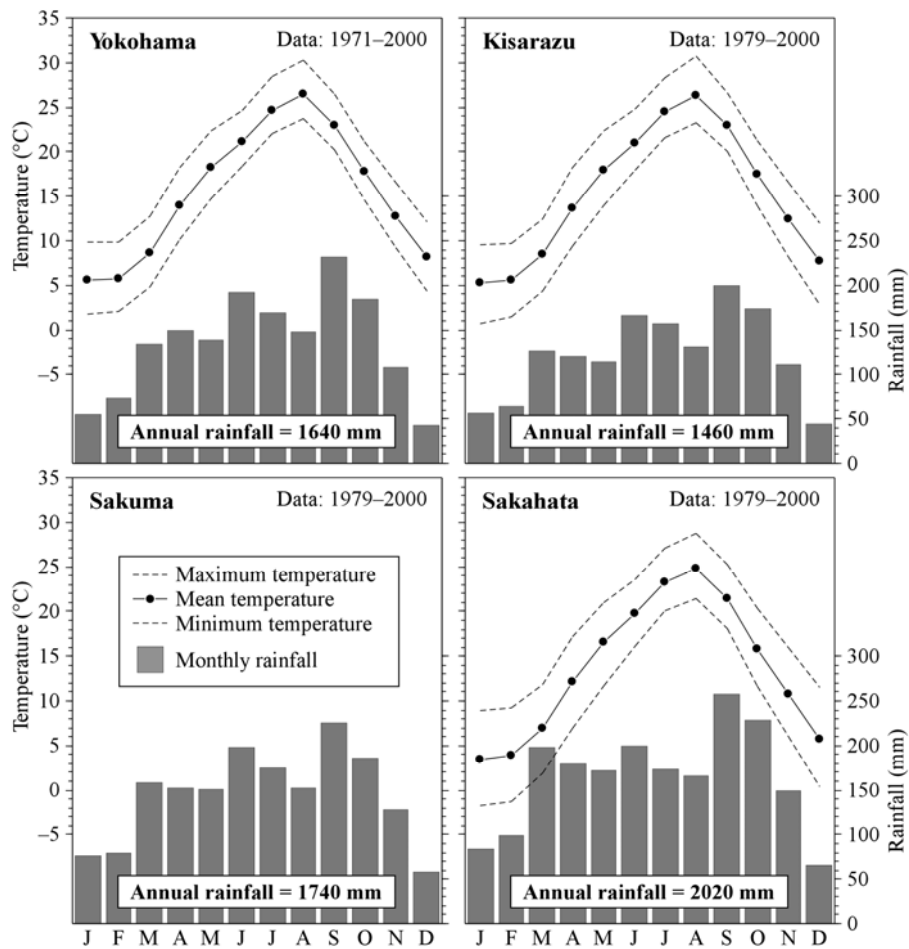


Figure 2 Climatic conditions of the study area

Locations of the meteorological stations are shown in Fig. 1. The station Sakuma has no data of temperature.

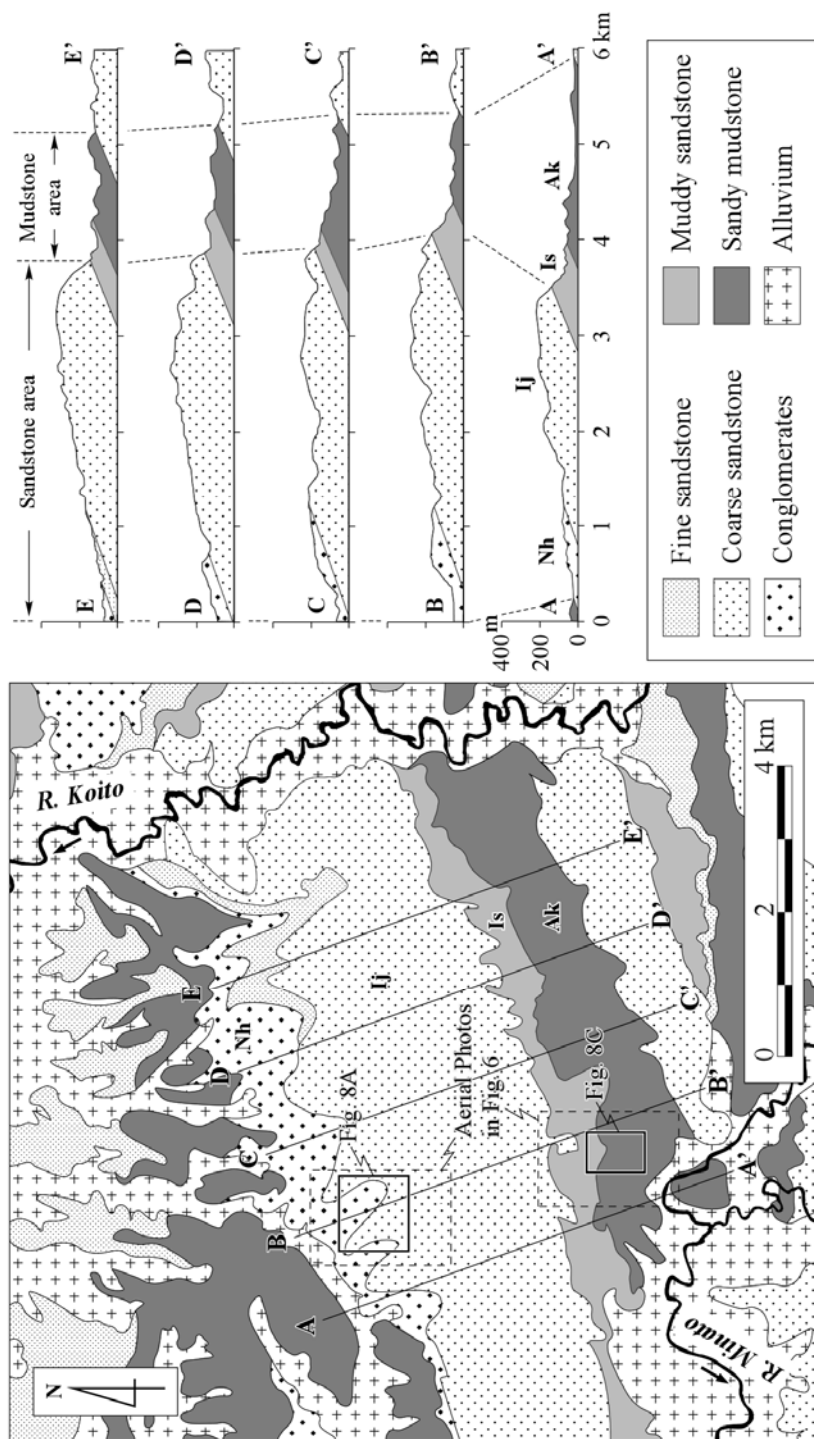


Figure 3 Geologic map and topographic cross-sections of the study area

Nh: Nagahama Formation; Ij: Ichijuku Formation; Is: Iwasaka Formation; Ak: Awakura Formation. The area of geological map corresponds to Fig. 1.

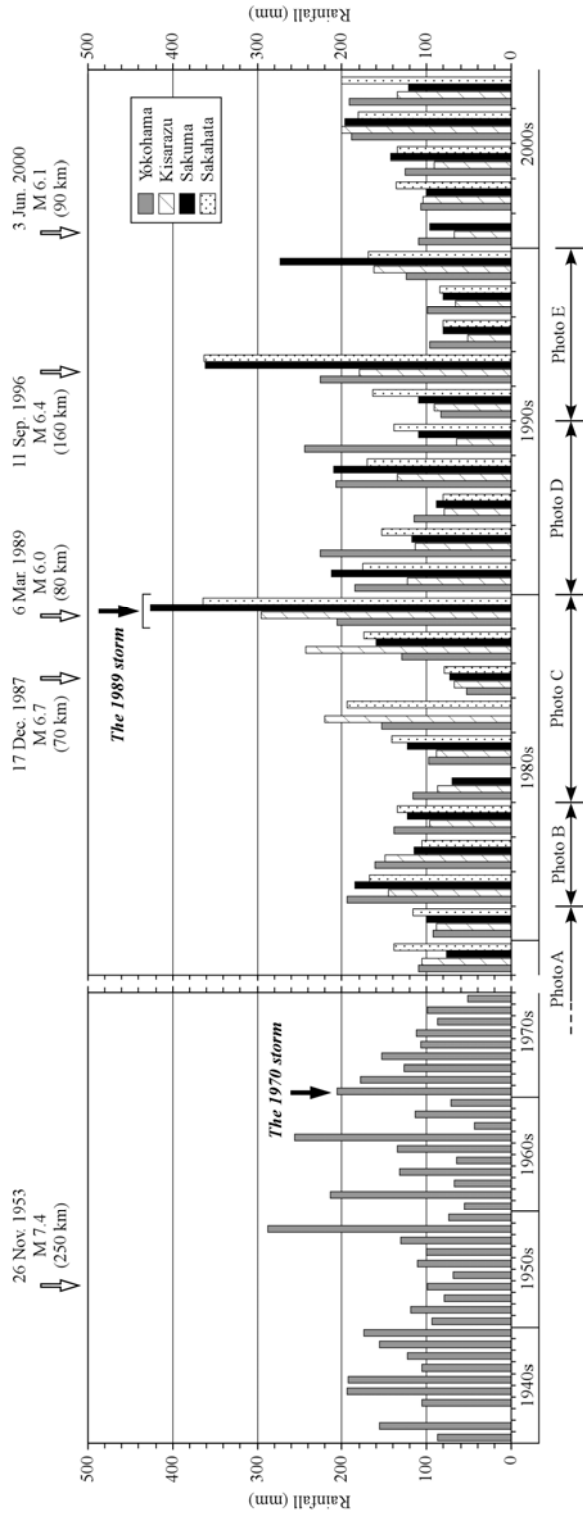


Figure 4 Records of annual maximum daily rainfall in the study area.

Data are available from only the Yokohama meteorological station during 1940–1978. Black arrows indicate the rainfall events triggering landslides. White arrows above the figure show the records of large earthquakes: date, magnitude on the Richter scale, and epicentral distance from the study area. Photo A to E represents the periods for counting number of landslides within the aerial photographs. See Fig. 1 for locations of the meteorological stations.

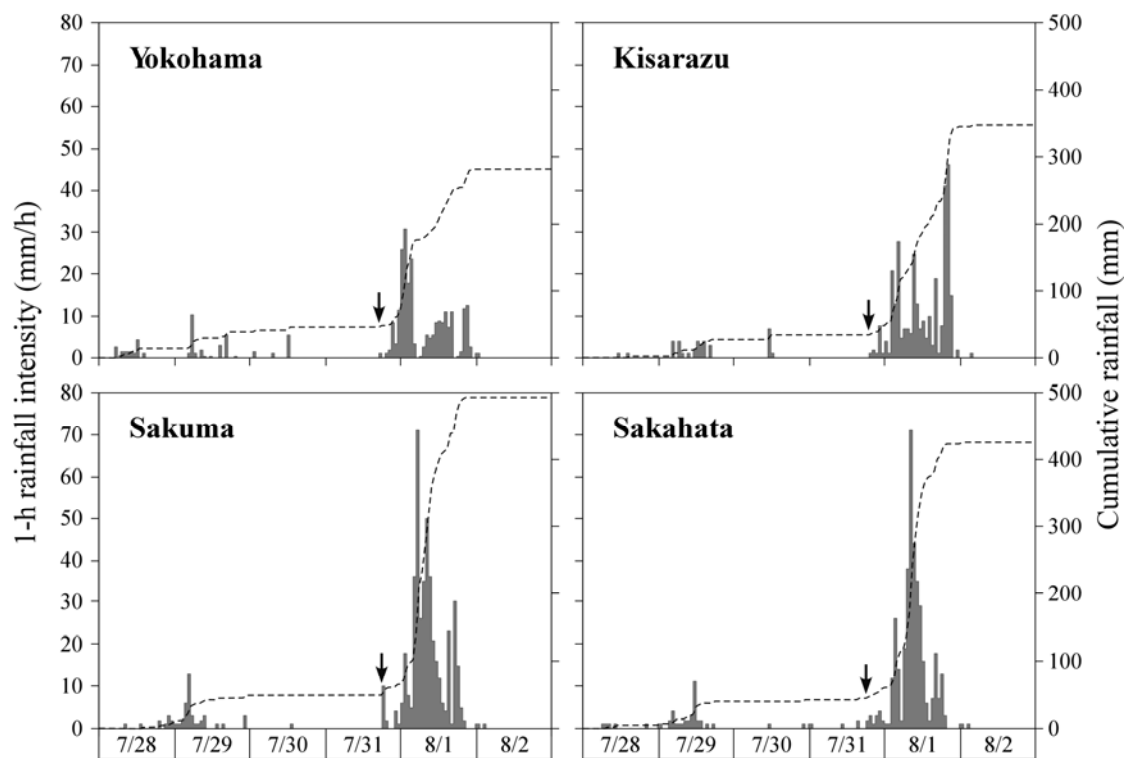


Figure 5 Rainfall records of the 1989 storm

Bars show rainfall intensity, broken curves represent cumulative rainfall amount. Arrows indicate the onset of the main storm body. See Fig. 1 for locations of the meteorological stations.

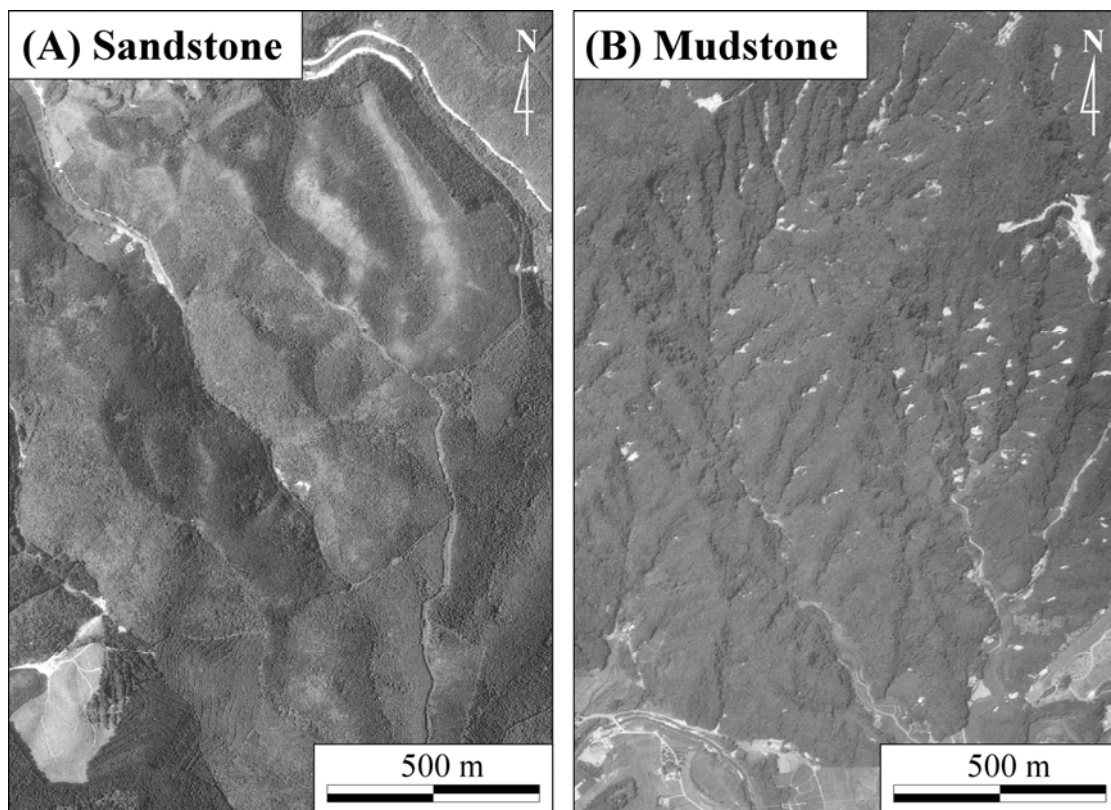


Figure 6 Aerial photographs taken in 1990

Scopes of the photographs are located in Figs. 1 and 3.

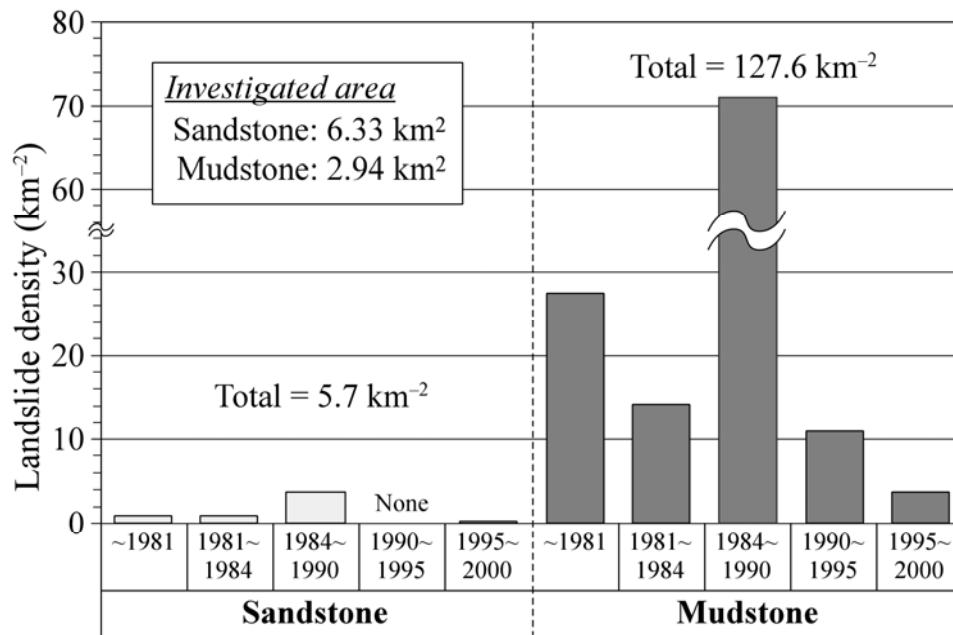


Figure 7 Landslide densities for the past two decades

Landslide densities were calculated from the number of slip scars on vertical air photographs taken in 1981, 1984, 1990, 1995 and 2000.

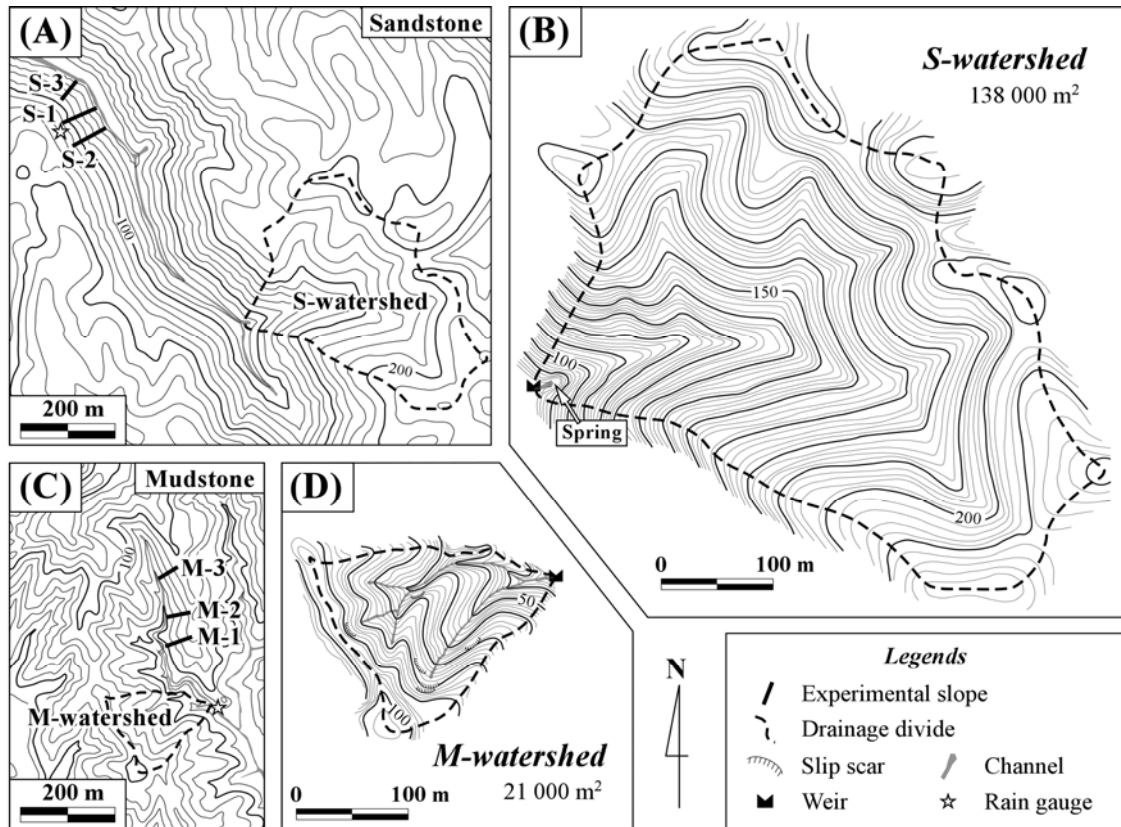


Figure 8 Locations of the selected slopes and topographic maps of the observed watersheds

See Figs. 1 and 3 for locations of the maps (A) and (C). Contours are in meters.

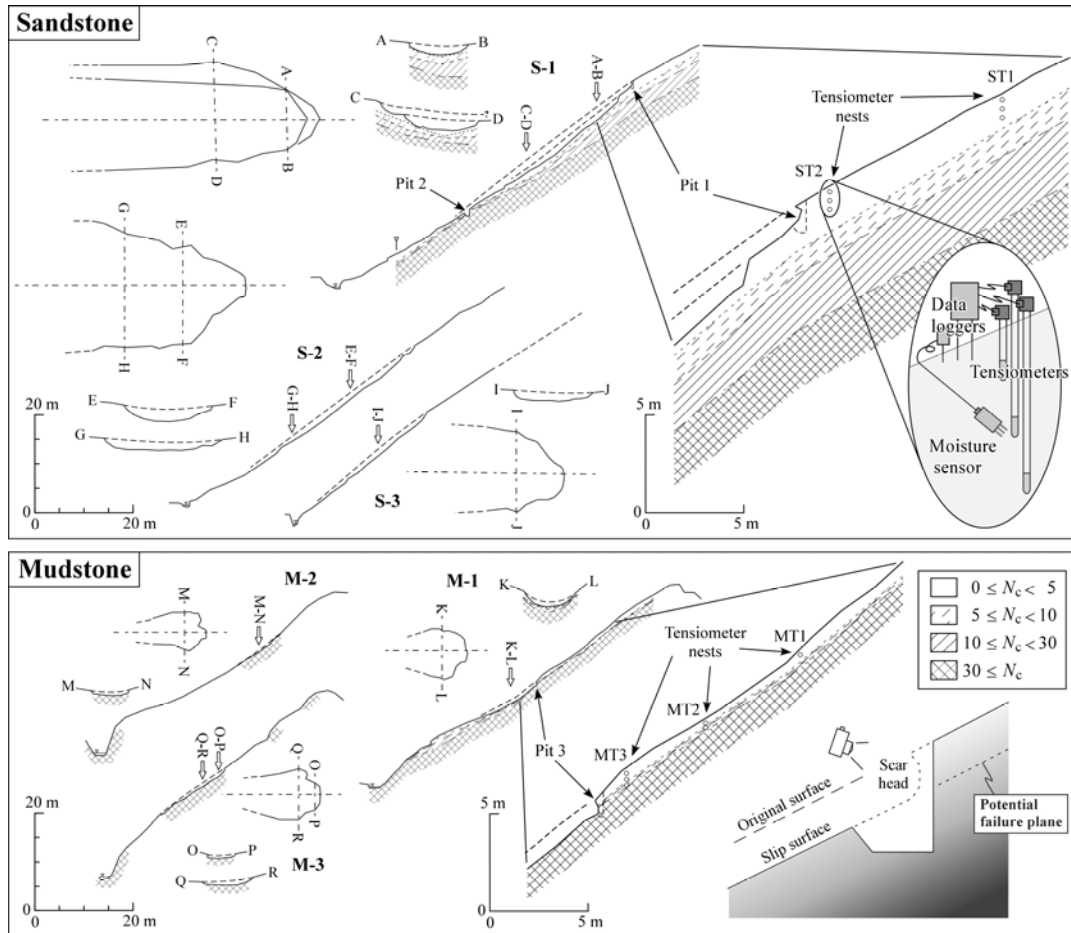


Figure 9 Profiles of the selected slopes, and plan views and cross sections of slip scars

The subsurface layers of S-1 and M-1 are inferred from soil soundings (see Fig. 10 for details). Enlarged views of the upper parts of the slopes show the sensor nests for hydrological observation. The schematic illustration in the lower right shows soil pit scraping at scar heads. See Figs. 8A and 8C for locations of the slopes.

(A)

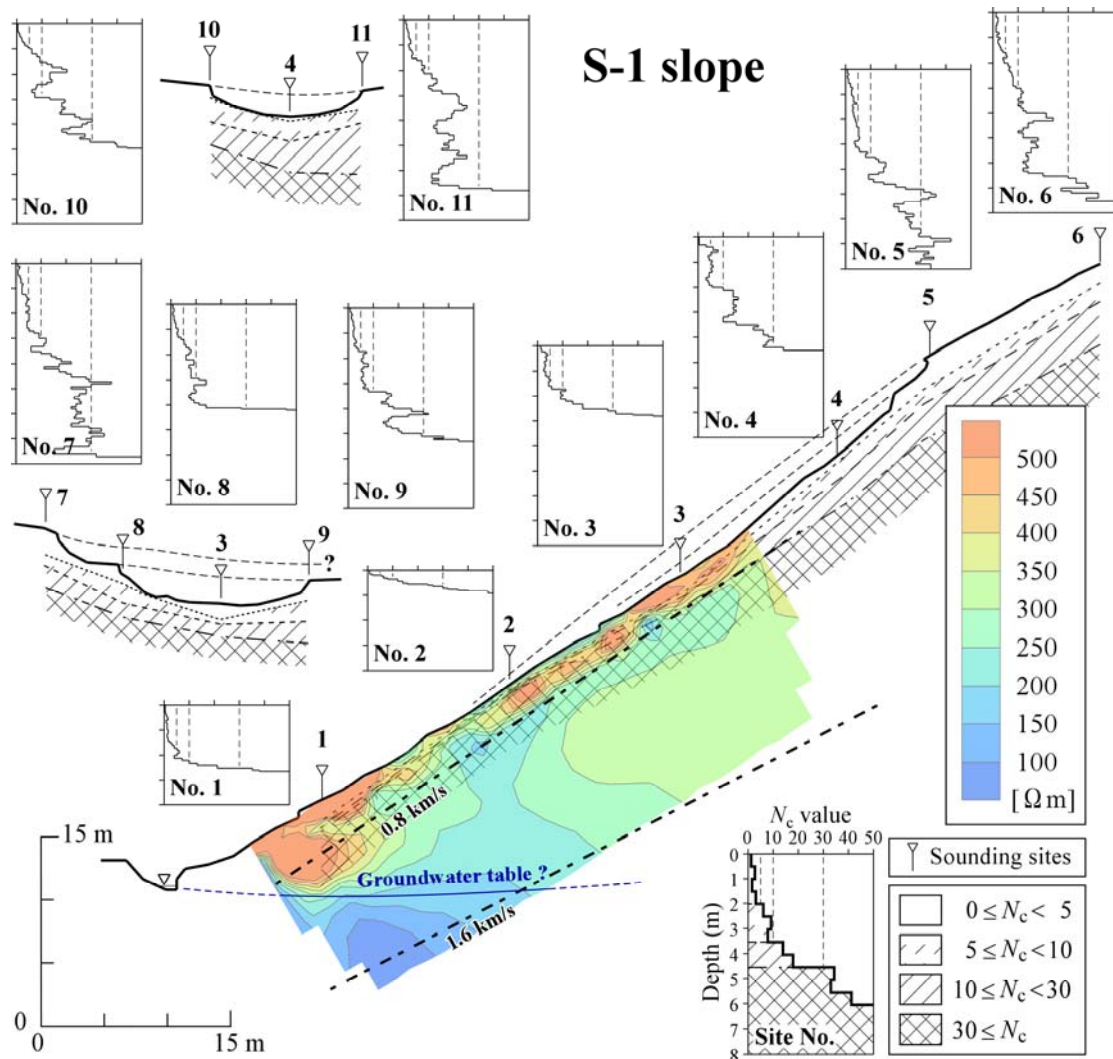


Figure 10 Subsurface structures of the hillslopes inferred from soil soundings and geophysical surveys

For the sandstone (A) and mudstone (B) slopes. Hatched layers represent soil classifications by cone penetration resistance. Dash-dotted bold lines indicate elastic discontinuities inferred from the seismic refraction soundings. Colored regions show resistivity tomograms obtained by electrical resistivity investigations.

(B)

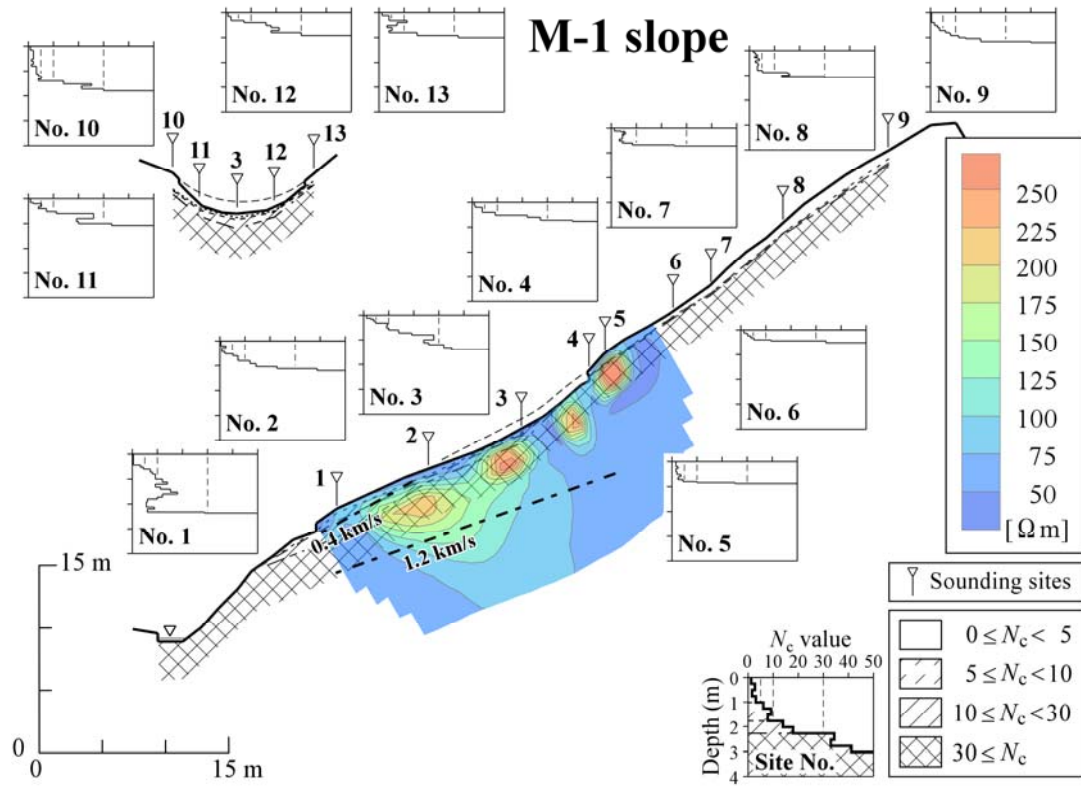


Figure 10 Continued

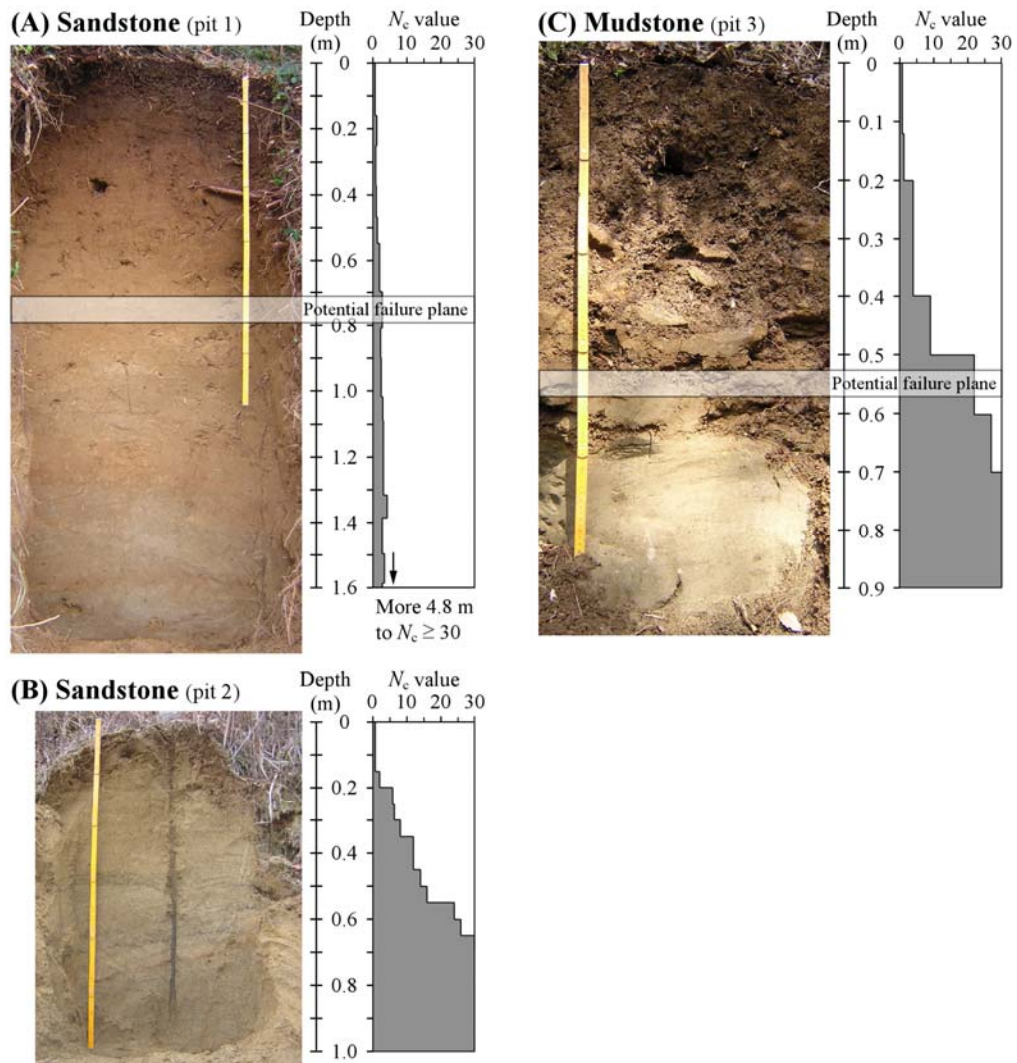


Figure 11 Shallow soil profiles at the soil pits with depth variations of the cone penetration resistance

See Fig. 9 for locations of the soil pits. Horizontal narrow bands represent the potential failure depth that corresponds to the height of scar step (cf. schematic in Fig. 9)

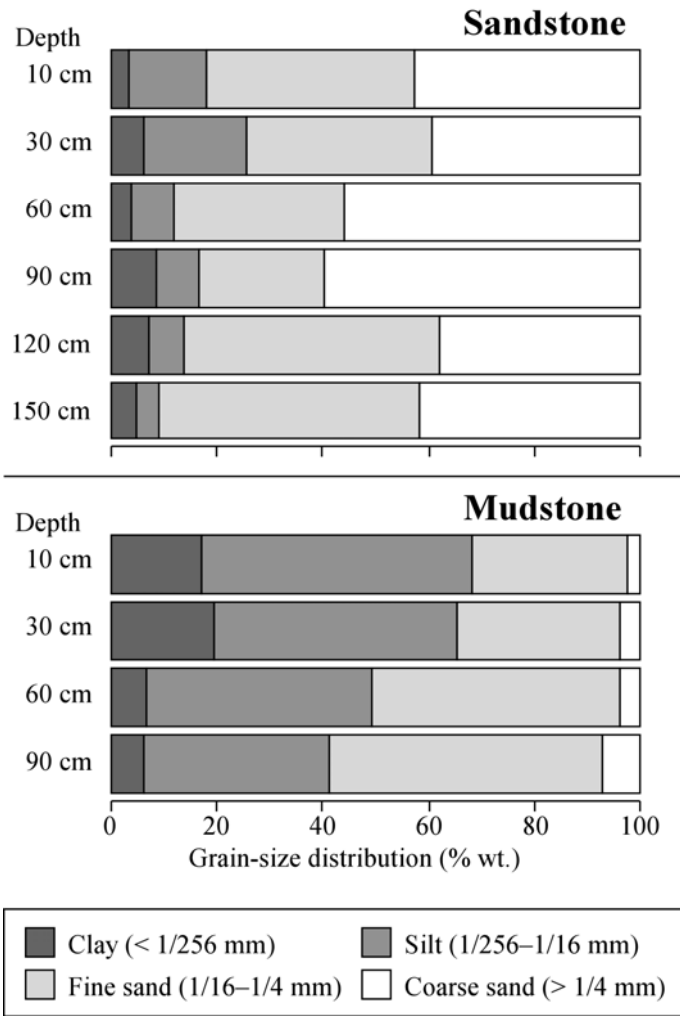


Figure 12 Grain-size distributions of the soils

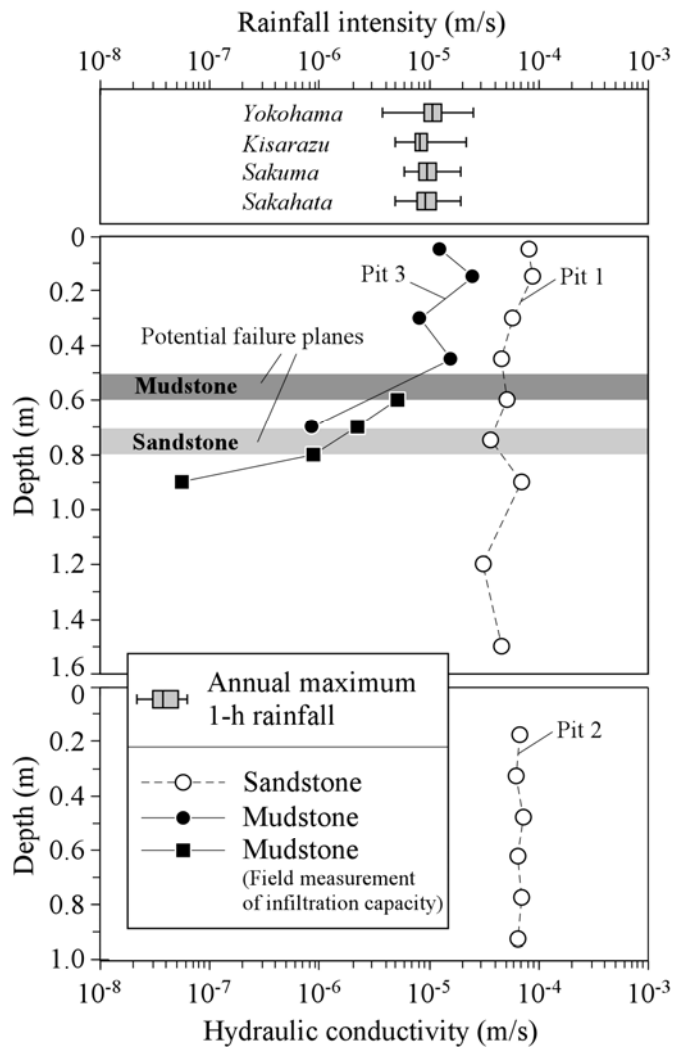


Figure 13 Vertical profiles of hydraulic conductivity

See Fig. 9 for locations of the soil pits. The open and solid circles represent saturated hydraulic conductivities measured at laboratory. The solid squares are the results of in situ infiltration tests under saturated conditions. Horizontal shaded bands indicate the depth of potential failure planes (cf. Fig. 11). Box-plots in the upper diagram represent the annual maximum 1-h rainfalls at the four meteorological stations (see Fig. 1 for their locations) Horizontal whiskers, shaded boxes, and vertical lines within the boxes represent the extremes, interquartile range, and median values, respectively.

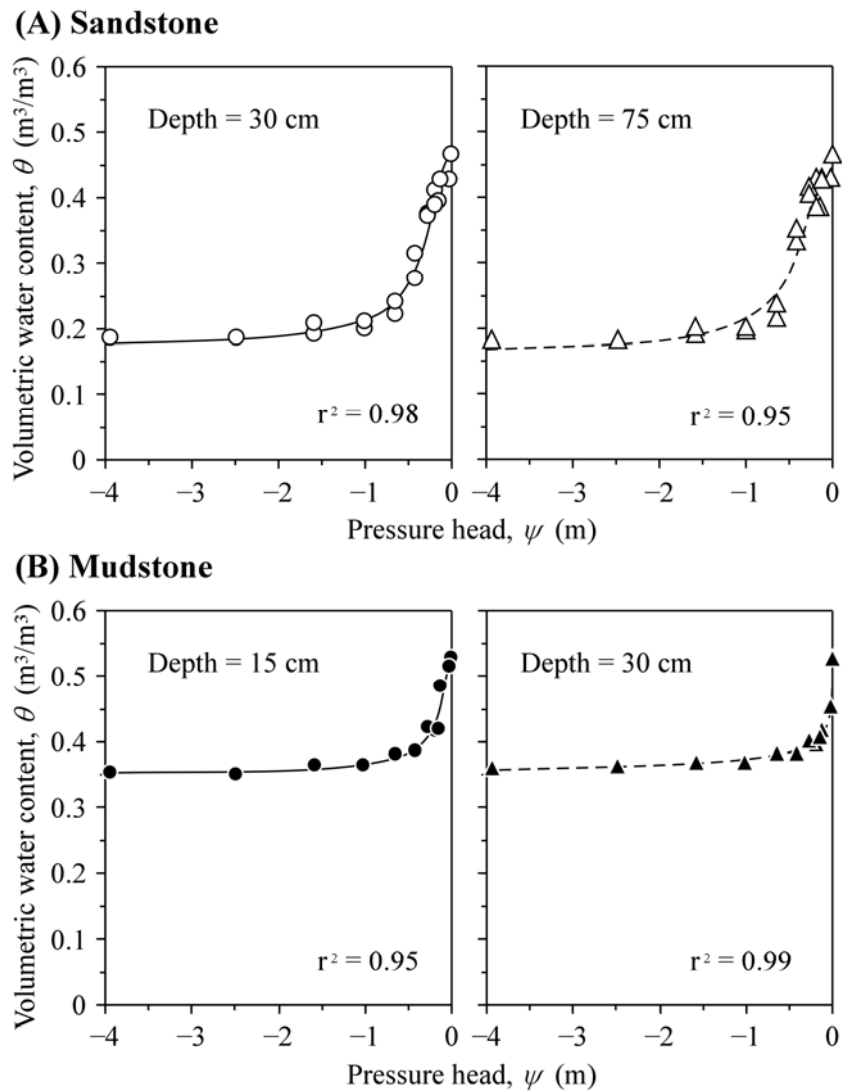


Figure 14 Soil-water characteristic curves of the soils

The plots represent drying soil-water retention from saturated conditions. The broken and solid lines are best-fit Kosugi's (1994) model curves (see Eq. (1) in text), whose optimum parameter values are listed in Table 4.

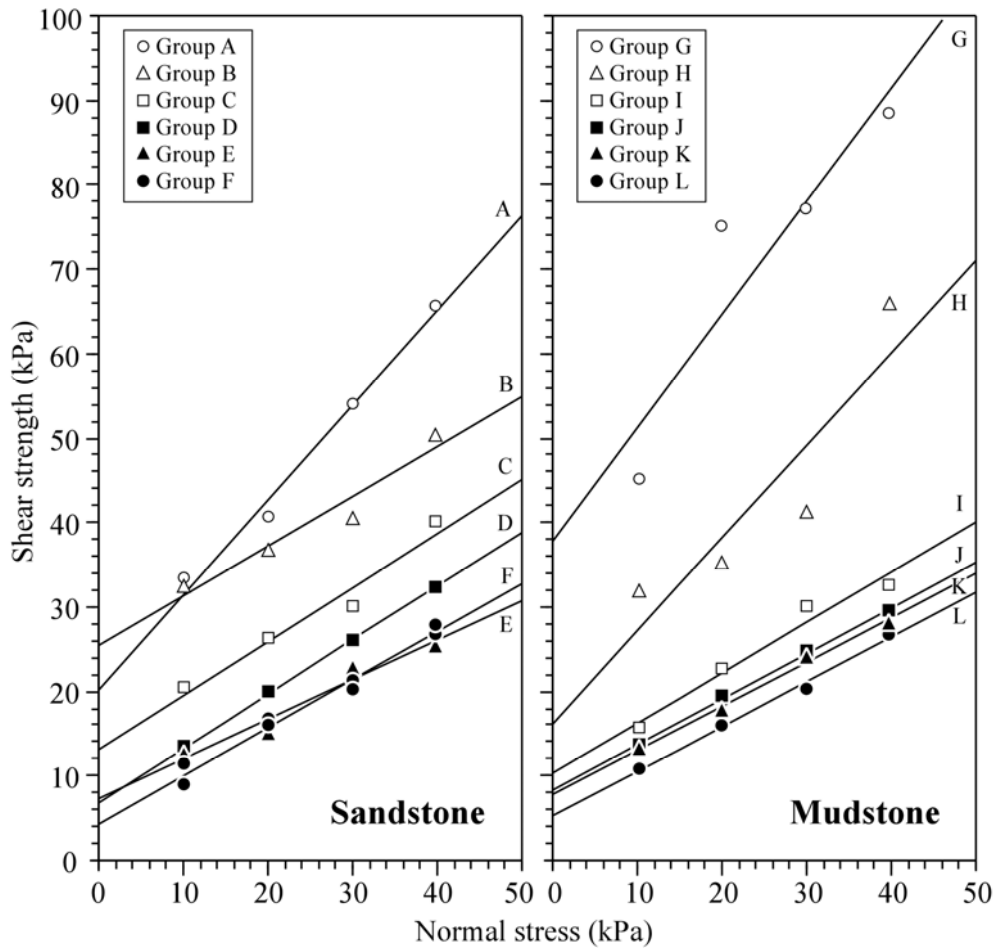


Figure 15 Results of shear tests for the soil specimens with varied moisture contents

Moisture condition of the soil changes from dried to saturated states (groups from A to F and groups from G to L). The solid lines represent simple linear-regressions for each specimen group in similar moisture conditions (cf. Table 5).

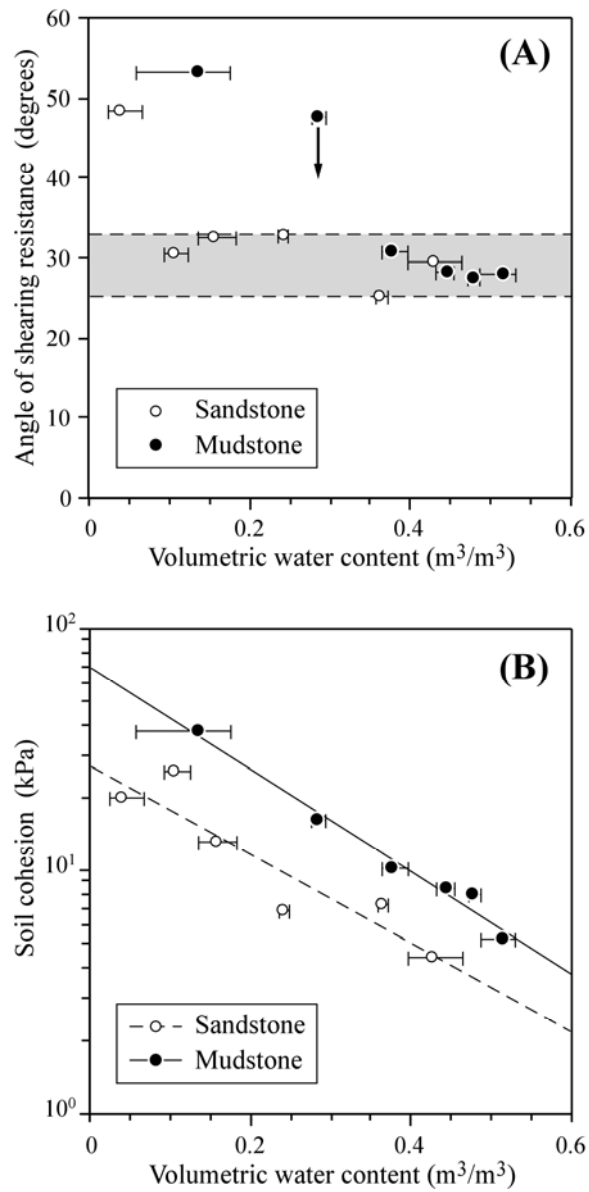


Figure 16 Relations between the volumetric water content and shear strength parameters

Error bars for the volumetric water contents indicate the ranges for each specimen group (cf. Table 5). The angle of shearing resistance (A) and soil cohesion (B) respectively represent the inclination and y-intercepts of the simple linear-regression for each moisture group (cf. Fig. 15 and Table 6).

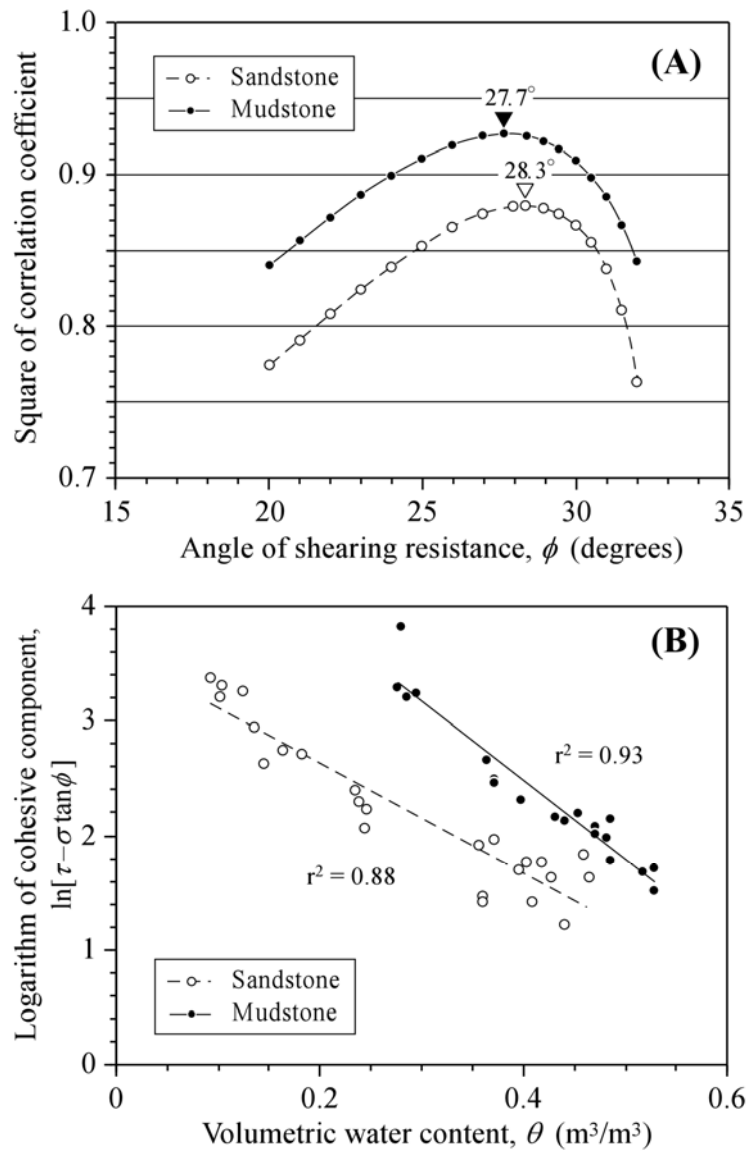


Figure 17 Results of multiple linear-regression analyses for the formulation of shear strength reduction

(A) Changes in square of correlation coefficient in which substituting varied angle of shearing resistance. (B) The best-fit correlations between logarithm of cohesive shear strength (left part of Eq. (3) in text) and volumetric water content. The relationships in (B) are obtained by substituting the most suitable angle of shearing resistance, i.e., the peak values in (A): 28.3° and 27.7° respectively.

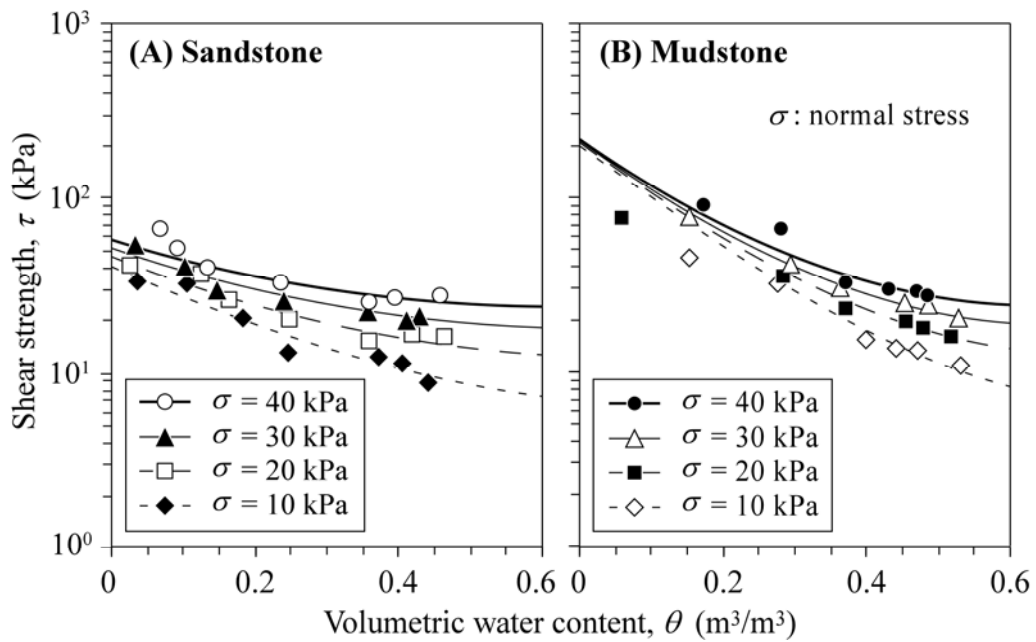


Figure 18 Reduction in shear strength with respect to increasing soil volumetric water content

The diagram targets only the test results for air-dried to capillary saturated conditions, Groups B to F, and H to L (cf. Table 5). The solid and broken lines represent best-fit regression curves for each soil (using Eq. (2) in text), whose optimum parameter values are listed in Table 7.

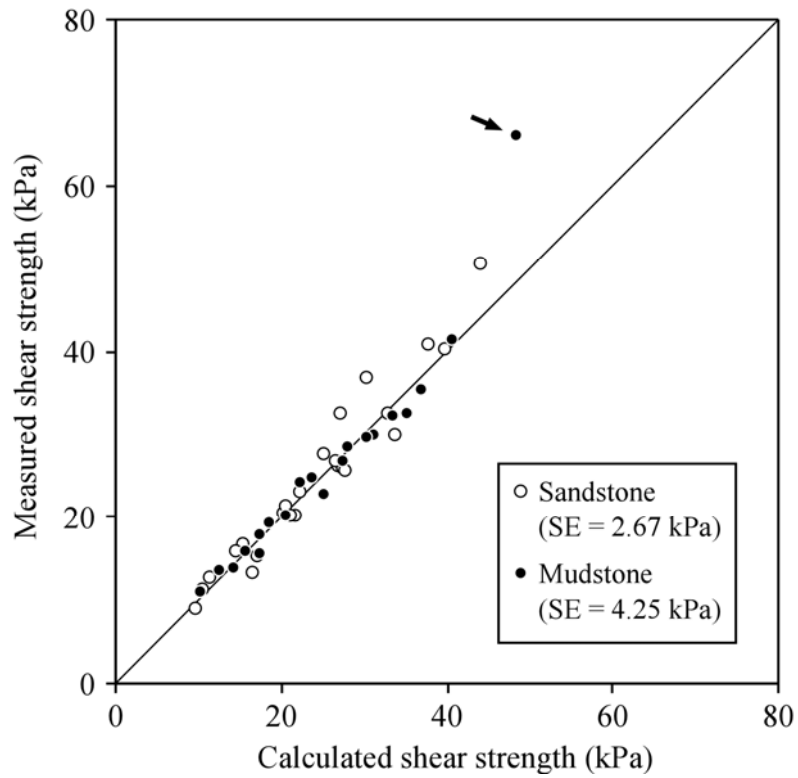


Figure 19 Comparison of measured and calculated shear strength

SE represents standard error of estimate: a standard deviation of the predictive residuals. The arrowed outlier is a datum with normal stress of 40 kPa within the group H (see Table 5)

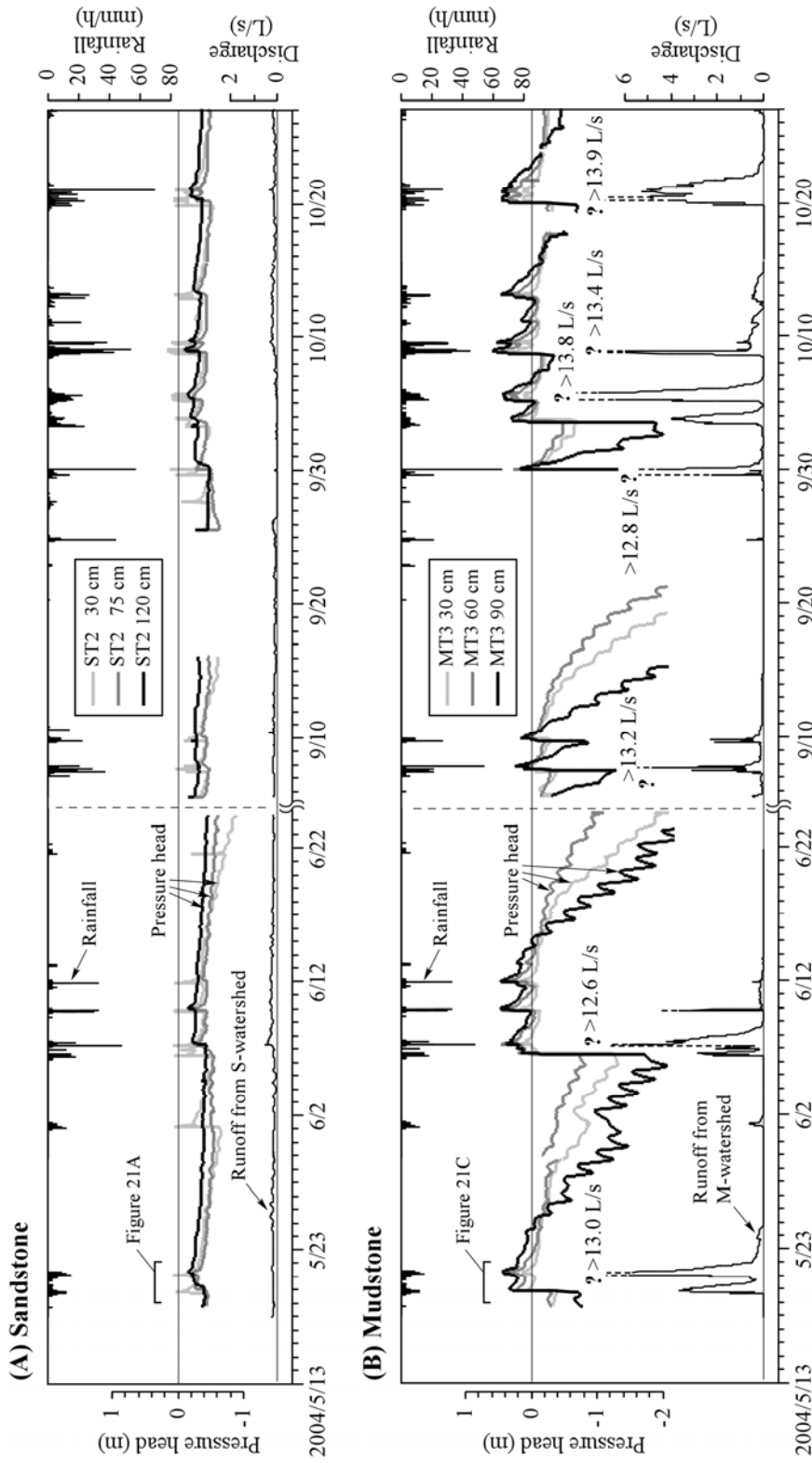


Figure 20 Pressure head fluctuations in slopes and hydrographs in watersheds for the entire observation period

The tensiometers at the nests ST2 and MT3 (cf. Fig. 9) provide the data as representatives of the pressure head responses. Soil desiccation during the summer months in 2004 exceeded the air-entry limit of ceramic cups, so that the pressure-head data lacked in this period.

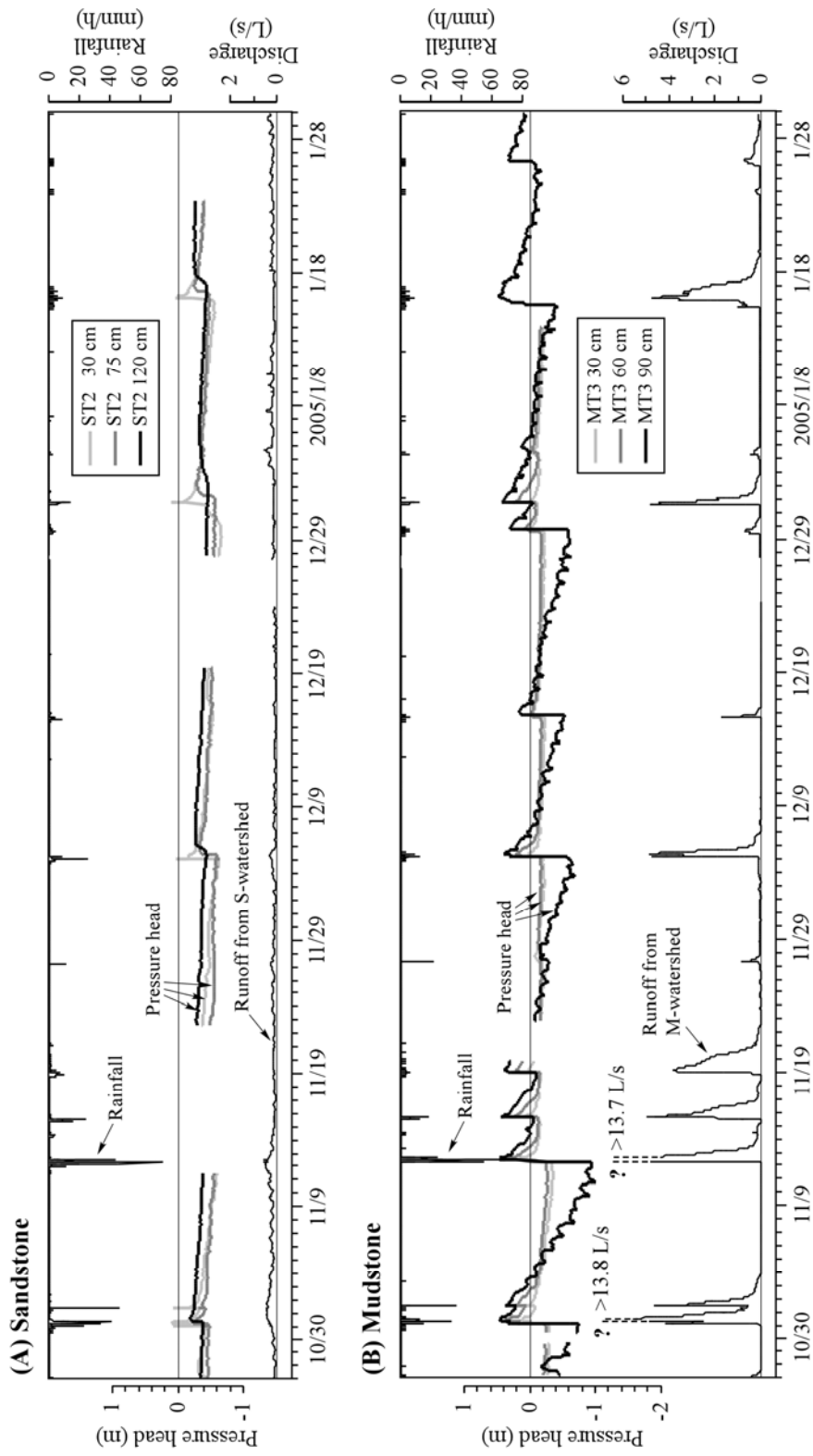


Figure 20 Continued

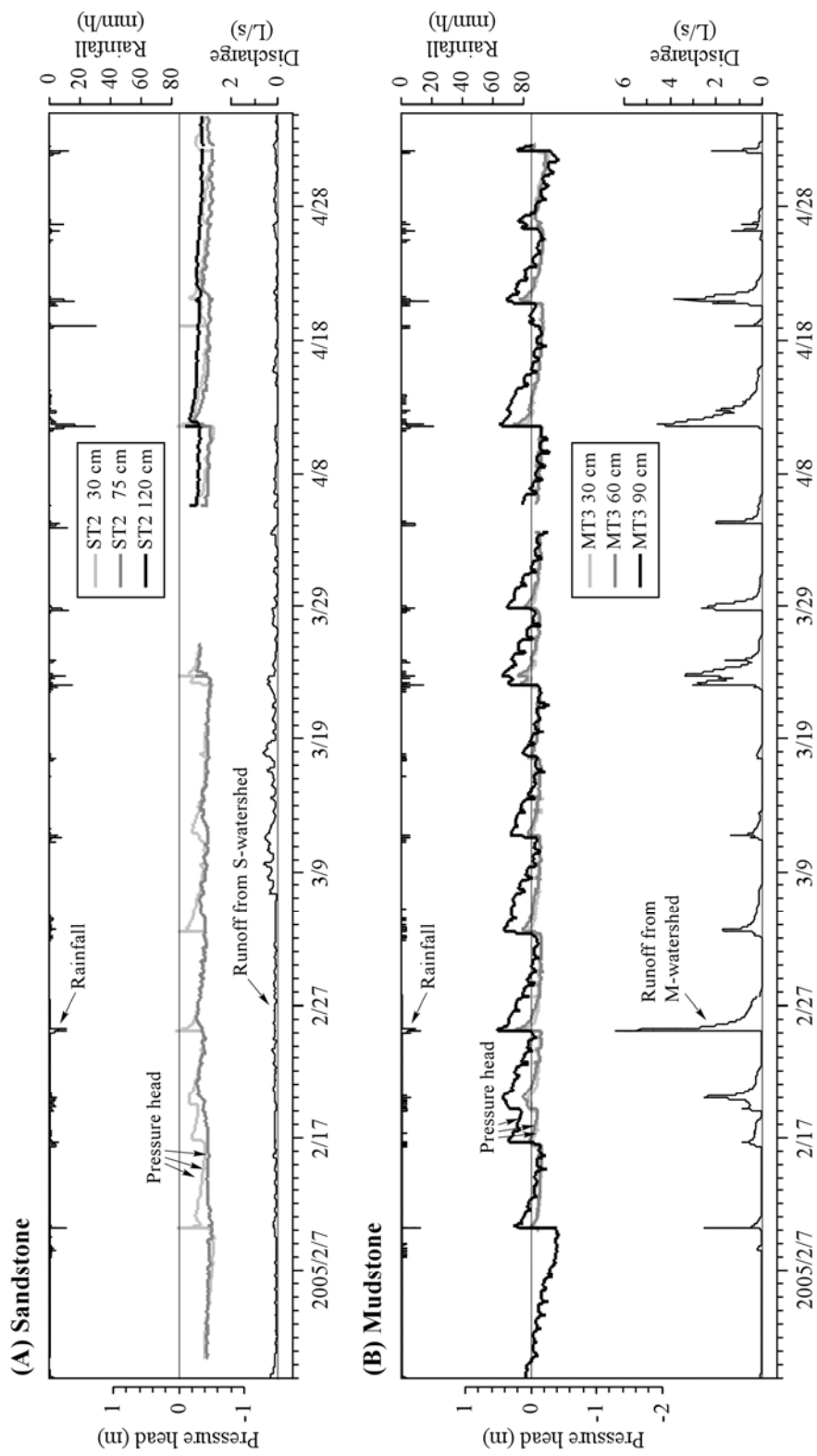


Figure 20 Continued

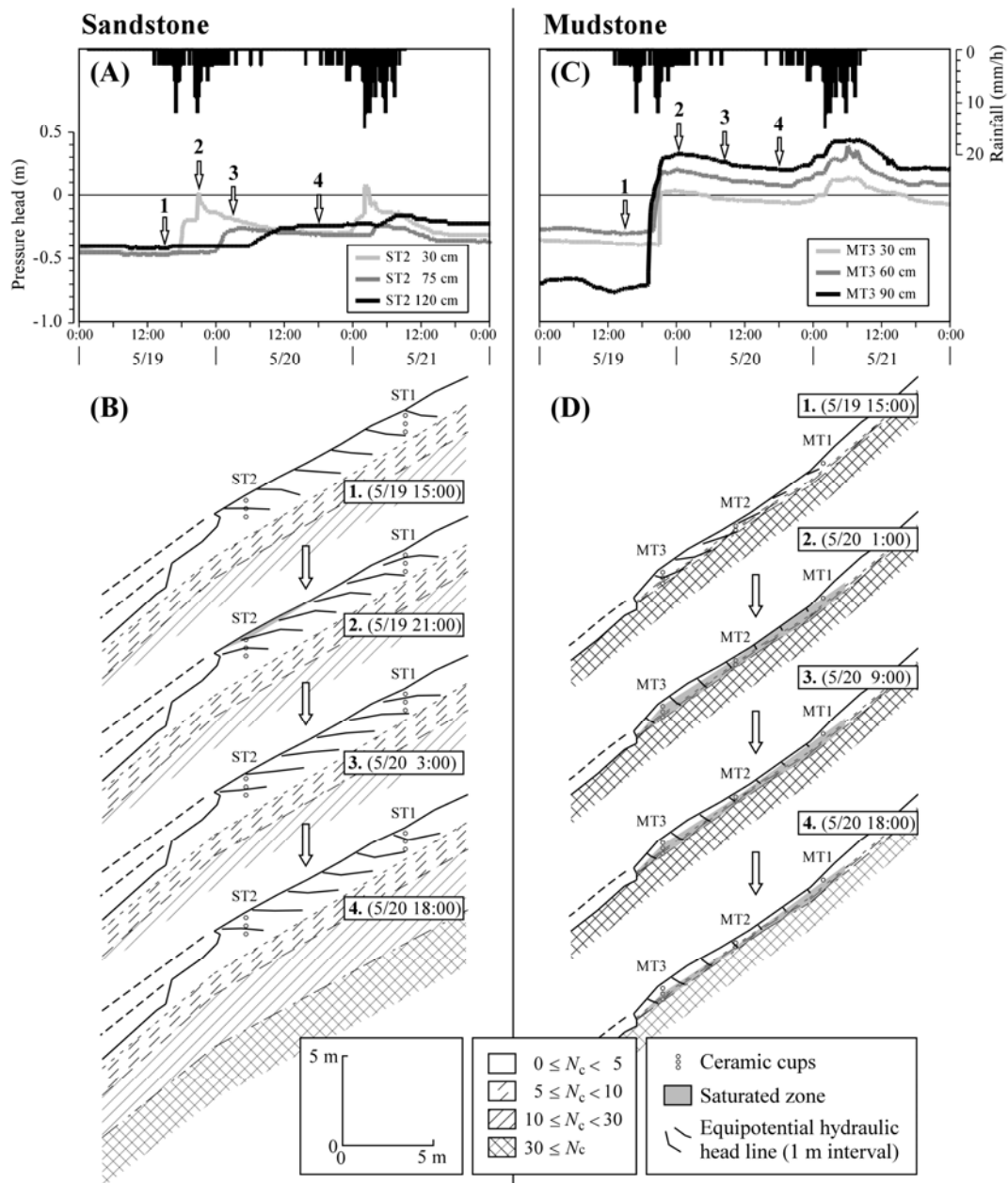


Figure 21 Short-term pressure head responses and equipotential lines of hydraulic head during May 19 to 21, 2004

Slope profiles illustrate the time-series alterations of hydraulic heads and distributions of saturated zone within the slopes. Interval of the equipotential lines is 1 m. The four timings correspond to the arrows in (A) and (C), respectively.

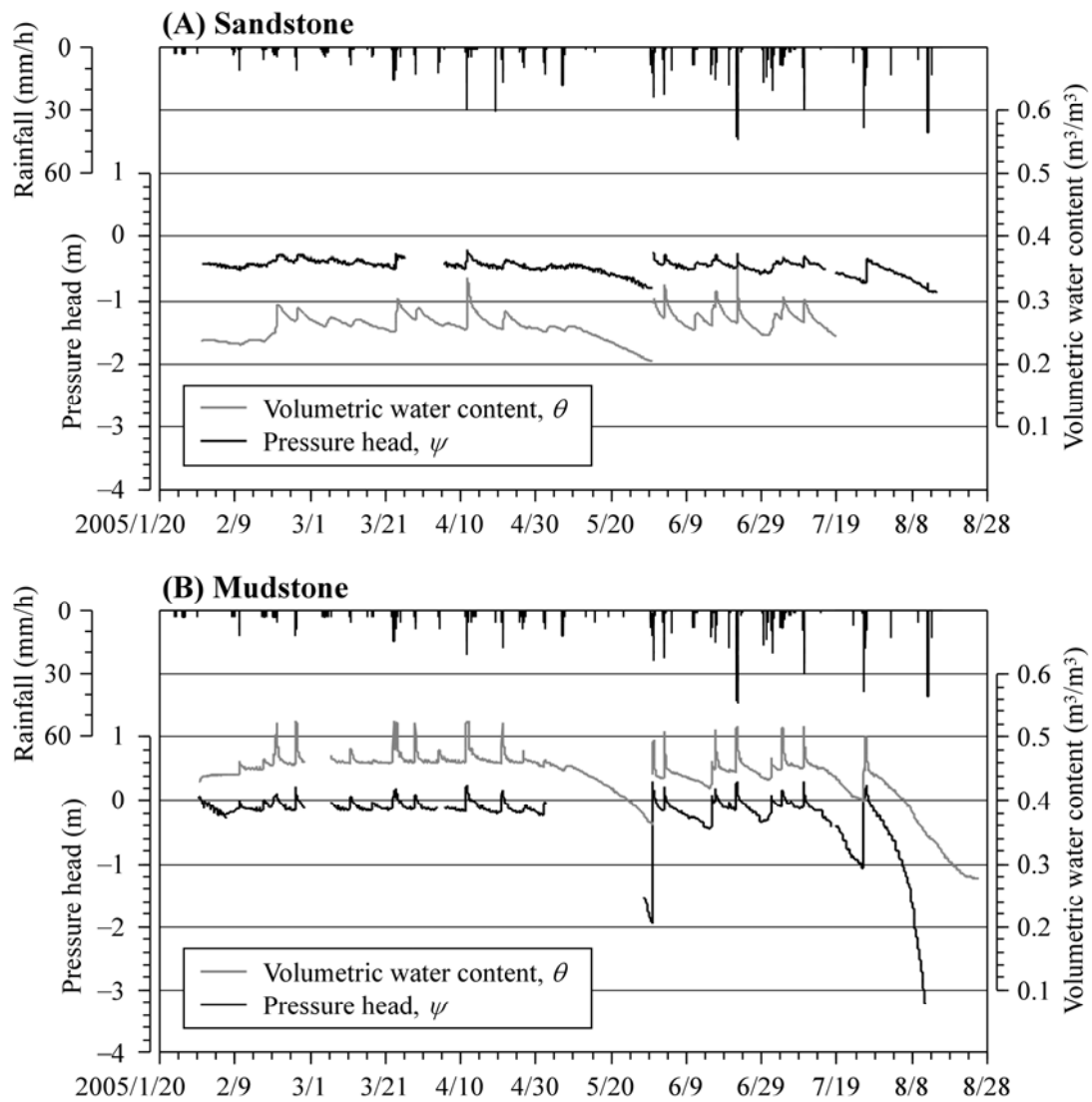


Figure 22 Changes in volumetric water content in slopes with fluctuations of pressure head at corresponding depths

Monitoring depth is 75 cm for sandstone and 60 cm for mudstone.

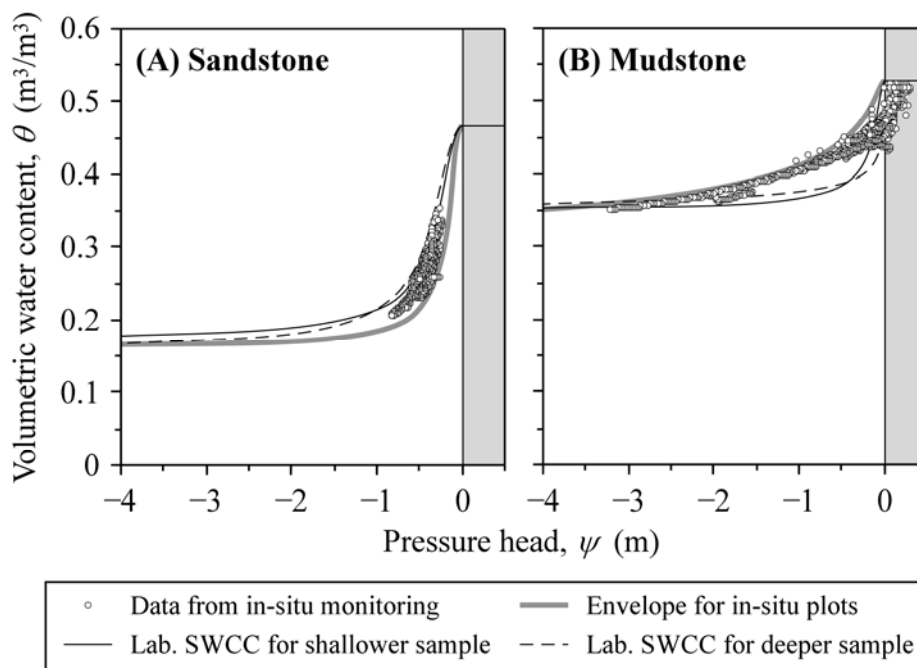


Figure 23 Soil-water retention plots from in situ monitoring

Open circles are results of simultaneous monitoring of pressure head and volumetric water content. SWCC: soil-water characteristic curve. Solid and broken lines indicate the best-fit model curves for laboratory data (cf. Table 4). Gray line is the lower (for sandstone) and upper (for mudstone) envelope for the in situ data. Parameters for the envelopes are listed in Table 8.

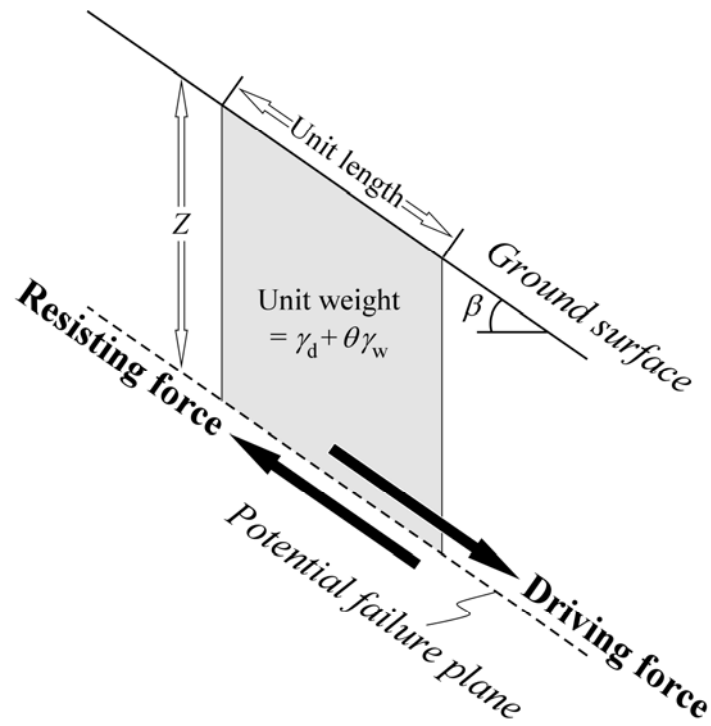


Figure 24 Schematic illustration of the infinite-slope model for the limit equilibrium stability analysis

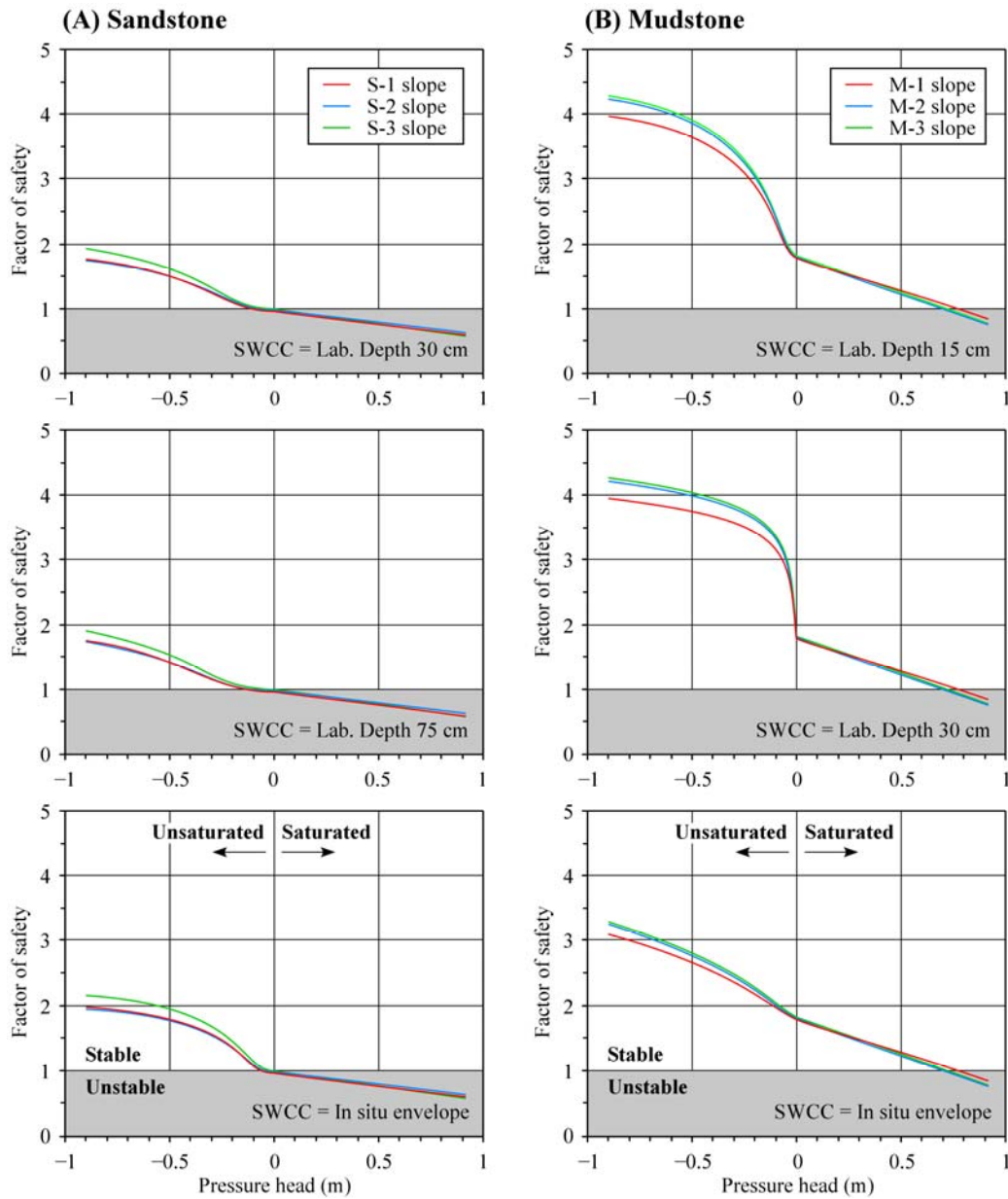


Figure 25 Simulation of the reduction in factor of safety with increasing pressure head

All curves originated from Eq. (6) by being substituted Eq. (1). SWCC: soil-water characteristic curve. Parameters for the SWCCs are listed in Tables 4 and 8 (see also Figs. 14 and 23). Soil weights and parameters for shear strength are shown in Tables 3 and 7 respectively. Actual slope angles and slip depths of the six surveyed slopes were used for computation (cf. Table 2).

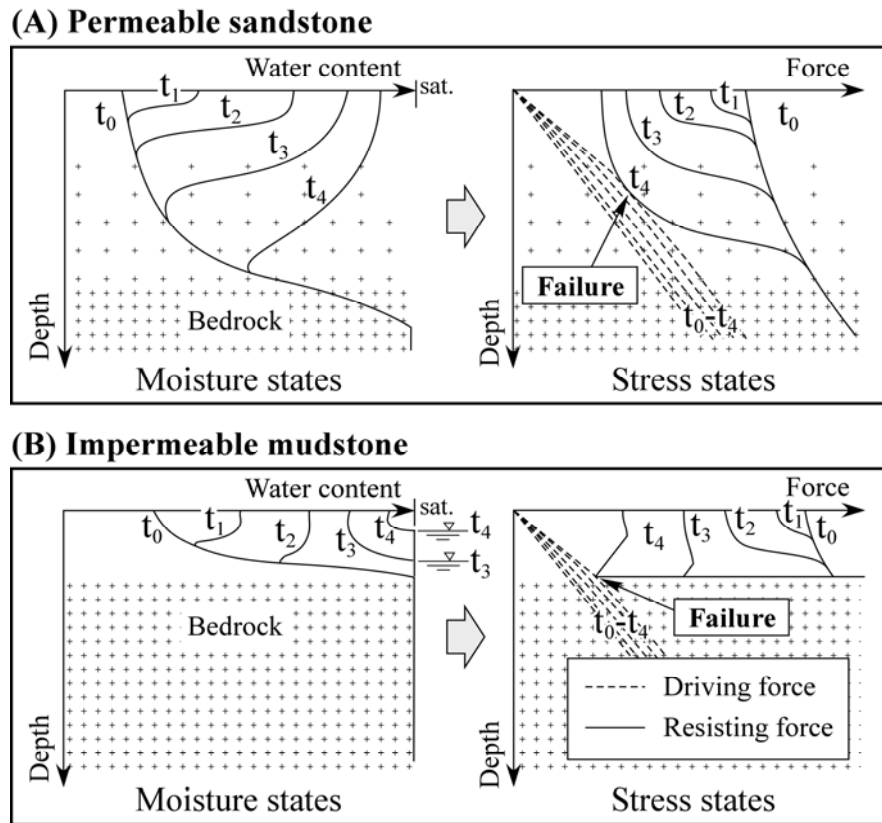


Figure 26 Schematic illustrations showing hydrological landslide-triggering mechanisms

The left part of the diagrams indicates wetting processes of slope materials. The right part represents the change in shear stress (broken lines) and shearing resistance (solid curves) within the slopes.

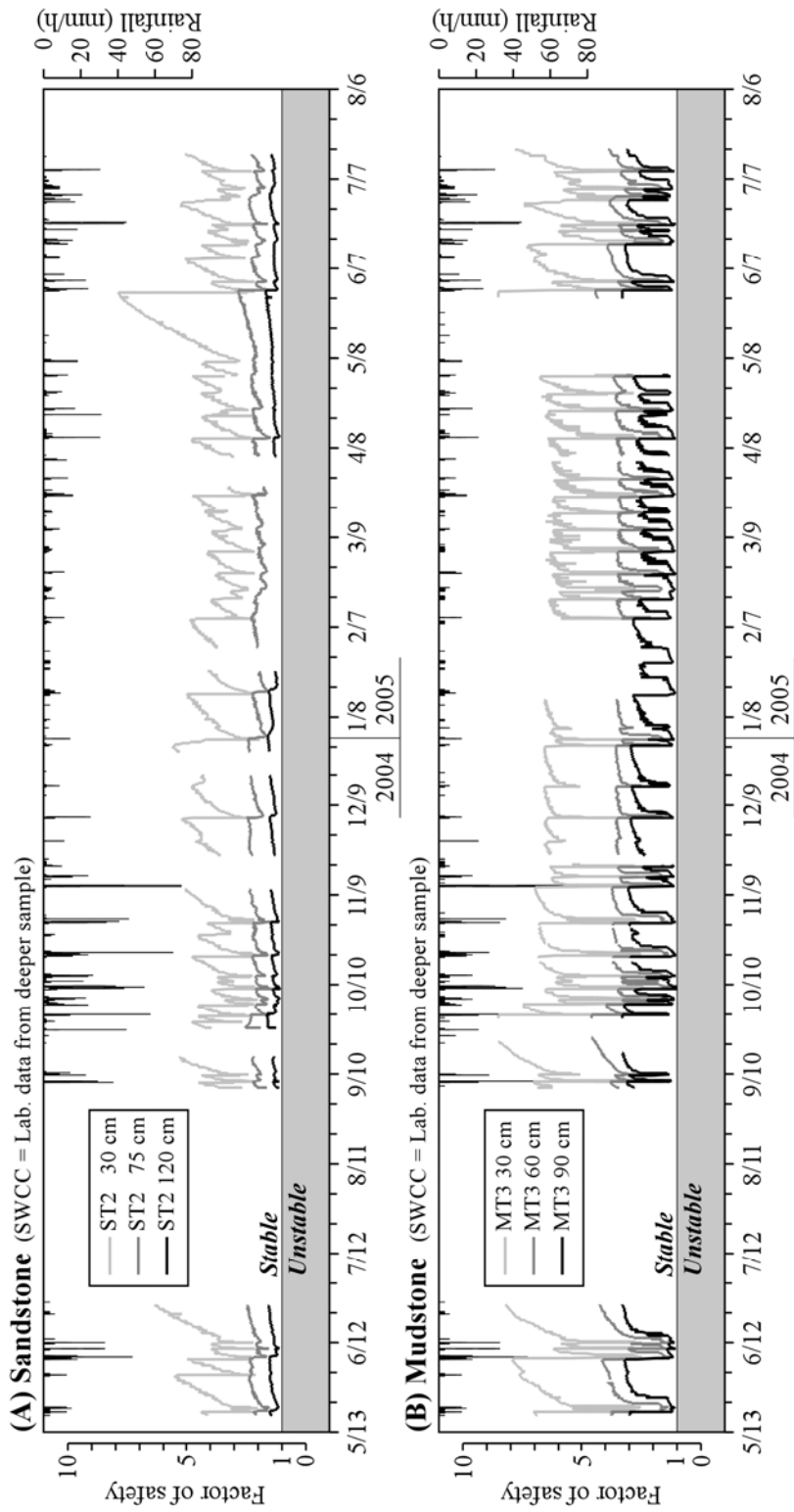


Figure 27 Slope stability fluctuations calculated from observed pressure heads

SWCC: soil-water characteristic curve. Both of the laboratory and in situ parameter-set for soil-water characteristic curves were used for calculation: (A) and (C) for the sandstone slope, (B) and (D) for the mudstone slope. Laboratory parameters are derived from samples at depth 75 cm for sandstone and 30 cm for mudstone (Table 4). In situ parameters are for envelopes in Fig. 22 (Table 8).

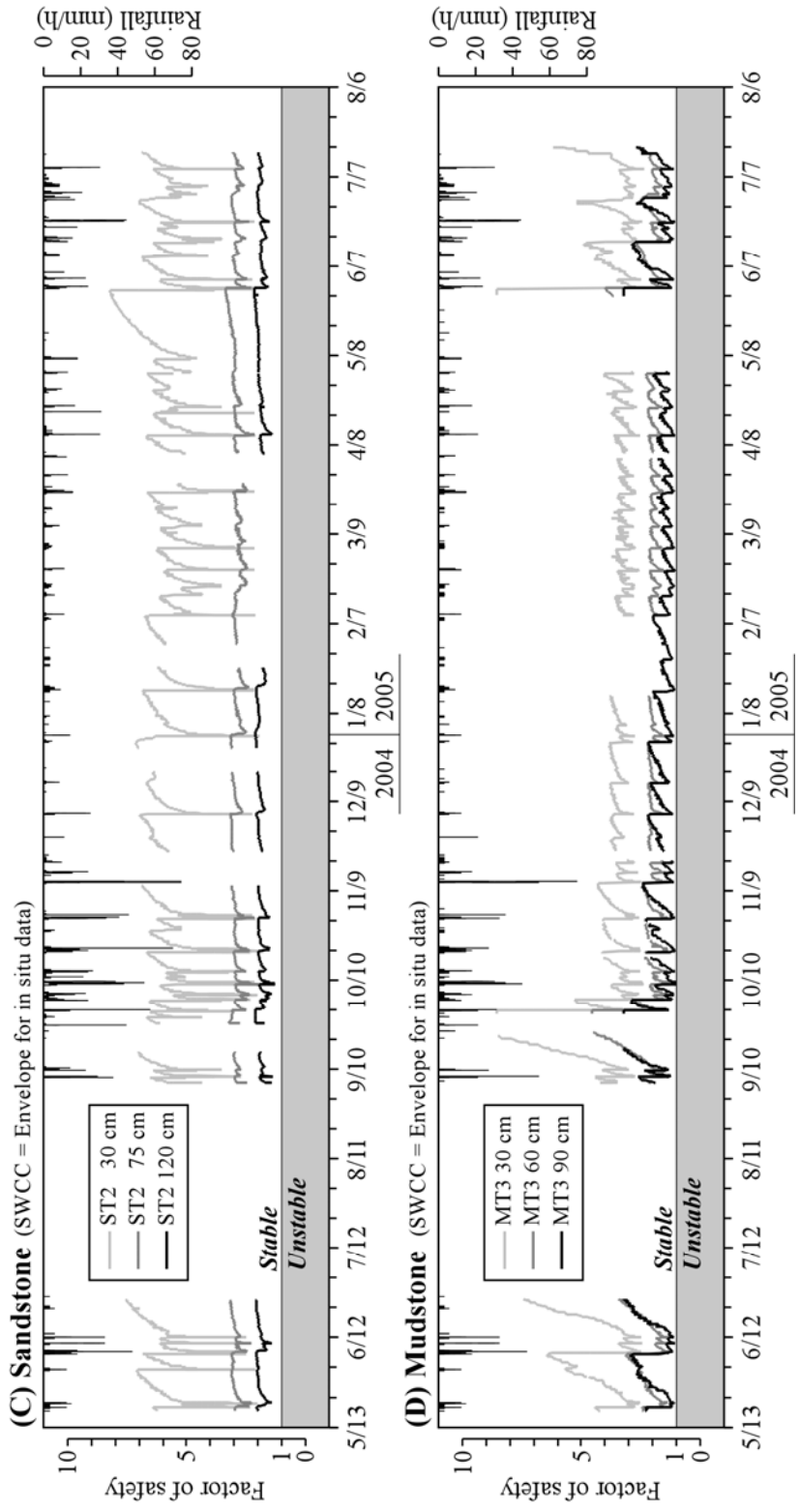


Figure 27 Continued

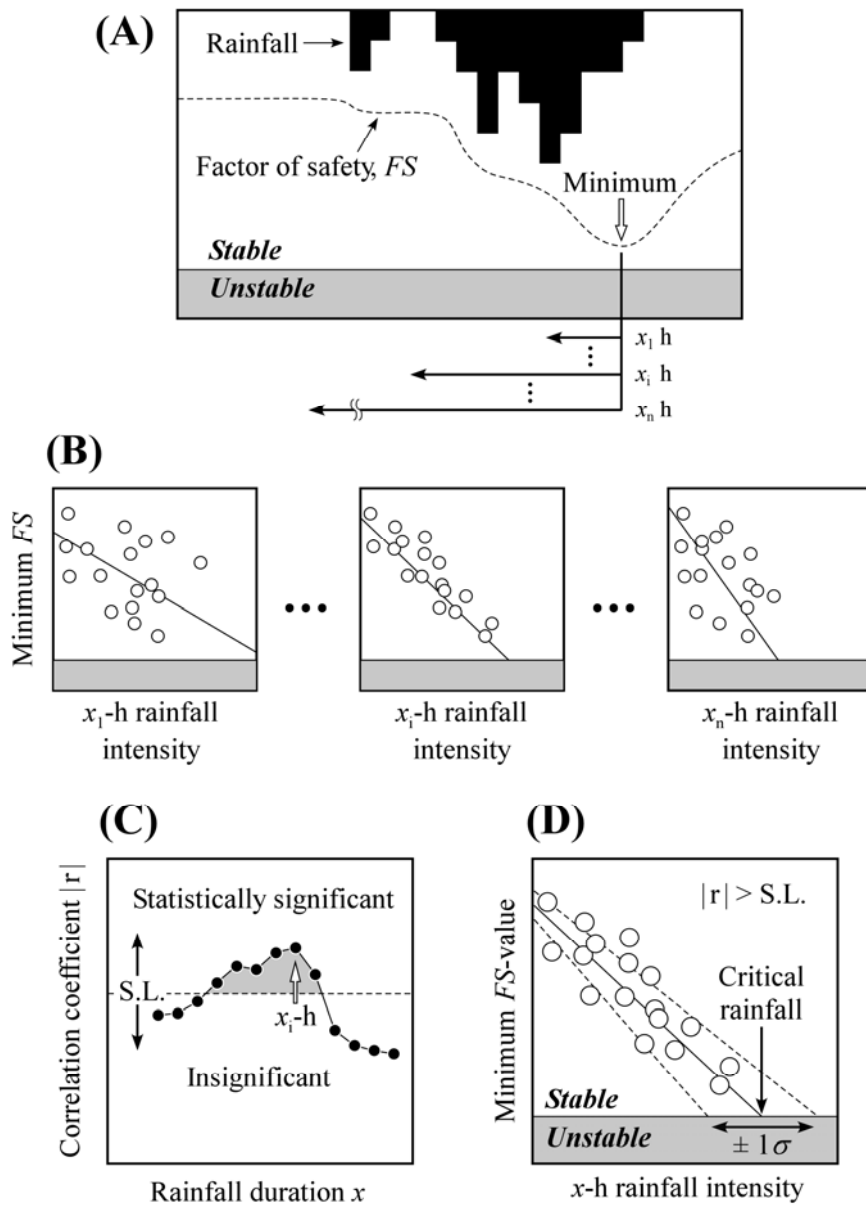


Figure 28 Analytical procedures for determining critical rainfall

(A) Schematic illustration of a diurnal factor of safety calculated from observed pressure heads, and time frames for the preceding rainfall durations. Shaded unstable regions are defined as a range of factor of safety below unity. (B) Sequential correlation analysis between minimum factor of safety and mean rainfall intensity during a given duration. (C) Identification of effective rainfall durations. S.L. is a significance level sorting out the statistically-meaningful correlation. (D) Definition of the critical rainfall intensities. Solid and broken lines indicate linear-regression lines with 68% confidence limits.

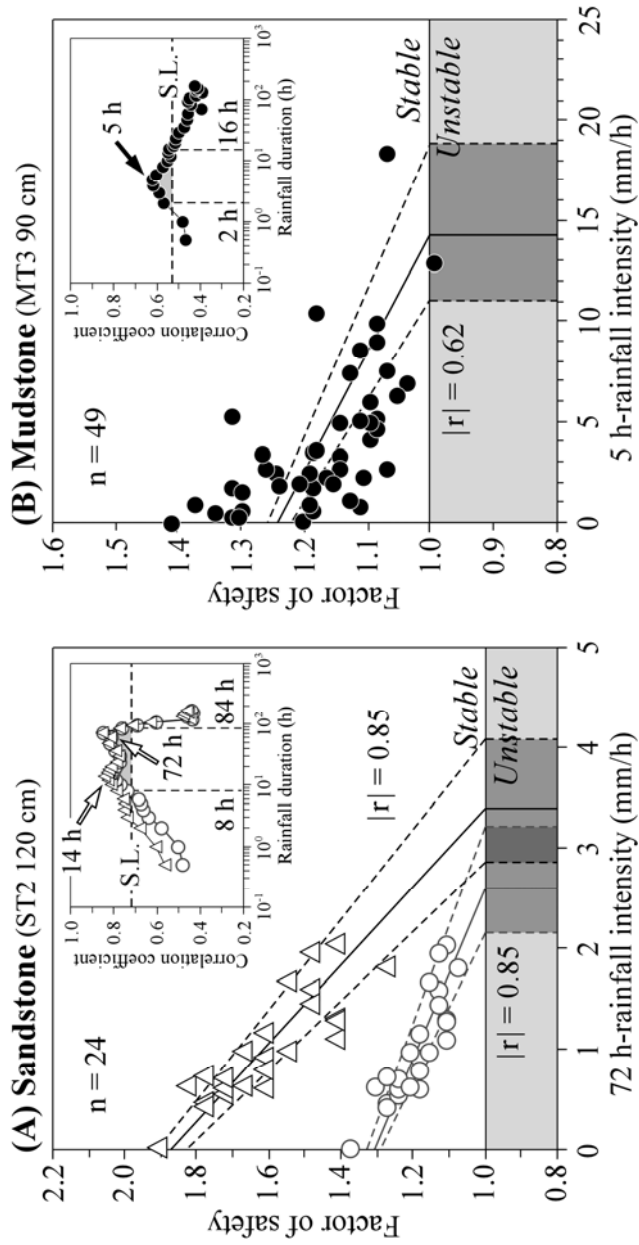


Figure 29 Inverse correlations between the minimum factors of safety and mean rainfall intensities at the most effective rainfall duration

Insets show the changes in the correlation coefficient against varying time frame of rainfall duration. Circles in the correlation for sandstone indicate the results from the laboratory soil-water characteristic curve (depth 75 cm, Fig. 14A); triangles show the results using the in situ envelope (Fig. 23A). Solid and broken lines indicate linear-regression lines with 68% confidence limits (cf. Fig. 28D).

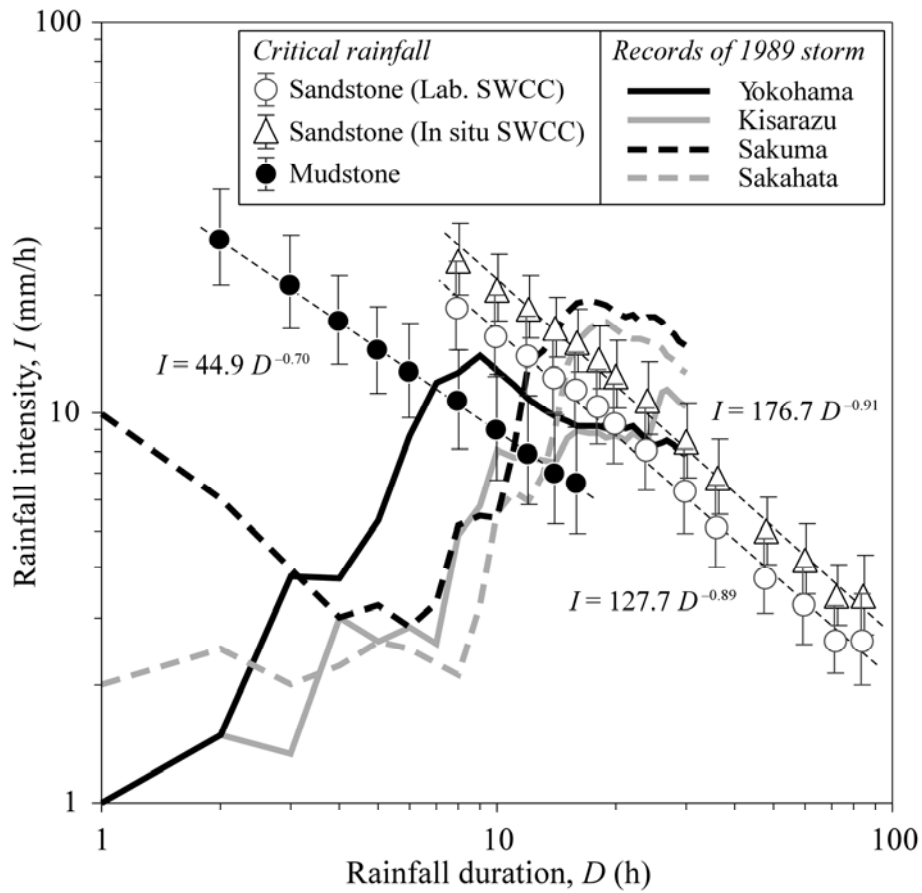


Figure 30 Rainfall thresholds for landsliding and temporal changes in mean rainfall intensity of the torrential rainfall on August 1, 1989

SWCC: soil-water characteristic curve. Open circles in the critical rainfall for the sandstone were calculated by using the SWCC for the samples from 75 cm depth (Fig. 14A, Table 4). Triangles represent the results by using the envelope for the in situ SWCC (Fig. 23A). Error bars of the critical rainfall represent 68% confidence limits from the linear-regression analysis (cf. Fig. 28D). The four bold lines were computed from the rainfall records of the 1989 storm (Fig. 5), by dividing the cumulative rainfall with elapsed time from the onset of the storm body.

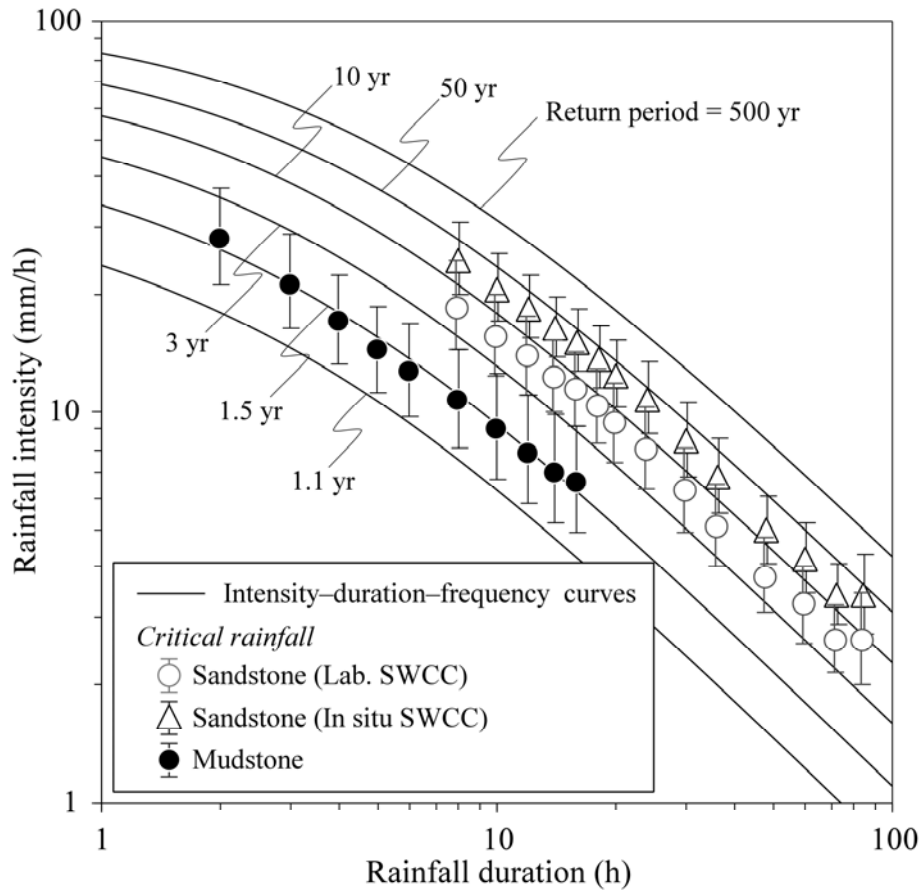


Figure 31 Recurrence intervals of the critical rainfall

SWCC: soil-water characteristic curve. Open circles in the critical rainfall for the sandstone were calculated by using the SWCC for the samples from 75 cm depth (Fig. 14A, Table 4). Triangles represent the results by using the envelope for the in situ SWCC (Fig. 23A). The intensity–duration–frequency curves were computed from the annual records of the most intensive 1-h and 1-day rainfall from 1940 to 2004 at Yokohama meteorological station.

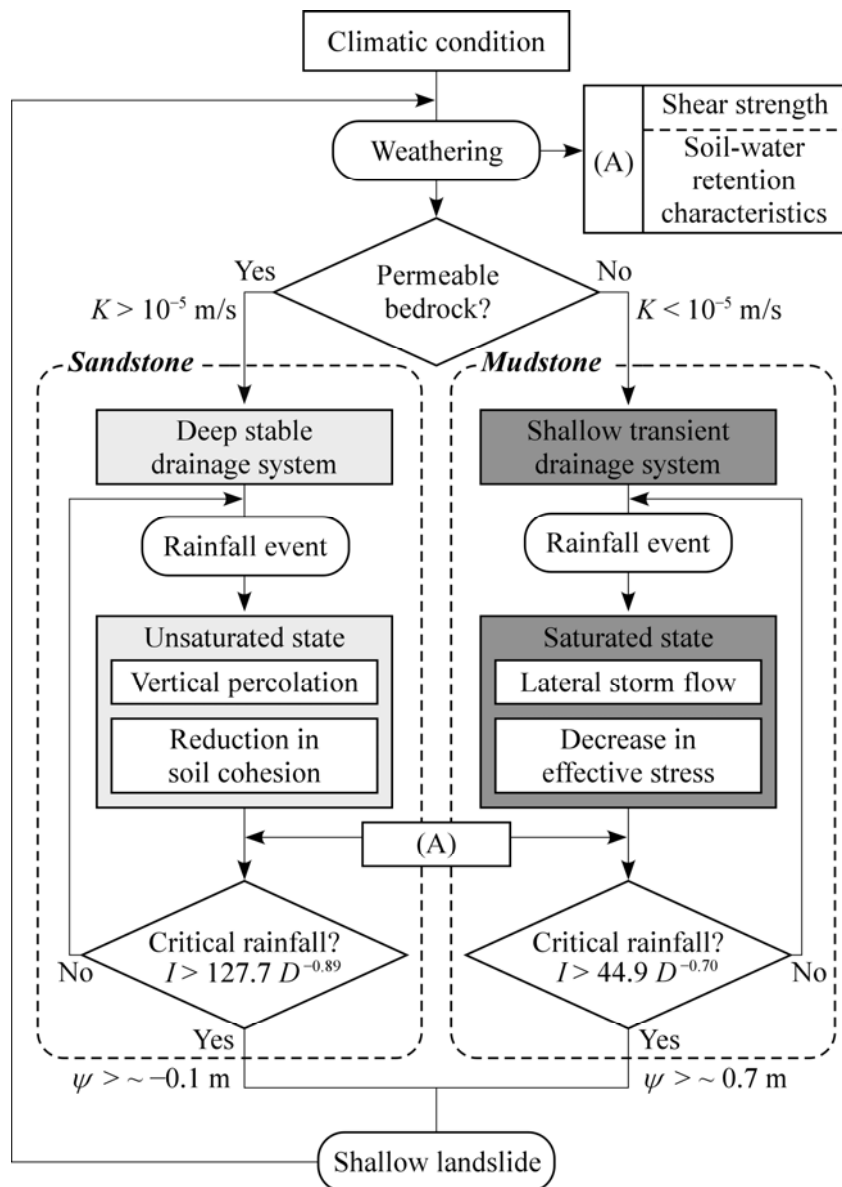


Figure 32 Hydrological landslide-triggering cycles in hillslopes with permeable and impermeable bedrocks

K : permeability; I : rainfall intensity; D : rainfall duration; ψ : pressure head. Permeability of bedrock dictates the two flows of hydrological processes and instability mechanisms leading to the landslide initiation in hillslopes. Shear strength and soil-water retention characteristics also affect the rainfall threshold for landsliding as denoted by Box A.